

CONSTRAINING THE INITIAL CONDITIONS AND FINAL
OUTCOMES OF ACCRETION PROCESSES AROUND YOUNG
STARS AND SUPERMASSIVE BLACK HOLES

by

Jordan M. Stone



A Dissertation Submitted to the Faculty of the

DEPARTMENT OF ASTRONOMY

In Partial Fulfillment of the Requirements
For the Degree of

DOCTOR OF PHILOSOPHY

In the Graduate College

THE UNIVERSITY OF ARIZONA

2015

THE UNIVERSITY OF ARIZONA
GRADUATE COLLEGE

As members of the Dissertation Committee, we certify that we have read the dissertation prepared by Jordan M. Stone entitled Constraining the Initial Conditions and Final Outcomes of Accretion Processes around Young Stars and Supermassive Black Holes and recommend that it be accepted as fulfilling the dissertation requirement for the Degree of Doctor of Philosophy.

Date: 14 September 2015

Josh Eisner

Date: 14 September 2015

Dan Marone

Date: 14 September 2015

Kaitlin Kratter

Date: 14 September 2015

Laird Close

Date: 14 September 2015

George Rieke

Final approval and acceptance of this dissertation is contingent upon the candidate's submission of the final copies of the dissertation to the Graduate College.

I hereby certify that I have read this dissertation prepared under my direction and recommend that it be accepted as fulfilling the dissertation requirement.

Date: 14 September 2015

Dissertation Director: Josh Eisner

STATEMENT BY AUTHOR

This dissertation has been submitted in partial fulfillment of requirements for an advanced degree at the University of Arizona and is deposited in the University Library to be made available to borrowers under rules of the Library.

Brief quotations from this dissertation are allowable without special permission, provided that an accurate acknowledgment of the source is made. This work is licensed under the Creative Commons Attribution-No Derivative Works 3.0 United States License. To view a copy of this license, visit <http://creativecommons.org/licenses/by-nd/3.0/us/> or send a letter to Creative Commons, 171 Second Street, Suite 300, San Francisco, California, 94105, USA.

SIGNED: Jordan M. Stone

ACKNOWLEDGEMENTS

I would first like to thank my family. My wife, Megan, has been incredibly supportive, especially in these last few months as I sprinted to finish this document. My parents whose steadfast support has provided the firm foundation I needed to reach for the stars. My grandparents, Alberta and Wesley, first showed me the Teapot in Sagittarius, and Grammy, told the nurse that “her boy” was an astronomer after the European Philae probe landed on Comet 67P/ChuryumovGerasimenko. No one could hope for a better team of cheerleaders than all of you.

I thank my advisor, Josh Eisner, who has been a great mentor and great climbing partner. I also had the opportunity to work closely with Dan Marrone and Kaitlin Kratter, who both helped me grow as a scientist and have been great advocates.

My peers, including Evan Schneider, Tim Arnold, Michi Bauböck, Vanessa Bailey, Steph Sallum, David Lesser, and others made Steward a very fun place to be a graduate student.

DEDICATION

To Megan, an unimaginably good teammate.

TABLE OF CONTENTS

LIST OF FIGURES	9
LIST OF TABLES	11
ABSTRACT	12
CHAPTER 1 Introduction	15
1.1 Star and Planet Formation	16
1.1.1 Protoplanetary Disks	16
1.1.2 The Formation of Gas-Giant Planets	21
1.2 The Super-Massive Black Hole at the Center of the Galaxy	25
1.2.1 Probing the Gravitational Potential of a Super-Massive Black Hole with Improved Astrometry of Stellar Orbits	25
1.2.2 Accretion onto the Super-Massive Black Hole at the Center of our Galaxy	27
CHAPTER 2 Variable Accretion Processes in the Young Binary-Star System	
UY Aur [†]	30
2.1 Introduction	31
2.2 Observations and Reduction	33
2.3 Results and Analysis	38
2.3.1 Equivalent Widths	38
2.3.2 Line Luminosities	39
2.3.3 Accretion Rates	39
2.3.4 H ₂ Lines	40
2.3.5 Veiling	43
2.4 Discussion	44
2.5 Conclusions	48
CHAPTER 3 L-band Spectroscopy with Magellan-AO/Clio2: First Results on	
Young Low-Mass Companions [†]	56
3.1 Introduction	57
3.2 Observations and Reduction	59
3.2.1 Target Selection and Parameters from Literature	59
3.2.2 Instrumental Setup	60
3.2.3 Data Acquisition	62

TABLE OF CONTENTS – *Continued*

3.2.4	Preliminary Reduction	64
3.2.5	Spectral Extraction	65
3.2.6	Wavelength Calibration	65
3.2.7	Telluric Calibration	67
3.3	Results	67
3.3.1	Model Atmosphere Fits	67
3.3.2	Comparison to Field Dwarf Spectra	71
3.4	Discussion	73
3.4.1	Comparison to Directly Imaged Planets	73
3.4.2	The Red Slope of CD-35 2722 B	74
3.4.3	A Blue Feature in AB Pic b and 2M 0103(AB) b	75
3.5	Conclusions	76
CHAPTER 4 Disentangling Confused Stars at the Galactic Center with Long		
	Baseline Infrared Interferometry [†]	78
4.1	Introduction	79
4.2	Simulating a Star Field within 50 Milliarcseconds of Sgr A*	83
4.3	Synthesizing Visibility Data	85
4.3.1	Basic Concepts	85
4.3.2	Sources of Uncertainty for Phase Referenced Interferometric Imaging	87
4.3.3	Producing Mock Fringes	90
4.3.4	Observing Routine, UV-coverage, and PSFs	93
4.4	Fitting Stellar Positions to Visibility Data	95
4.5	Results	97
4.5.1	Star Fields Observed with ASTRA at the Keck Interferometer	97
4.5.2	Star Fields Observed with GRAVITY	107
4.6	Discussion	115
4.7	Summary and Future Work	119
CHAPTER 5 Far Infrared Variability of Sagittarius A*: 25.5 hours of Monitor-		
	ing with <i>Herschel</i> [†]	121
5.1	Introduction	122
5.2	Observations and Reduction	125
5.2.1	<i>Herschel</i> SPIRE	125
5.2.2	Caltech Submillimeter Observatory 0.85 mm	129
5.2.3	<i>XMM-Newton</i>	130
5.2.4	SMA 1.3 mm	131
5.3	Results	131
5.4	Discussion	136

TABLE OF CONTENTS – *Continued*

5.5	Conclusions	140
CHAPTER 6	Conclusions	143
6.1	Variable accretion processes in the young binary-star system UY Aur	143
6.2	L-band Spectroscopy with Magellan-AO/Clio2: First Results on Young Low-Mass Companions	143
6.3	Disentangling Confused Stars at the Galactic Center with Long Base- line Infrared Interferometry	145
6.4	Far Infrared Variability of Sagittarius A*: 25.5 hours of Monitoring with <i>Herschel</i>	146
REFERENCES	147

LIST OF FIGURES

2.1	Dewarping	35
2.2	Rectified Lamp Lines	35
2.3	Defringing the Flat	38
2.4	Defringing Telluric Calibrators	49
2.5	Defringing Near Broad Lines	49
2.6	Measuring Equivalent Widths of Broad Lines	50
2.7	Mass Accretion Rate vs. Time	51
2.8	Relative Accretion Rate vs. Time	52
2.9	Molecular Hydrogen Lines	53
2.10	Molecular Gas Temperature	54
2.11	Veiling	55
3.1	Best fit spectral resolution	66
3.2	L-band spectra of low-mass companions compared to model atmospheres	68
3.3	Surface gravity as a function of mass and age	69
3.4	L-band spectra of low-mass companions compared to field dwarfs . .	72
4.1	Keck-Interferometer uv-Coverage and beam	94
4.2	VLTI uv-Coverage and Beam	94
4.3	Model Fitting to Simulated Data	96
4.4	Simulated Keck-Interferometer Visibilities	97
4.5	Single Epoch Fit to Keck-Interferometer Simulations	98
4.6	Multi-epoch Performance with Keck Inteferometer	99
4.7	Fit Performance Depends on Positional Angle with Keck	100
4.8	Single-epoch Keck Interferometer performance on Field2	101
4.9	Multi-epoch Keck Interferometer Performance on Field2	102
4.10	Fit Performance Depends on Positional Angle with Keck Field2 . . .	102
4.11	Keck Interferometer Beam and Example Orbit	106
4.12	Isolating the Effects of Crowding, Keck Interferometer	108
4.13	Multi-epoch Performance with the VLTI	109
4.14	Multi-epoch Performance with the VLTI, Error Ellipses	110
4.15	Multi-epoch Performance with the VLTI, Field2	112
4.16	VLTI Beam and Example Orbit	113
4.17	Isolating the Effects of Crowding, VLTI	114
4.18	Multi-epoch Performance with the VLTI, Field0	115
5.1	Submillimeter Maps	127

LIST OF FIGURES – *Continued*

5.2	Light curves from first observing interval	133
5.3	Light curves from second observing interval	134
5.4	Cross correlations	135
5.5	Variability amplitude cumulative distribution	137
5.6	Submillimeter color changes in variable features	139
5.7	Variability Power spectrum	141

LIST OF TABLES

2.1	Observations	37
2.2	Equivalent Widths and Line Luminosities	41
3.1	Observing log	60
3.2	Summary of target information from the literature	61
3.3	BT-Settl Model Atmosphere Fits to L-band Spectra	71
4.1	Model star field parameters for our simulated fields.	84
4.2	Coherence Length	87
4.3	Parameters	92
4.4	Keck simulated data signal to noise for each spectral channel for Field1104	
4.5	Keck simulated data signal to noise for each spectral channel for Field2105	
4.6	VLTI simulated signal-to-noise ratios for each spectral channel for Field1111	
4.7	VLTI simulated signal-to-noise ratios for each spectral channel for Field2111	
5.1	<i>Herschel</i> SPIRE ObsIDs	126

ABSTRACT

In this thesis I discuss probes of small spatial scales around young stars and protostars and around the supermassive black hole at the galactic center. I begin by describing adaptive optics-fed infrared spectroscopic studies of nascent and newborn binary systems. Binary star formation is a significant mode of star formation that could be responsible for the production of a majority of the galactic stellar population. Better characterization of the binary formation mechanism is important for better understanding many facets of astronomy, from proper estimates of the content of unresolved populations, to stellar evolution and feedback, to planet formation. My work revealed episodic accretion onto the more massive component of the pre-main sequence binary system UY Aur. I also showed changes in the accretion onto the less massive component, revealing contradictory indications of the change in accretion rate when considering disk-based and shock-based tracers. I suggested two scenarios to explain the inconsistency. First, increased accretion should alter the disk structure, puffing it up. This change could obscure the accretion shock onto the central star if the disk is highly inclined. Second, if accretion through the disk is impeded before it makes it all the way onto the central star, then increased disk tracers of accretion would not be accompanied by increased shock tracers. In this case mass must be piling up at some radius in the disk, possibly supplying the material for planet formation or a future burst of accretion. My next project focused on characterizing the atmospheres of very low-mass companions to nearby young stars. Whether these objects form in an extension of the binary-star formation mechanism to very low masses or they form via a different process is an open question. Different accretion histories should result in different atmospheric composition, which can be constrained with spectroscopy. I showed that 3–4 μm spectra of a sample of these objects with effective temperatures greater than 1500 K are similar to the spectra of older more

massive brown dwarfs at the same temperature, in contrast to objects at 1000 K that exhibit distinct L-band SEDs. The oldest object in my sample of young companions, 50 My old CD-35 2722 B, appears redder than field dwarfs with similar spectral type based on 1–2.5 μm spectra. This could indicate reduced cloud opacity compared to field dwarfs at the same temperature.

I also present work to better understand the supermassive blackhole at the center of our Galaxy. Astrometric monitoring of stellar orbits about the black hole have been used to sketch the gravitational potential, revealing $4 \times 10^6 M_{\odot}$ within a radius of 40 AU. Further constraints on the gravitational potential, and the detection of post-Newtonian effects on the stellar orbits, will require improved astrometric precision. Currently confusion noise in the crowded central cluster limits astrometric precision. Increased spatial resolution can alleviate confusion noise. Dual field phase referencing on large-aperture infrared interferometers provides the sensitivity needed to observe the Galactic center, providing the fastest route to increased spatial resolution. I present simulations of dual-field phase referencing performance with the Keck Interferometer and with the VLTI GRAVITY instrument, to describe the potential contributions each could make to Galactic center stellar astrometry. I demonstrate that the near-future GRAVITY instrument at the VLTI will have a large impact on the ability to precisely track the paths of stars orbiting there, as long as a star with K-band apparent magnitude less than 20 exists within 70 milliarcseconds of the blackhole. Many of the stars orbiting the blackhole are in a post-main sequence wind phase. The wind from these stars is feeding an accretion flow falling onto the blackhole. This flow is radiatively inefficient, producing only 10^{-8} times the Eddington limit. Thus our relative proximity to the center of our own Galaxy, provides the opportunity to study a low-luminosity accretion mode that would be difficult or impossible to observe in more remote galaxies. Variable emission from the accretion flow arises from very deep within the flow and could be used to reveal the physics of the accretion process. Characterizing the variability is challenging because all wavelength regimes from radio through X-ray are affected by the process(es) that gives rise to the variations. I report observations of variability at wavelengths that

are difficult or challenging to observe from the ground using the SPIRE instrument onboard the *Herschel Space Observatory*. My work provides the first constraints on the flux of the accretion flow at 250 μm . Variations at 500, 350, and 250 μm observed with *Herschel* exhibit typical amplitudes similar to the variations observed at 1300 μm from the ground, but the amplitude distribution of flux variations observed with *Herschel* does not exhibit a tail to large amplitudes that is seen at 1300 μm . This could suggest a connection between large-amplitude mm/submillimeter variations and X-ray activity, since no increased X-ray activity was observed during our *Herschel* monitoring.

CHAPTER 1

Introduction

This thesis includes two parts, both of which explore the fundamental role that accretion processes play in astrophysics. The main focus will be on star and planet formation using high-spatial resolution techniques to obtain spectra of closely separated systems. As discussed below, these spectra are valuable for characterizing protoplanetary disks, which process the material from which stars and planets form. Additionally, spectroscopy of young directly imaged companions orbiting nearby stars constrains their formation mechanism, as formation via a disk processes—like core-accretion or gravitational instability— is likely to result in distinct atmospheric composition compared to earlier fragmentation of the collapsing core in a binary-like formation process. (e.g, Pollack et al., 1996; Boss, 1997; Boley et al., 2011).

In the second part, I discuss probes of small spatial scales around the super-massive black hole at the center of our galaxy. The black hole apparently lacks an optically thick accretion disk analogous to those seen around young stars, and instead accretes via a low-luminosity dynamically hot mechanism that is poorly understood. A population of massive stars orbiting the black hole is currently in a post main-sequence wind phase (Krabbe et al., 1995) and supplies the region with the raw material that is fueling the flow. The orbits of the inner-most stars and short-timescale variability of the emission from the accretion flow can both be used to probe the region within a few light-hours of the super-massive black hole. These probes will provide unique constraints on the shape of the gravitational potential, and will contribute to a better understanding of low-luminosity accretion mode that may be ubiquitous among quiescent galactic nuclei.

1.1 Star and Planet Formation

Disks are an inevitable part of the star and planet formation mechanism through which the gas and dust of interstellar material is processed and accreted onto protostars. In the following I explain why disks must form during the gravitational collapse of interstellar clouds, a theory for how gas is accreted through them, and how they set the stage for planet formation.

1.1.1 Protoplanetary Disks

Disks are a consequence of the conservation of angular momentum and the contraction of interstellar gas during the star-formation process. The angular momentum of a system is related to its mass M , radius R , and angular velocity ω , according to

$$L \propto MR^2\omega. \quad (1.1)$$

Thus, to keep L constant during a contraction with no mass loss, if R is reduced by a factor of x , then the angular velocity must increase by a factor of x^2 .

Consider the amount of contraction necessary to form a star from interstellar gas. The minimum length scale that an over dense region in an interstellar molecular cloud must attain before gravitational collapse can proceed is known as the Jeans length. For a core of mass M and radius R , the Jeans length can be derived by requiring that the internal gravitational energy

$$U \approx \frac{-GM^2}{R}, \quad (1.2)$$

with G Newton's gravity constant, can exceed the internal kinetic energy:

$$K \approx Nk_bT \approx \frac{M}{m_p}k_bT, \quad (1.3)$$

where N is the total number of gas particles, k_b is Boltzmann's constant, m_p is the typical mass of a particle, and T is the temperature of the gas. That is, we expect the onset of gravitational collapse to occur when

$$|U| \gtrsim K, \quad (1.4)$$

$$\frac{GM^2}{R} \gtrsim \frac{M}{m_p} k_b T, \quad (1.5)$$

$$R \gtrsim \sqrt{\left(\frac{k_b}{Gm_p}\right) \frac{T}{\rho}}, \quad (1.6)$$

where in the last step I have used

$$M \sim R^3 \rho, \quad (1.7)$$

to replace M in favor of ρ . For the typical temperature (~ 10 K) and density ($\sim 1000 \text{ cm}^{-3}$) of star-forming gas (e.g., Bergin and Tafalla, 2007), the Jeans length is ~ 0.3 pc. In order to become a star (radius $\sim 10^{10}$ cm), the gas must contract by a factor of ~ 10 million. For homologous collapse, the conservation of angular momentum demands that the rotation rate of the gas increases by a factor $\sim 10^{14}$. Thus, even if the initial core had near-zero rotation, by the late stages of contraction rotation becomes a dominant feature of the dynamics.

The centrifugal force due to rotation can support the gas against gravity in the direction perpendicular to the rotation axis, preventing collapse to stellar scales. Gravity squeezes the material much more effectively in the direction parallel to the rotation axis. The result is a disk of rotating material. The final steps of star-formation must some-how redistribute the angular momentum in the disk, allowing most of the disk mass to flow onto the star and a fraction of the mass to carry away the angular momentum.

Fragmentation and mass-loss can help alleviate some of the challenges to star-formation presented by the angular momentum problem. Note that in Equation 1.6, for the minimum length-scale susceptible to gravitational collapse, a factor of ρ is in the denominator. This means that as collapse proceeds, and density increases, the Jeans length is reduced, so collapsing clouds are prone to fragmentation—as long as the collapse remains approximately isothermal (as opposed to adiabatic). Fragmentation reorganizes the total angular momentum, distributing it between the fragments (orbital angular momentum) and within them (internal angular momentum). Further collapse to stellar scales must only overcome the internal angular

momentum. Mass loss of high-angular momentum material also helps reduce the angular momentum barrier by directly removing angular momentum from the system. Magnetic fields are thought to play a large role in mass loss processes (e.g., McKee and Ostriker, 2007).

Some intuition about the physical structure of protostellar disks is important to begin exploring the types of processes that act within them to allow material to fall onto the star and to grow into planets. A fiducial model is called the minimum mass solar nebula (MMSN, Weidenschilling, 1977b; Hayashi, 1981). The MMSN is a theoretical construct, created to understand the disk phase of our own solar system. The MMSN is built by first augmenting the mass of each planet in the solar system with enough gas so that its average metallicity matches that of the sun. Next, the augmented mass is distributed in concentric annuli. The result is a disk with a surface density profile, $\Sigma(r)$, which falls off with radial distance r from the protosun like

$$\Sigma(r) \approx 1.7 \times 10^3 \left(\frac{r}{1\text{AU}}\right)^{-\frac{3}{2}} \text{gcm}^{-2}, \quad (1.8)$$

using the normalization of Hayashi (1981). The implied total mass of this disk is $\sim 0.01 M_\odot$. A similar approach for estimating the mass and structure of protoplanetary disks uses multi-planet systems orbiting other stars (Kuchner, 2004; Chiang and Laughlin, 2013). These studies, find an even steeper power-law profile of the disk surface density with an index of ~ -2 . All of these models implicitly assume that planets formed at their current positions with no radial migration, which is not particularly well justified.

The vertical structure of the disk can be derived for each radius by requiring that the vertical pressure gradient balance the vertical component of gravity (Pringle, 1981). For a disk assumed to be vertically isothermal, the vertical density profile can be shown to be:

$$\rho(z) = \rho_0 e^{-z^2/2h^2}, \quad (1.9)$$

where ρ_0 is the midplane density, and h is the scale height of the disk, given by the

ratio of the sound speed of the disk material, c_s , to the orbital frequency, Ω

$$h = \frac{c_s}{\Omega}. \quad (1.10)$$

A natural mechanism for redistributing angular momentum in a fluid disk with radial shear is viscosity. The timescale for viscous evolution in a protoplanetary disk can be derived using the conservation of angular momentum and the continuity equation for the special case of Keplerian orbital velocity at each radius (e.g., Pringle, 1981). The result is that the characteristic timescale for protoplanetary disk evolution is

$$\tau \approx \frac{r^2}{\nu}, \quad (1.11)$$

where r is a characteristic radius of the disk, and ν is the viscosity. Molecular viscosity can be estimated as

$$\nu \sim lc_s, \quad (1.12)$$

where l is the mean free path of gas particles,

$$l = (n\sigma)^{-1}, \quad (1.13)$$

where n is the number density of particles and σ is their collisional cross-section. The gas sound speed, c_s , depends on the temperature T and the average particle mass μ , according to

$$c_s = \sqrt{\frac{k_b T}{\mu}}. \quad (1.14)$$

To calculate the molecular viscosity for molecular hydrogen gas ($\mu \sim 2m_H$, $\sigma \sim 2 \times 10^{-15} \text{ cm}^2$, Chapman and Cowling, 1970)), we need the disk density and temperature. We can use the MMSN. At 1 AU, the MMSN should have $n \sim 4 \times 10^{14} \text{ cm}^{-3}$ and $T \approx 280 \text{ K}$, which corresponds to $c_s \approx 1 \times 10^5 \text{ cm s}^{-1}$, implying a viscosity, $\nu \sim 1.5 \times 10^5 \text{ cm}^2 \text{ s}^{-1}$. Thus, the timescale for viscous evolution of a protoplanetary disk due to molecular viscosity is $\sim 10^{13} \text{ yr}$, $\sim 10^3$ times the age of the universe. Obviously, molecular viscosity cannot be responsible for the evolution of protoplanetary disks, which have observationally constrained lifetimes of $\lesssim 10^7 \text{ yr}$ (e.g., Mamajek et al., 2004).

Shakura and Sunyaev (1973) developed a theory for the viscous evolution of accretion disks assuming that some unknown mechanism (other than molecular interactions) acts as a viscosity. A prime candidate for the unknown mechanism is turbulence. The mean free path for turbulent cells in the disk can be much much greater than the mean free path from individual gas particles while the velocity of such cells can remain close to the sound speed. In this case, the problem becomes identifying a robust mechanism for driving turbulence in the protoplanetary disk. One such mechanism, the magneto-rotational instability (Balbus and Hawley, 1991), is a likely candidate.

The magneto-rotational instability is caused by differentially rotating parcels of ionized gas that are connected by a magnetic field line. As the gas with higher rotational velocity attempts to rotate past the slower parcel, its motion is impeded by the field line which is frozen into the ionized gas. Likewise, the slower parcel receives a pull forward by the faster gas. Thus a torque is present whereby angular momentum can be transferred from the inner fast-rotating parcel to the outer slow-rotating parcel. This situation is unstable because the nature of Keplerian orbits is that high angular momentum objects orbit at greater radius and with slower angular velocity, while low angular momentum objects orbit closer in and with higher angular velocity, so the fast get faster and the slow get slower, amplifying the effect.

The magneto-rotational instability can only operate in gas that is sufficiently ionized to couple to the magnetic field. In protoplanetary disks, the extreme radii—near ($r \lesssim 1$ AU) and far ($r \gtrsim 10$ AU) from the protostar—are sufficiently ionized through their whole widths. Close in, sufficient ionization is facilitated by heat from the protostar, and far out the ionization is facilitated by cosmic rays that can penetrate all the way to the midplane because of the reduced surface density at large radius. At intermediate radii, the disk is not sufficiently heated by the protostar and cosmic rays only sufficiently ionize an outer layer of the disk. This scenario leads to the idea of a dead-zone, or zone where no accretion takes place, near the midplane of the disk at intermediate radii (Gammie, 1996). Whether such a dead zone actually exists in protoplanetary disks—and understanding the magneto-

hydrodynamical implications of such a zone on disk evolution and planet formation—remains an important open question in this field (Armitage, 2011).

In Chapter 2, we explore these questions with observations of protoplanetary disks in the UY Aur binary star system.

1.1.2 The Formation of Gas-Giant Planets

In the last decade a population of directly-imaged companions orbiting nearby ($\lesssim 100$ pc) young ($\lesssim 100$ Myr) stars has been revealed by high-resolution imaging surveys. Many of these objects have masses at or near the deuterium burning limit ($\sim 13 M_{\text{Jup}}$), suggested by the International Astronomical Union (IAU) as the maximum mass for extrasolar planets. Advances in the search for the lowest-mass components of nearby star associations have revealed young isolated objects with masses below the deuterium burning limit, suggesting that the star formation process likely extends to very low masses (Luhman, 2012). Thus, it is important to understand whether the directly imaged companions are an extension of the planet formation process to high masses, or of the star formation process to low masses.

The planet formation mechanism that produced our solar-system planets produced gas giants that are metal-enriched compared to our sun. Metal enrichment may be an important indicator that a companion orbiting a distant star formed via a similar mechanism. The core-accretion process for gas-giant planet formation as well as gravitational fragmentation of the protoplanetary disk are both capable of producing metal-enriched planetary atmospheres (Pollack et al., 1996; Boss, 1997; Boley et al., 2011). Furthermore, because of the radial temperature gradient in protoplanetary disks, certain chemical species will be removed from the gas phase at radii corresponding to their freeze-out temperatures. This will result in distinct elemental ratios in the planetary atmosphere that may be diagnostic of the radial position at which a given planet formed in a disk (e.g., Öberg et al., 2011). On the other hand, if a companion is produced via gravitational fragmentation of the initial dense molecular cloud core, no large compositional differences are expected.

All of the suggested formation mechanisms for directly imaged planets face sig-

nificant physical challenges. The main road block for the core-accretion theory is the formation of the initial planetary core on a timescale shorter than the gas dissipation timescale. Aggregation of sub-micron dust particles in the protoplanetary disk to larger and larger scales is complicated by two distinct barriers that impede growth past size scales ~ 1 m. One barrier is the tendency, seen in terrestrial experiments, of collisions with particles larger than ~ 10 cm to result in erosion or fragmentation, not growth (Blum and Wurm, 2008).

A second barrier is aerodynamic. Gas in the disk is partially supported by a pressure gradient because the disk gets hotter and more dense at shorter radii. This fact causes gas to orbit slightly slower than the Keplerian velocity expected given the mass of the protostar. Solids in the disk are not supported by the radial pressure gradient, so orbit at the Keplerian speed (Weidenschilling, 1977a). The different orbital velocities of solids and gas subjects the solid bodies to a headwind that produces a drag. Basic intuition regarding the nature of the drag force can be gained by considering the gas pressure force on the leading and trailing sides of the particle. For a particle with radius a and moving with relative velocity v with respect to gas with a density ρ and sound speed c_s , the force on the leading side is

$$F_{\text{lead}} \approx \pi a^2 \rho (c_s + v)^2, \quad (1.15)$$

and the pressure force on the trailing side is

$$F_{\text{trail}} \approx \pi a^2 \rho (c_s - v)^2. \quad (1.16)$$

Thus, the net force on the particle is

$$F_{\text{drag}} \approx 4\pi a^2 \rho c_s v. \quad (1.17)$$

This drag force, called the Epstein drag, is only strictly applicable to small particles but is sufficient for illustrating the nature of the conceptual challenge to planetesimal growth posed by aerodynamic drag.

This drag will set a timescale for significantly altering the momentum of a particle,

$$t_{\text{drag}} \approx \frac{mv}{F_{\text{drag}}} \approx \frac{mv}{4\pi a^2 \rho c_s v} \approx \frac{\rho_{\text{solid}} a}{4\rho c_s}. \quad (1.18)$$

In the above equation m is the mass of the particle, and in the last step, I have substituted m with $\frac{4}{3}\pi a^3 \rho_{\text{solid}}$, where ρ_{solid} is the density of the solid material.

The dimensionless stopping time of a solid particle is

$$\tau_{\text{stop}} = t_{\text{drag}} \Omega_K, \quad (1.19)$$

where Ω_K is the Keplerian orbital frequency.

Equation 1.18 reveals that the drag timescale, and the stopping time, is a function of particle radius, $\tau \propto a$. If the stopping time of a particle is very small, then the gas can completely modify the momentum of the particle many times per orbit. In this case the particle is tightly coupled to the gas and will orbit with the gas. If the stopping time is very large, then the gas can never significantly alter the particle's momentum. In this case, the particle—probably a large planetesimal—is decoupled from the gas and will orbit at the Keplerian velocity. For intermediate sizes, with $\tau_{\text{stop}} \sim 1$, the particle is not completely coupled or decoupled from the gas. In this case, the particle will spiral into the star. For the typical conditions in a protoplanetary disk at 1 AU from the protostar, solids with a radius ~ 0.1 – 1 m should spiral into the star in ~ 100 y, a timescale much much shorter than the several million years necessary to form a planet. Thus, it is clear that the formation of planetesimals must be very rapid.

Youdin and Goodman (2005) suggested an instability capable of concentrating small particles in protoplanetary disks to the point where self-gravity can bind the particles, leaping over the meter-sized barrier. The instability relies on the tendency of solid particles to move toward local pressure maxima (arising from turbulence in the disk) in the presence of gas drag in a Keplerian potential. When the back-reaction of the dust on the gas is considered, a runaway can occur because Coriolis forces can balance pressure-gradient forces as the perturbation grows (e.g., Jacquet et al., 2011). Johansen et al. (2007) conducted a numerical experiment to understand the effects of this instability. They demonstrated the formation of dwarf-planet sized objects via the accretion of particles with $\tau_{\text{stop}} \sim 1$ in ~ 10 orbits.

The core-accretion mechanism for the formation of gas-giant planets (e.g., Pollack

et al., 1996) relies on these $r \sim 1000$ km planetesimals growing to $\sim 10 M_{\oplus}$ before the dissipation of the gas in the protoplanetary disk (~ 10 Myr). The agglomeration of large planetesimals is regulated by their dynamical interactions that increase their relative velocities, decreasing the effect of gravitational focusing and the probability of a constructive collision. The rapid growth of planetesimals is likely facilitated by gas drag which results in the efficient accretion of particles with $\tau_{\text{stop}} \sim 1$ (Ormel and Klahr, 2010). Lambrechts and Johansen (2012) showed that this decreases the timescale for planetary-core formation by several orders of magnitude compared to models where planetesimals themselves coalesce, possibly allowing giant-planet cores to form at $r \gtrsim 40$ AU.

The main hurdle for explaining directly imaged companion formation via gravitational instability, which would by-pass the challenges of planetary core formation, is that protoplanetary disks appear to be quite stable in all but the hottest and most massive disks (Matzner and Levin, 2005; Kratter et al., 2008). Since Keplerian disks are differentially rotating, with gas closer to the protostar completing orbits much faster than gas farther out, gravitational collapse within the disk can only occur if the timescale for collapse of a parcel with extent equal to the Jeans length is shorter than the timescale for the shear from the differential rotation to tear the parcel apart. The ratio of these two timescales is called the Toomre Q parameter (Toomre, 1964),

$$Q = \frac{c_s \Omega}{\pi G \Sigma}. \quad (1.20)$$

Gravitational instability is reached when $Q \lesssim 1$.

Even if gravitational instability is reached in a protoplanetary disk, the result may not be fragmentation and the production of a planet. Fragmentation requires an additional cooling constraint to be met (Gammie, 2001). If a gravitationally unstable parcel cannot cool fast enough, then it cannot condense into a fragment before orbital shear can disrupt it. In this case, gravitational instability will simply drive turbulence (Gammie, 2001), or result in the formation of global disk structures such as spiral arms (Lodato and Rice, 2004). In the hot massive disks where gravitational instability and adequate cooling rates can be attained, it is hard to understand how

to turn off accretion before an object reaches stellar mass (Kratter et al., 2010).

In chapter 3, I discuss work intended to further our ability to characterize the products of the planet formation process. By studying the atmospheres of young directly imaged companions orbiting nearby young stars, we can constrain the composition of the objects. Specifically, I discuss commissioning the L-band spectroscopic mode of Clio2, the infrared instrument behind the Magellan adaptive optics system. This instrument is capable of providing low spectral resolution spectra of directly imaged planets in the wavelength regime where they are expected to be brightest. Recent studies of directly imaged planets using narrow band photometric measurements in the L-band have demonstrated the power of $2.9\text{--}4\ \mu\text{m}$ constraints in guiding models and inferences about the state and composition of their atmospheres (e.g., Skemer et al., 2014, Skemer et al., submitted). The L-band is particularly valuable in characterizing directly imaged planets because of the presence of the P, Q, and R-branch fundamental methane bands, which allow for sensitive probes of disequilibrium carbon chemistry, and because cloud properties can be inferred based on their effect on the general slope of the L-band spectra.

1.2 The Super-Massive Black Hole at the Center of the Galaxy

1.2.1 Probing the Gravitational Potential of a Super-Massive Black Hole with Improved Astrometry of Stellar Orbits

Early observations of the Ne II emission from gas within 1 pc of the dynamical center of our galaxy suggested the presence of a large central mass, $\sim 4 \times 10^6\ M_\odot$ (Wollman et al., 1977). However, since gas is subject to hydrodynamical forces in addition to gravity, gas kinematics are not the best probe of gravitational potentials. Stars provide a much better test-particle for probing the shape of gravitational potentials as their motions are dictated entirely by gravity. When Rieke and Rieke (1988) measured stellar dispersions in the same region with velocities only half that seen in the gas, they suggested that a central compact mass $\sim 4 \times 10^6\ M_\odot$ was not necessary (though still possible) and that certain radial distributions of the stellar population

at the galactic center could account for the velocities they observe.

Continued monitoring with ever increasing sensitivity and spatial resolution resolved stars even closer to the galactic center. After the first accelerations were detected in the motions of galactic center stars, the case for a compact mass became quite convincing (Ghez et al., 2000; Schödel et al., 2002). Currently Keplerian orbits for ~ 20 stars have been fit to ~ 20 yr of astrometric monitoring data (Ghez et al., 2008; Gillessen et al., 2009a). Some of the stars have been tracked through their entire orbits. These stars all seem to orbit a single point mass of $4.4 \pm 0.4 \times 10^6 M_{\odot}$. This mass all must be located within the closest approach of the star S-16, which has a peri-apse of only 40 AU.

The possibilities for the types of objects that could supply this mass and density are extremely limited (e.g., Genzel et al., 2010). The logical conclusion is that a super-massive black hole resides at the center of our galaxy.

Stars on highly elliptical orbits plunging deep into the black-hole's gravitational potential can be used as test-particles to test the predictions of general relativity (e.g., Weinberg et al., 2005). General relativity in the post-Newtonian approximation predicts several modifications to Keplerian orbital motion (Weinberg, 1972). The magnitude of these effects is small but generally grows linearly with the number of orbital revolutions and increases with increasing proximity to the black hole (Rubilar and Eckart, 2001). Thus, precise astrometric measurements of the shortest period stars is essential.

Currently, stellar crowding in the dense nuclear cluster limits sensitivity to faint stars and limits the astrometric precision with which brighter stars can be monitored (Fritz et al., 2010). These limits have precluded the detection of stars on orbits shorter than 11.5 years (Meyer et al., 2012) and have not provided the necessary precision to detect deviations from Keplerian motion (e.g., Ghez et al., 2008). The confusion noise imposed by the number of sources at the galactic center can only be overcome with higher resolution observations which better localize the light from each source.

One technique which can provide high-spatial resolution observations of galactic

center stars is long-baseline infrared interferometry. Interferometry is a technique that takes advantage of the wave nature of light to create interference patterns that can be analyzed to reveal high-spatial resolution information. A thorough review of infrared interferometry is provided in Chapter 4.

In order to work, interferometers must combine the light from each aperture almost exactly in-phase. A particular challenge to infrared interferometry is keeping the light from each aperture in phase in the presence of the aberrating effects of the Earth’s atmosphere.

Recent upgrades on the world’s largest infrared interferometers have provided dual-field phase referencing modes to increase sensitivity. In dual-field phase referencing, an interferometer simultaneously observes two fields on the sky: a field of scientific interest, and a nearby field containing a bright reference target. By monitoring the interference pattern in short-exposure images of the bright reference target, the phase of each aperture can be tracked and path length adjustments can be made to correct for optical delays imposed by the turbulent atmosphere. This enables longer integrations on the fainter science target. The improved sensitivity of infrared interferometers makes infrared interferometric observations of the galactic center feasible for the first time.

In Chapter 4, we report on simulated observations of the galactic center with infrared interferometers, exploring how these new modes may fare in future observations.

1.2.2 Accretion onto the Super-Massive Black Hole at the Center of our Galaxy

Coincident with the location of the mass inferred from stellar orbits is a compact non-thermal, radio (Balick and Brown, 1974), near-infrared (Genzel et al., 2003) and X-ray (Baganoff et al., 2001) source, now known to arise from the accretion flow feeding the black hole. Extinction by dust in the galactic plane precludes detection at uv and optical wavelengths, and the opacity of the Earth’s atmosphere prohibits ground-based observations in the far-infrared. The luminous source is called Sagittarius A* (Sgr A*). Short time-scale variability from Sgr A* provides another way to probe

small spatial scales near the black hole because variations occurring on a timescale t necessarily arise from spatial scales

$$R \lesssim ct, \quad (1.21)$$

where c is the speed of light. The radius of the event horizon of the $4 \times 10^6 M_\odot$ black hole is 0.08 AU ($\sim 17 R_\odot$), corresponding to a light crossing time of ~ 80 s. The variable emission is compact and coming from very near the black hole, deep in the gravitational potential well (Baganoff et al., 2001; Doeleman et al., 2008; Fish et al., 2011).

While variable emission is thought to arise from the deepest parts of the accretion flow, the radiative processes responsible for the emission are not fully understood. This shortfall limits our ability to use variable features as probes of the accretion physics and black hole gravitational potential.

Some models for the variable emission have been tuned to fit multi-wavelength data (e.g., Eckart et al., 2009; Yusef-Zadeh et al., 2008; Haubois et al., 2012; Yusef-Zadeh et al., 2010). Many include the adiabatic expansion of a transiently heated synchrotron emitting blob (Eckart et al., 2009; Yusef-Zadeh et al., 2008). However, the role of inverse-Compton scattering and electron cooling in producing the observed variability seen in IR and X-ray bands is challenging to constrain with current data (Dodds-Eden et al., 2009). Dodds-Eden et al. (2010) and Haubois et al. (2012) suggest that the variability is powered by magnetic reconnection events, analogous to those seen on the sun. Magnetic reconnection can explain a tentative anti-correlation seen in variability light-curves between X-ray peaks and submillimeter flux, however Yusef-Zadeh et al. (2010) suggest that the submillimeter dips coincident with X-ray peaks are due to obscuration.

One way to constrain the physics of the variable emission is to make simultaneous observations across a wide spectral range. Such observations can help identify the specific radiative mechanism responsible for producing the electro-magnetic emission. Another way to better understand the physics of the accretion flow is to analyze the statistical characteristics of the variability. This analysis can help identify the

dynamical processes within the accretion flow that give rise to the emission.

In chapter 5, I discuss using both approaches to characterize variability at sub-millimeter wavelengths. In particular I report the first ever detection of Sgr A* at 0.25 mm, a wavelength that is impossible to observe from the ground due to the opacity of the Earth's atmosphere.

CHAPTER 2

Variable Accretion Processes in the Young Binary-Star System UY Aur[†]

We present new K-band spectroscopy of the UY Aur binary star system. Our data are the first to show H₂ emission in the spectrum of UY Aur A and the first to spectrally resolve the Br γ line in the spectrum of UY Aur B. We see an increase in the strength of the Br γ line in UY Aur A and a decrease in Br γ and H₂ line luminosity for UY Aur B compared to previous studies. Converting Br γ line luminosity to accretion rate, we infer that the accretion rate onto UY Aur A has increased by $2 \times 10^{-9} \text{ M}_{\odot}\text{yr}^{-1}$ per year since a rate of zero was observed in 1994. The Br γ line strength for UY Aur B has decreased by a factor of 0.54 since 1994, but the K-band flux has increased by 0.9 mags since 1998. The veiling of UY Aur B has also increased significantly. These data evince a much more luminous disk around UY Aur B. If the lower Br γ luminosity observed in the spectrum of UY Aur B indicates an intrinsically smaller accretion rate onto the star, then UY Aur A now accretes at a higher rate than UY Aur B. However, extinction at small radii or mass pile-up in the circumstellar disk could explain decreased Br γ emission around UY Aur B even when the disk luminosity implies an increased accretion rate. In addition to our scientific results for the UY Aur system, we discuss a dedicated pipeline we have developed for the reduction of echelle-mode data from the ARIES spectrograph.

[†]This chapter has been published previously as Stone et al. (2014). My roles included writing the necessary telescope proposal, planning the observations, designing the calibration strategy, executing the observations, developing the necessary computer software to perform calibrations, quantitative analysis of the results and writing the paper. I benefited from helpful conversations with the Co-authors, especially Josh Eisner and Colette Salyk. Don McCarthy and Craig Kulesa built the instrument.

2.1 Introduction

A large fraction ($\sim 30\%$) of all main sequence stars in the galactic disk are in binary or multiple systems (e.g. Lada, 2006). The main-sequence binary fraction is a function of spectral type, varying from near 100% for early type stars down to $\sim 20\%$ for late M-type stars (Raghavan et al., 2010, and references therein). While observations of rich star-forming clusters seem to exhibit a binary fraction consistent with the main sequence value, loose star-forming associations show considerable excess (Duchêne, 1999, and references therein). In fact, surveys of the young low-mass stars in the Taurus-Auriga star-forming region indicate a binary fraction of $\gtrsim 75\%$ (Ghez et al., 1993; Leinert et al., 1993; Kraus et al., 2011). Furthermore, young classical T-Tauri star binaries appear to be more co-eval than random pairings of stars within a cloud, implying the binary formation mechanism operates within ~ 1 Myr (Prato and Simon, 1997; Duchêne, 1999; White and Ghez, 2001; Hartigan and Kenyon, 2003). The high incidence of binaries in loose star forming regions implies that formation in multiple systems is the norm (see e.g. Duchêne and Kraus, 2013, for a recent review). While the multiplicity statistics of dense star-forming regions do not show significant excess over the main-sequence, it is still undetermined whether stars form with different multiplicity statistics in these environments, or whether shorter dynamical times accelerate the disruption of multiple systems (Duchêne and Kraus, 2013).

It is important to understand the details of the binary-star formation process given the significance of binary-star formation both as a substantial contributor to the galactic stellar population and in influencing planet formation and stellar feedback.

Theoretical studies have elucidated how dynamical resonances and tidal torques conspire to open a gap in a viscous circumbinary disk (e.g. Lin and Papaloizou, 1979). Matter can accrete through such gaps in geometrically thin streams (e.g. Artymowicz and Lubow, 1996). Studies of the flow from the circumbinary disk onto the circumstellar disks indicate that the primary star should have the more massive disk, however, model predictions of which star is preferentially fed new material seem

to depend on the adopted viscosity (e.g. Bate and Bonnell, 1997; Ochi et al., 2005). Recently sub-mm observations of young binary stars have revealed some systems where the secondary is host to the most massive disk, possibly implicating multiple formation modes for binary stars (Akeson and Jensen, 2014).

UY Aur is a Classical T-Tauri star binary system. The stars are separated by $0.9''$ (~ 120 AU). When Joy and van Biesbrok (1944) first identified UY Aur as a binary in the optical, the authors reported a $\Delta m \approx 0.5$. A few decades later, Herbst et al. (1995) could not detect the secondary and placed a lower limit of $\Delta m \approx 5$ at R-band. UY Aur has since been observed as a binary in the infrared (e.g. Ghez et al., 1993; Leinert et al., 1993; Close et al., 1998; Brandeker et al., 2003; Hioki et al., 2007). Resolved near-infrared photometry by Close et al. (1998), Brandeker et al. (2003), and Hioki et al. (2007) demonstrated that the flux ratio is variable in the infrared as well. Combining the H-band measurements of Close et al. (1998), and Hioki et al. (2007), UY Aur A varied relatively little, changing by $\lesssim 0.4$ magnitudes over 3 epochs in 10 years. UY Aur B, on the other hand, varied by up to 1.3 magnitudes in the same time.

Herbst et al. (1995) performed spatially resolved K-band spectroscopy of both sources. Those authors showed that UY Aur B exhibited strong $\text{Br}\gamma$ and H_2 $v=1-0$ S(1) emission lines, while UY Aur A showed none. $\text{Br}\gamma$ is a canonical accretion tracer, and their observations showed that UY Aur A can spend some time in a state with a very low accretion rate. The presence of H_2 $v=1-0$ S(1) emission without H_2 $v=2-1$ S(1) emission led Herbst et al. (1995) to believe it was arising in a shock. They suggested that the shock could arise from a stellar wind originating from UY Aur A and impacting circumstellar material around UY Aur B.

Millimeter molecular line observations revealed a Keplerian disk surrounding the stars (Dutrey et al., 1996; Duvert et al., 1998). The disk has an inner rim of ~ 500 AU (Hioki et al., 2007). By studying the reflected infrared light from the circumbinary disk, Close et al. (1998) was able to deduce a small/unrefined dust grain distribution. When Skemer et al. (2010)—using spatially resolved N-band spectroscopy—found a similar distribution of dust grains in the *circumstellar* disk of UY Aur A, they noted

that either something is prohibiting the evolution of grains in the stellar disk, or the grains are being replenished from the circumbinary reservoir, a clue that material is making its way from the circumbinary disk to the circumstellar disks, as predicted by theory.

Throughout this paper we assume the stellar spectral types and masses deduced by Hartigan and Kenyon (2003). Using STIS on board *HST*, Hartigan and Kenyon (2003) obtained spatially resolved medium and low resolution spectra from 0.5–1 μm . They simultaneously fit their data for veiling, spectral type, and reddening. Their best fit for UY Aur A is a 0.6 M_{\odot} M0 type star with $A_v=0.55$. For UY Aur B, their best fit parameters indicate a 0.3 M_{\odot} , M2.5 type star with $A_v=2.65$. The significant difference in extinction toward each source is uncommon among their sample, but is consistent with the large change in observed flux of UY Aur B between the 1940's and 1990's. In fact, variable reddening has been suggested as the driver of the NIR variability in UY Aur B (e.g. Brandeker et al., 2003).

Here we report new spatially and spectrally resolved observations of UY Aur. We present the first detection of H_2 lines in the spectrum of UY Aur A, and the first spectrally resolved measurement of $\text{Br}\gamma$ in the spectrum of UY Aur B. We highlight a significant change in the relative strengths of both the $\text{Br}\gamma$ line and the H_2 v=1-0 S(1) line between our observations and the only other published K-band spectrum of UY Aur B (Herbst et al., 1995).

2.2 Observations and Reduction

We observed both components of UY Aur on 3 October 2012 UT using ARIES on the MMT. ARIES is optimized for diffraction limited observations behind the MMT adaptive optics system. We used the f/5.6 (0.1"/pixel) echelle mode with a 1"x0.2" slit. This mode is designed to provide $\gtrsim 20$ cross-dispersed spectral orders at a resolution of $R \approx 30,000$. Our setup targeted a wavelength range of $\sim 1.6\mu\text{m} - 2.47\mu\text{m}$ with some gaps between orders. The adaptive optics provided 0.2" FWHM PSFs on the imaging side of ARIES and we realized 0.4" FWHM spatial profiles on the spectrograph side. The degraded spatial profile is most likely due to one of

the optics on the spectrometer side of ARIES. Measured argon-lamp emission lines indicate a realized spectral resolution of $R=15,000$.

Each component of the UY Aur binary was observed with the slit aligned along two anti-parallel position angles: 40° and -140° . This was done in order to help characterize instrumental effects on the spectral traces (e.g. Brannigan et al., 2006). An observing log is included in Table 5.1. We slewed off source to collect sky frames once for the pair of $PA=40^\circ$ observations and once for the pair of $PA=-140^\circ$ observations. Likewise, observations of the A7 star HR 1620 were made once for each position angle to facilitate the correction of telluric absorption features in our data. Flat field frames were collected to correct for inter-pixel variations in the detector gain.

To monitor instrumental flexure and spectral fringing effects, we collected flat field frames at each new pointing during the night. Dark frames to correct the flats were collected at the end of the night.

We developed a dedicated pipeline for the reduction of echelle-mode data from ARIES to analyze our observations. We began with subtracting sky frames from science frames, and dark frames from flat frames. We then dewarped the spectral orders using a fifth-degree two-dimensional polynomial coordinate transformation to map the curved stellar spectral traces to straight lines. Figure 2.1 shows an example of dewarping a flat-field frame using the transformation derived from the stellar traces. We used a fifth-degree transformation as this was adequate to ensure that the spatial dimension of each order was perpendicular to the spectral dimension, as we verified using observations of an Argon arc lamp (Figure 2.2).

After dewarping all the frames, we began defringing, beginning with the flats. The dominant frequency of the instrumental fringing is $\sim 0.01 \text{ pixels}^{-1}$. This corresponds to a fringe wavelength of $\sim 500 \text{ km/s}$. Our flat-defringing algorithm proceeded row-by-row in each order as follows. We first fitted and subtracted a third-order polynomial to the row. We then created a model of the fringe pattern using a Fourier filter which only passed frequencies less than $0.015 \text{ pixels}^{-1}$ (see Figure 2.3). Next, we subtracted this model fringe from the row it was created from and then added

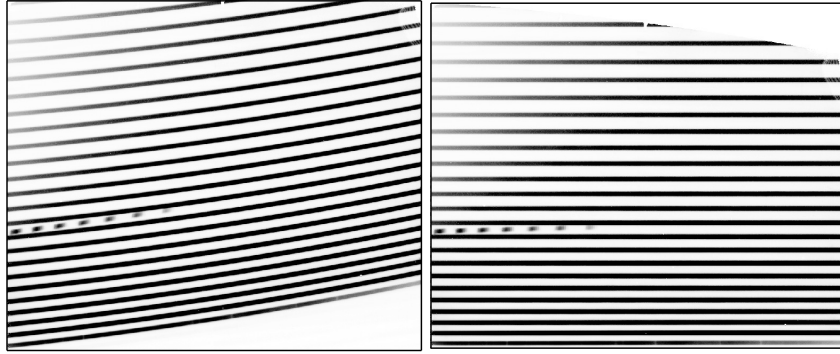


Figure 2.1: Dewarping a flat-field frame. On the left, we show an original warped image of a flat lamp with many curved orders. On the right we show the straight spectral orders after dewarping.

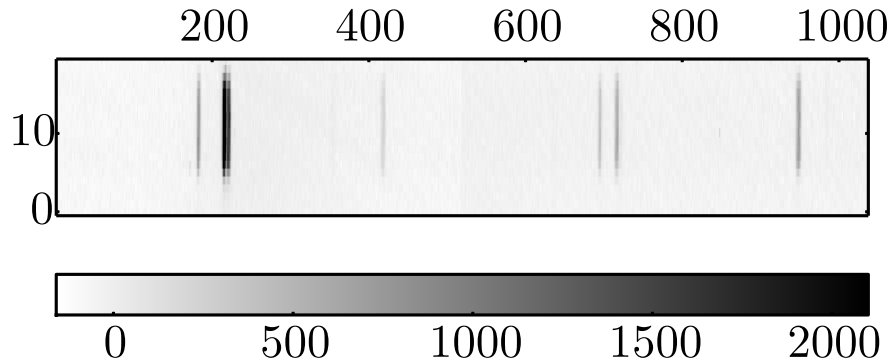


Figure 2.2: Argon arc lamp emission lines are rectified after using a fifth-degree two-dimensional polynomial transform.

back in the third-order polynomial that was previously subtracted. This was done in order to remove the fringing but maintain the very low frequency shape of the flat. We saved our derived model fringe in a template for later re-use in defringing the stellar spectra.

After defringing the flats, we divided the flat frames into the stellar spectra. Our next step was to extract from the two-dimensional spectral orders one-dimensional

spectra. To extract the 1-d spectra we first fit a Gaussian to the average spatial profile of the order. Then, for each column, we summed the light in each row $1\text{-}\sigma$ above and below the average spatial centroid.

With the stellar spectra extracted, our next step was to defringe them. We started with the telluric calibrator. Since sharp features have broad Fourier transforms, narrow telluric absorption lines in the telluric calibrator spectrum can bias the instrumental fringe model when using even a low-pass Fourier filter. To avoid this, before creating the model fringe, we first interpolated over telluric lines. We have illustrated this step in the top panel of Figure 2.4. We created a model fringe by first subtracting a best-fit low-order polynomial and then using a Fourier filter to pass only the spatial frequencies less than $0.015 \text{ pixels}^{-1}$ (see the middle panel of Figure 2.4). Finally, we subtracted this model fringe from the original spectrum to remove the instrumental fringing and then added back in the best-fit polynomial. Since our calibrator source, HR 1620, rotates quite quickly ($v \sin i = 131 \text{ km/s}$, Royer et al., 2002), our Fourier filtering approach had the ancillary effect of removing rotationally broadened photospheric lines. In the bottom panel of Figure 2.4, we compare to the observed telluric transmission spectrum provided by Hinkle et al. (2003). To facilitate the comparison, we show the spectrum of HR 1620 before we replace the best-fit polynomial shape.

Next, we performed a wavelength calibration on both the defringed telluric spectrum and the as-yet uncorrected target spectra. Wavelength calibration was done by fitting a fourth-degree polynomial to transform measured telluric absorption line pixel positions to the wavelengths of each line provided by Hinkle et al. (2003). We then divided the telluric calibrator spectrum into the target spectra to remove telluric absorption features. At this point, we summed the spectra from each PA for each target, creating one higher signal-to-noise spectrum for each source.

To defringe the target spectra, we interpolated over narrow emission lines and photospheric absorption lines before defringing. For broad features, such as the $\text{Br}\gamma$ emission line, we had to take care not to model out real emission while still generating an accurate model for the instrumental fringing. To do this, we first

Table 2.1. Observations

Source	Total Exposure Time [s]	Slit PA	Airmass
UY Aur A	899.1	40°	1.00
UY Aur B	899.1	40°	1.01
HR 1620	149.5	−47°	1.03
UY Aur B	899.1	−140°	1.04
UY Aur A	799.2	−140°	1.07
HR 1620	149.5	56°	1.05

Note. — Each member of the UY Aur binary was observed twice. Each observation was performed with anti-parallel slit orientations. We use HR 1620 to perform the telluric calibration. After performing a wavelength calibration and correcting for telluric lines in the spectra of UY Aur A and B, we sum over rotation angle to produce a single spectrum for each source.

generated a best-guess model fringe. Our best-guess fringe was created in two steps: 1) we extracted a one-dimensional flat-field fringe by summing the same rows in the template of saved flat fringes that were summed in the science frame during the extraction of the science spectrum, and 2) we fit this one-dimensional flat-field fringe to the target spectrum by adjusting the wavelength solution parameters to produce a closest match. We show this step in the top panel of Figure 2.5. Next we replaced spectral regions of known features in our observed spectra, with the corresponding region of our best-guess fringe down weighted by the addition of Gaussian noise. We then used a low-pass Fourier filter to generate a model fringe (middle panel of Figure 2.5). We repeated this process 1000 times, each time with a new realization of the Gaussian noise, to produce 1000 model fringes. The average of the 1000 model fringes we took as our fiducial fringe for defringing. The variation in the 1000 fringe models suggested the precision of our model fringe. In the bottom panel of Figure 2.5, we show a portion of the defringed spectrum of UY Aur A in the vicinity of $\text{Br}\gamma$, plotted with a blue swath. The width of the swath at each wavelength represents the $1\text{-}\sigma$ variation in the fringe model at that point.

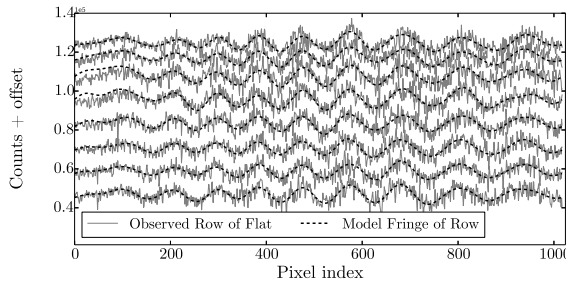


Figure 2.3: This plot illustrates, for one order, our approach to defringing the flat-field frames. A model fringe for each row was made using a low-pass Fourier filter. These models were subtracted from the flat, and saved for use in defringing the science targets. In this figure, the flux in each row is plotted versus pixel number in gray. Each row is manually offset for clarity. The model fringe is over-plotted with a dashed black line.

2.3 Results and Analysis

2.3.1 Equivalent Widths

We measured the equivalent width (EW) of the $\text{Br}\gamma$, H_2 $v=1-0$ S(1), and H_2 $v=1-0$ S(0) lines for both sources. For the broad $\text{Br}\gamma$ lines, we performed the EW measurement during the repetitive fringe modeling process (see Section 3.2). For each repetition, we generated and subtracted a new fringe model from the observed spectrum and measured the EW. To illustrate this process we show 10 repetitions in Figure 2.6. The mean and standard deviation of all 1000 EW measurements is our adopted EW and uncertainty, respectively. The defringing process appears to introduce $\sim 0.3 \text{ \AA}$ of uncertainty into our EW measurements for $\text{Br}\gamma$. We do not correct our measured EWs for photospheric absorption, in line with previous studies (Herbst et al., 1995; Fischer et al., 2011). Given the spectral types of the stars (M0 and M2 for UY Aur A and B, respectively Hartigan and Kenyon, 2003), even with zero veiling the effect on our measured EWs is 10%, within our measurement uncertainty.

For the narrow H_2 lines, we did not iterate to produce the fringe model because the H_2 lines are narrow compared to the fringing, and can be readily distinguished (see Section 3.2). To estimate our precision in the measurement of the EW of these

lines, we ascribed to each pixel in the line the same level of noise as measured in the nearby continuum. We then calculate the EW uncertainty to be $\sqrt{N}\sigma$, where N is the number of pixels in the line and σ is the measured noise level. All EW measurements are presented in Table 2.2.

2.3.2 Line Luminosities

To convert our EW measurements to line luminosities we used $D=140$ pc (Elias, 1978), and the K-band photometry of Close et al. (1998) for UY Aur A. For UY Aur B, which has shown significant NIR variability (e.g. Hioki et al., 2007), we determined the flux ratio to the primary using imaging data taken at the same time as our spectra. Line luminosities are not corrected for extinction. In Section 2.4 we discuss how variable extinction may effect the relative line luminosities. All resulting emission line luminosities are reported in Table 2.2.

2.3.3 Accretion Rates

We converted our measured $\text{Br}\gamma$ line luminosity to accretion luminosity, without correcting for extinction, using the correlation reported by Muzerolle et al. (1998). Accretion rates were derived from accretion luminosities using Equation 11 in Hartigan and Kenyon (2003) —which assumes that accreting material is in free fall from $3R_*$ when it hits the stellar surface and that half of the accretion energy is radiated directly, the other half heats the star. Our accretion rate measurements are listed in Table 2.2.

In Figure 2.7 we plot the accretion rate versus time for each source in the binary. The additional $\text{Br}\gamma$ derived accretion rates for UY Aur A were calculated using the EWs from Herbst et al. (1995) and Fischer et al. (2011) and the continuum flux level observed by Close et al. (1998). The flux level for UY Aur B is always deduced by comparing to UY Aur A. Since Herbst et al. (1995) and Fischer et al. (2011) do not report errors for their EW measurements we assign them our measured value of 0.3 \AA . This is probably conservative since most of our uncertainty comes from defringing. We use 0.05 magnitudes of uncertainty in the continuum flux level, the value reported

in Close et al. (1998). Some additional uncertainty in the flux level is accrued by using flux calibration data not collected in parallel with the spectroscopic observations. For example, young binary stars as a class can vary by $\gtrsim 0.4$ magnitudes in the NIR (e.g. Skrutskie et al., 1996; Hioki et al., 2007). However, since the flux ratio between A and B is measured, any untracked variability in the flux of UY Aur A will affect both components of the binary similarly, preserving the relative trends. In addition to Br γ derived accretion rates, we also include measurements using other techniques in Figure 2.7. With triangle and square symbols we show accretion rates derived using both optical veiling measurements (Hartigan and Kenyon, 2003), and Pf β measurements (Salyk et al., 2013), respectively.

The published Pf β -derived accretion rates (Salyk et al., 2013) appear to be at odds with the long-term trends in accretion rate inferred from Br γ and optical veiling measurements. A re-analysis of the NIRSPEC data suggests that the components were misidentified, and we correct that here. However, we caution that the NIRSPEC slit was misaligned with the binary PA during these observations, and this adds systematic uncertainty to the relative accretion luminosities derived from these data.

In Figure 2.8, we show the accretion rate ratio versus time for all epochs when the accretion rate was measured for both sources. Figure 2.8 shows that accretion was directed primarily toward the secondary component in the initial epoch, but transitioned to the primary over time. The timescale of the observed variability is much shorter than the ~ 2000 year dynamical timescale of the binary. Rather, the 5-10 year timescale corresponds to the orbital timescale at 2.5–5 AU from the $\sim 0.5M_{\odot}$ stars.

2.3.4 H₂ Lines

In Figure 2.9, we show portions of the stellar spectra near the molecular Hydrogen v=1-0 S(0) and S(1) lines and the v=2-1 S(1) line. We detect the v=1-0 S(0) and S(1) lines in both sources. A photospheric absorption line in the spectrum of UY Aur A complicates our ability to place a strong constraint on the v=2-1 S(1) line. We do not detect the line in the spectrum of UY Aur B.

Table 2.2. Equivalent Widths and Line Luminosities

UY Aur	m _K ^a	EW(Br γ) [Å]	L _{Brγ} ^b [L _⊙]	L _{acc} ^c [L _⊙]	\dot{M} ^d [M _⊙ yr ⁻¹]	EW(S(1)) [Å]	L _{S(1)} [L _⊙]	EW(S(0)) [Å]	L _{S(0)} [L _⊙]
A	7.42	-2.7(0.3)	7.3(0.8)E-5	1.6(0.2)E-1	3.5(0.5)E-8	-0.20(0.02)	5.4(0.5)E-6	-0.06(0.01)	1.6(0.4)E-6
B	7.67	-1.1(0.3)	2.3(0.5)E-5	0.4(0.1)E-1	1.2(0.4)E-8	-0.08(0.01)	1.7(0.2)E-6	-0.025(0.012)	0.5(0.2)E-7

^aThe K-band magnitude for UY Aur A is from Close et al. (1998). For UY Aur B, we determined the magnitude difference using our own measured flux ratio.

^bBr γ luminosities are not corrected for extinction, following the approach of previous studies. We discuss below the potential effects of strong extinction on the Br γ line of UY Aur B.

^cAccretion luminosity is derived using the correlation reported by Muzerolle et al. (1998)

^dMass accretion rates were derived using the stellar radii and masses reported in Hartigan and Kenyon (2003)

Note. — The uncertainty in each reported value is presented in parentheses. Luminosities were derived assuming a distance of 140 pc.

We have calculated the $v=1-0$ S(1) to S(0) ratio for each source. The ratios and associated uncertainty intervals are plotted in Figure 2.9. We have also converted these ratios to excitation temperatures using the transition probabilities of Wolniewicz et al. (1998). The implied temperatures, ~ 1025 K and ~ 750 K for UY Aur A and B, respectively, are also plotted in Figure 2.9. At these temperatures the $v=2-1$ S(1) line should be very weak, $\lesssim 1\%$ the intensity of the $v=1-0$ S(1) line. This is compatible with the absence of strong $v=2-1$ S(1) emission in our spectra. Since models of fluorescent diffuse gas predict that the strength of the $v=2-1$ S(1) line should be similar to, even greater than, the $v=1-0$ S(0) line (e.g. Black and van Dishoeck, 1987), we can rule out a large contribution to the H_2 line emission from fluorescent diffuse gas.

There are several ways to produce a thermalized spectrum of H_2 lines. Mechanisms include shock heating and UV/X-ray irradiation of dense gas. Shock heating, in an inflow or outflow, is expected to produce relatively broad lines ($\gtrsim 100$ km/s) offset from the continuum (e.g. Beck et al., 2008, 2012).

We observe lines that are unresolved (widths < 20 km/s) and not offset in velocity from the stellar photospheres. We detect no astrometric displacement along the slit (PA=40°). Our measured astrometric precision along the slit is ~ 0.5 AU. Given the observed $v=1-0$ S(1) line-to-continuum ratio for UY Aur A, ~ 0.1 , we constrain the bulk of the observed H_2 flux to be centered within 15 AU of the continuum at the $3-\sigma$ level. Furthermore, we see no significant increase in the line-to-continuum ratio of the H_2 lines when we extract spectra from the margins of our slit, $0.3'' - 0.5''$ (42 – 70 AU) from the continuum centroid. In these off-star extractions we can constrain any extended emission in the $0.3'' - 0.5''$ region, along a PA of 40°, to be less than $\sim 1 \times 10^{-13}$ ergs cm $^{-2}$ s $^{-1}$ arcsec $^{-2}$. Since we do not detect any spatial offsets or extension in the H_2 lines, it is difficult for us to directly implicate shocks with these data.

Assessing whether FUV or X-ray irradiation could be responsible for exciting the H_2 lines is difficult because no well characterized FUV spectrum exists for UY Aur. Nomura et al. (2007) used the spectrum of TW Hya to model the H_2 ro-vibrational

spectrum from a proto-planetary disk around a $0.5 M_{\odot}$ star. For the case with the smallest grains, they predict thermal line ratios and a $v=1-0$ S(1) line strength 2.5 times as strong as what we report here for UY Aur A. Since UY Aur has a weaker X-ray luminosity than TW Hya (by a factor of ~ 5 , Güdel et al., 2010), it is not surprising that UY Aur A has a somewhat weaker line strength than predicted by the Nomura et al. (2007) model. High density UV fluorescence combined with X-rays seems capable of generating much of the observed compact H_2 emission.

2.3.5 Veiling

Veiling is the ratio of excess flux (E_{λ}) over photospheric flux (P_{λ}) at a given wavelength:

$$r = \frac{E_{\lambda}}{P_{\lambda}}. \quad (2.1)$$

Since we did not observe photospheric calibrators for UY Aur A and B, making a quantitative measurement of the veiling toward each source is difficult. Without a photospheric template for each source we cannot characterize internal instrumental scattered light, which can artificially veil our spectra (see Eisner et al. (2010), for an example of instrumental veiling with ARIES). However, we can make a qualitative statement about the relative veiling between each source. In Figure 2.11 we show a portion of the spectra of both UY Aur A (top panel) and UY Aur B (bottom panel) in the vicinity of two strong Aluminum photospheric absorption lines. We also plot synthetic PHOENIX photospheric spectra (Husser et al., 2013). The model spectra represent stars with $\log g=4.5$ and $T_{\text{eff}}=3900$ K and $T_{\text{eff}}=3500$ K for UY Aur A and B, respectively. We veiled the synthetic spectra by $r = 0, 1.4, 3$, and 7 . The $r = 1.4$ value is that reported by Fischer et al. (2011) for UY Aur A. As shown in the figure, $r = 1.4$ matches our observation for UY Aur A well, suggesting that instrumental veiling is weak or absent. Our spectrum of UY Aur B shows significantly weaker absorption lines than the $\sim 10\%$ -depth lines observed in the R=250 spectrum reported by Herbst et al. (1995). Thus we report that a large change in the K-band veiling of UY Aur B has taken place since 1994.

2.4 Discussion

In the previous section we presented the second ever K-band spectrum of UY Aur B. We observe a ~ 0.9 magnitude increase in the flux of this source, together with increased veiling and decreased emission line luminosity. An increased circumstellar disk flux could explain both the increased K-band flux and the stronger veiling. Such an increase could be due to an episodic increase in the mass accretion rate through the disk. However, we must understand why the observed $\text{Br}\gamma$ luminosity, a tracer of accretion onto the star, has decreased even while accretion through the disk has increased.

One explanation appeals to a nearly edge-on viewing geometry to explain the increased luminosity of the disk and the decreased luminosity of the $\text{Br}\gamma$ line. Several observations of the system hint at an edge-on orientation, including the unusually discrepant visual extinctions toward UY Aur A and B (Hartigan and Kenyon, 2003), the extincted appearance of the 10-micron silicate feature (Skemer et al., 2010), and the large amplitude optical and NIR variability (e.g. compare Joy and van Biesbrok, 1944; Herbst et al., 1995; Close et al., 1998; Brandeker et al., 2003; Hioki et al., 2007). In this scenario, when the scale height of the disk responds to the increased accretion rate and temperature —becoming larger— our view of the star becomes more obscured by the inner disk rim. Thus, the intrinsic $\text{Br}\gamma$ luminosity can increase but be observed to decrease.

We estimate the level of increased K-band extinction necessary to produce the observed change in the $\text{Br}\gamma$ luminosity given an assumed factor for the increased disk luminosity. Measuring the increase in disk luminosity requires a previous quantitative measurement of the K-band veiling for UY Aur B, which does not exist. We can make a ballpark estimate assuming that the previous veiling was $r_K \lesssim 1$, a common value for other classical T Tauri stars (Fischer et al., 2011), and qualitatively consistent with the previous K-band spectrum (Herbst et al., 1995). For example, if the 0.86 magnitudes increase we observe in the K-band flux is driven by a factor of 3 increase in the luminosity of the disk, and we assume a similar increase in the intrinsic accretion

luminosity of material making it onto the star, then we expect a factor of 2.4 increase in the intrinsic $\text{Br}\gamma$ luminosity¹. However, the observed $\text{Br}\gamma$ line strength has decreased by a factor of 0.54. This implies that only 23% of the $\text{Br}\gamma$ luminosity is passing through the puffed up disk rim, an increase in A_K of 1.6.

We convert such an increase in A_K to a change in column density along the observed line of sight using a value for the K-band dust opacity. We use $\kappa_K = 10 \text{ cm}^2 \text{g}^{-1}$, compatible with models of T Tauri disk dust grains (Miyake and Nakagawa, 1993), to derive the required column density increase: 0.15 g/cm^2 . The fractional increase implied by such a change depends on the initial column density along our line of sight. Small fractional changes are required along lines of sight initially transecting optically thick portions of the inner rim while larger fractional changes are required along sight lines through more tenuous material. For example, if our sight line radially through the rim initially transected where $\tau = 1$, then a 3% change in the scale height of the disk is necessary. A 10% change in the scale height is required if our initial line of sight was through the rim at a height where $\tau = 0.2$. Using $L \propto T^4$, and assuming a hydrostatic disk, $h \propto c_s \propto T^{0.5}$, we expect a 14% increase in the scale height given our assumed increase in the luminosity of the disk.

Alternatively, if the observed decrease in the $\text{Br}\gamma$ flux and the increased disk luminosity implies an intrinsically lower accretion rate onto the central star, material flowing through the disk must accumulate at some radius or be ejected in an outflow before making its way onto the star. In a viscous accretion disk, mass is expected to pile up in regions with relatively low viscosity. Gammie (1996) described an accretion flow where the mid-plane of the disk at intermediate radii has very low viscosity because the gas, which is neutral there, is decoupled from the magnetic field. Mass is predicted to accumulate in these “deadzones”. Gammie (1996) pointed out that such an accumulation of mass would lead to instability, resulting either in the fragmentation of bound objects (e.g. planets) or in sufficient heating of the deadzone to ionize enough of the gas to couple the material there to the magnetic field, causing a sudden and dramatic increase in the accretion rate. If matter is indeed piling up

¹Using the correlation between accretion luminosity and $\text{Br}\gamma$ luminosity in Muzerolle et al. (1998)

in a deadzone, then we would expect UY Aur B to undergo outbursts in the future.

One clue that can help us understand the intrinsic accretion properties of UY Aur B is the observation of extended outflows. Mass-loss rates from young stars are correlated with mass accretion rates (e.g. Hartigan et al., 1995), and outflows can be used as a tracer of accretion. Recently, Pyo et al. (2014) reported the observation of extended outflows surrounding UY Aur. These extended outflows should not be extinguished by circumstellar disk material at small radii, and may give a clearer perspective on the intrinsic accretion rate of UY Aur B. Thus, time monitoring of outflow rates from UY Aur B will help to constrain the physics of the variability in this source.

Additionally, both of the H_2 excitation scenarios discussed above (shock or UV/X-ray excitation) should produce H_2 lines with intensity that correlates with the accretion rate. For shocks, a larger accretion rate should result in a larger outflow rate (e.g. Hartigan et al., 1995), strengthening the H_2 signal. An increased accretion rate should also produce a stronger UV and X-ray accretion-shock spectrum and strengthen the fluorescent excitation. Thus our observed decrease in H_2 line strength compared to the observations by Herbst et al. (1995) may indicate a decrease in the intrinsic accretion rate.

If the highly inclined geometry explanation for the behavior of UY Aur B is correct, we predict that veiling, total flux, and outflow tracers of accretion should be correlated, but that shock-tracers of accretion (such as H I lines like $Br\gamma$) should be anticorrelated. More frequent monitoring of this system will provide better knowledge of the nature and timescale of the variability and will be important in disentangling the physical state of UY Aur B.

Since the circumstellar disk around UY Aur A is not edge on (Akeson and Jensen, 2014), we predict that all tracers of accretion, veiling, and total flux should be correlated. Three epochs of published spatially separated K-band spectroscopy exist for UY Aur A. The accretion rate seems to be increasing $\sim 2 \times 10^{-9} M_{\odot} \text{yr}^{-1}$ per year. UY Aur A now has the larger observed $Br\gamma$ luminosity. In addition to the indicators included in our Figure 2.7, further evidence that UY Aur A has been trending toward

a more active state can be seen in the comparison of the He I line shapes of Edwards et al. (2006) and Pyo et al. (2014). In 2014, Pyo et al. (2014) observed deeper red and blue shifted absorption features than Edwards et al. (2006). This suggests more vigorous infall and outflow from the source.

Additional evidence that UY Aur A is now in an intrinsically more active state than UY Aur B comes from the relative outflow rates. Pyo et al. (2014) showed that UY Aur A was driving an outflow at a larger rate than UY Aur B in 2007, consistent with our Figure 2.7. However, if we assume the outflow is launched at the velocity observed by Pyo et al. (2014) in the [FeII] lines, ~ 150 km/s, then we expect ~ 2 year delay between variations in accretion at the stellar surface and variations in the observed outflow.

If UY Aur B is in fact accreting less than UY Aur A then we must understand why the more vigorous accretor in UY Aur seems to alternate between the primary and the secondary. Theory predicts that circumbinary disks should preferentially feed either the primary, as shown by Ochi et al. (2005), or the secondary as predicted by Bate and Bonnell (1997). One solution, which is consistent with the data, is that the accretion onto both sources, as traced by Br γ , is episodic. In this way the average accretion rate onto the primary or secondary could dominate over time. This scenario has significant implications for planet formation because intense bursts of accretion can alter the chemical make-up and particle distribution in the disk by dissociating molecules and evaporating dust.

Another option is that the UY Aur binary system is substantially different from modeled systems. For example, Bate and Bonnell (1997) and Ochi et al. (2005) modeled systems with the implicit assumption that the binary seeds result from a disk fragmentation process. The possibly mis-aligned inclinations of the circumstellar disks in UY Aur is a clue that UY Aur may not have formed via disk fragmentation. This more complicated scenario is not as easily compared to clear-cut theoretical predictions.

2.5 Conclusions

We have presented R=15,000 K-band spectroscopy of each star in the UY Aur binary system. Our spectrum of UY Aur B is only the second ever published and enables time domain studies at wavelengths probing both circumstellar material and accretion. We highlight significant changes since 1994. Specifically, we see that UY Aur A presents increased Br γ luminosity and now shows H₂ emission while UY Aur B shows a decrease in the strength of Br γ and H₂ emission. In contrast to the state of the system in 1994, UY Aur A now has the stronger observed Br γ line. Additionally, UY Aur B now appears significantly brighter and more heavily veiled than it has in the past.

We suggested two scenarios to explain the observed changes in the state of UY Aur B. Both cases include increased viscous accretion through the circumstellar disk to account for the increased luminosity and stronger veiling observed. In the first scenario a similar increase in the *intrinsic* Br γ line strength is attenuated by increased extinction due to a puffed-up edge-on disk. We showed that the change in the scale height of the disk that is necessary to produce the reduced Br γ line strength is compatible with the amount of change expected for a disk undergoing an episode of increased viscous accretion. Alternatively, the observed reduction in the Br γ line strength, and the accretion onto the star which it traces, is intrinsic. In this case, mass flowing through the disk must pile up or be ejected before it reaches the star. We predict, if the edge-on disk scenario is correct, that future higher cadence time-monitoring of this system will reveal an anti-correlation in the variability of shock-tracers of accretion (such as H I lines) and the observed disk luminosity and veiling.

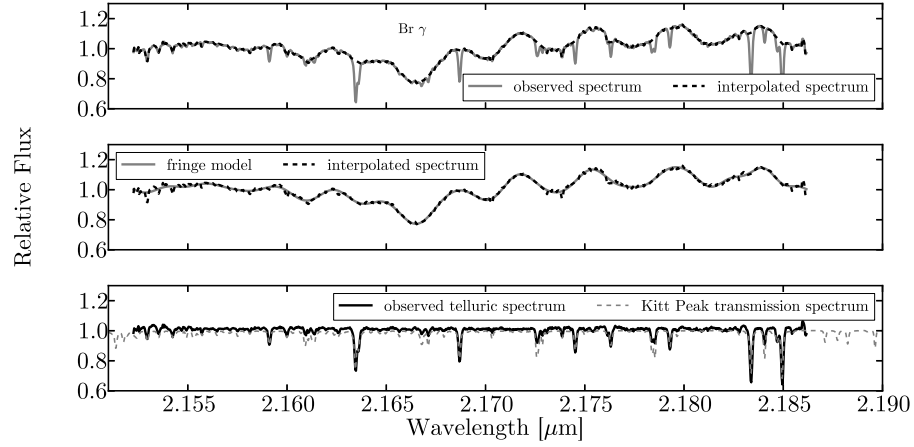


Figure 2.4: In order to defringe the orders of the telluric calibrator spectrum we first interpolated over narrow telluric absorption lines (top panel). We then used a low-pass Fourier filter to generate a model fringe. Since our calibrator is a fast rotator, this method also corrected for photospheric absorption (middle panel). In the bottom panel we show the spectrum of HR 1620 after subtracting the model fringe, which corrected for both the instrumental fringing and the photospheric absorption. The technique of interpolating over sharp features before generating a model fringe was also applied to the orders of the UY Aur spectra which included narrow H_2 lines.

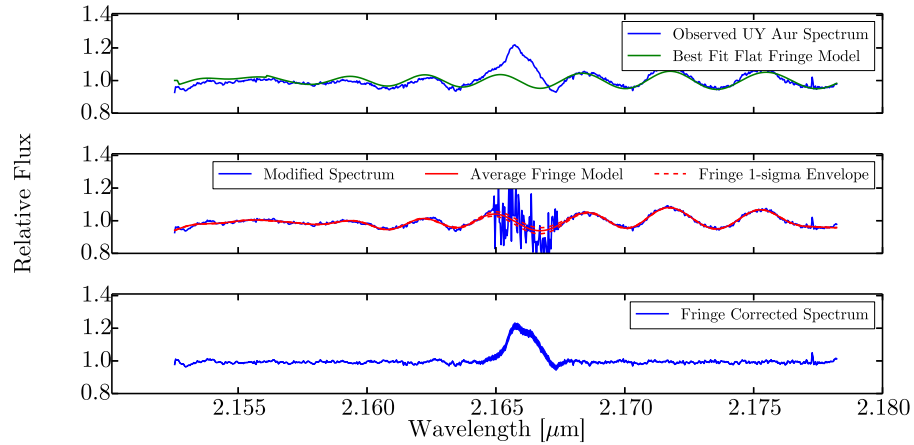


Figure 2.5: Top: Fit of the 1-d flat-field fringe to the observed spectrum. Middle: Regions of known broad-emission features are replaced with the best fit flat fringe and noise. This is repeated 1000 times, generating a model fringe with a Fourier filter each time. Bottom: The defringed spectrum, the width of the swath indicating the range of allowed solutions given the precision of our defringing model

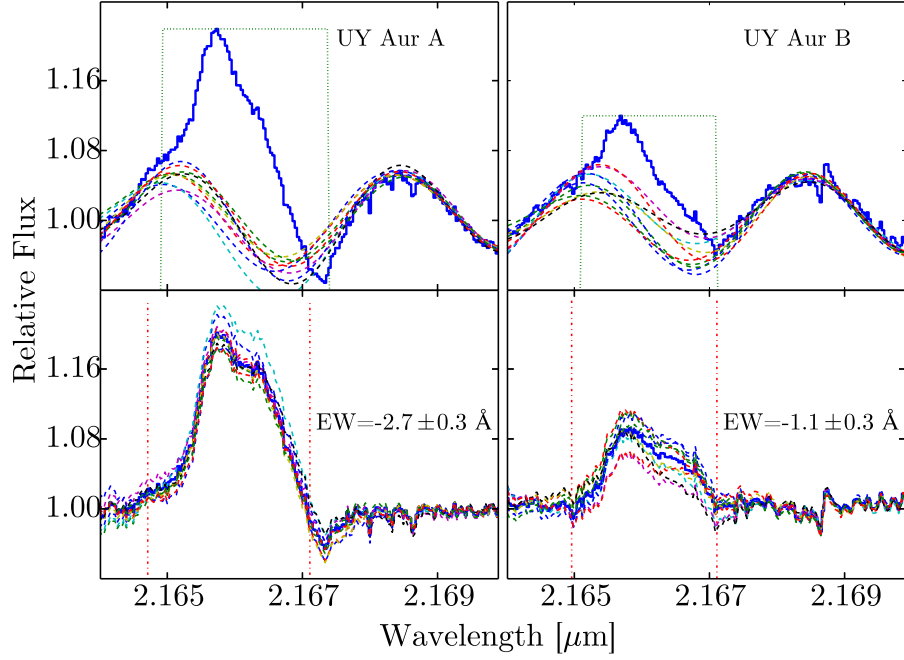


Figure 2.6: Measuring the EW of Br γ . The left column corresponds to UY Aur A, and the right column corresponds to UY Aur B. In the top panels, we show with a blue histogram the observed spectrum in the vicinity of Br γ . The dotted top hat indicates the portion of the observed spectrum which we excised and replaced with a noisy first-guess fringe. The smooth dashed fringes show 10 examples of the 1000 model fringes derived using this method. In the bottom panels we show the defringed spectrum for each of the 10 models to illustrate the range of our defringing confidence. This approach introduces ~ 0.3 Å error into our EW measurement.

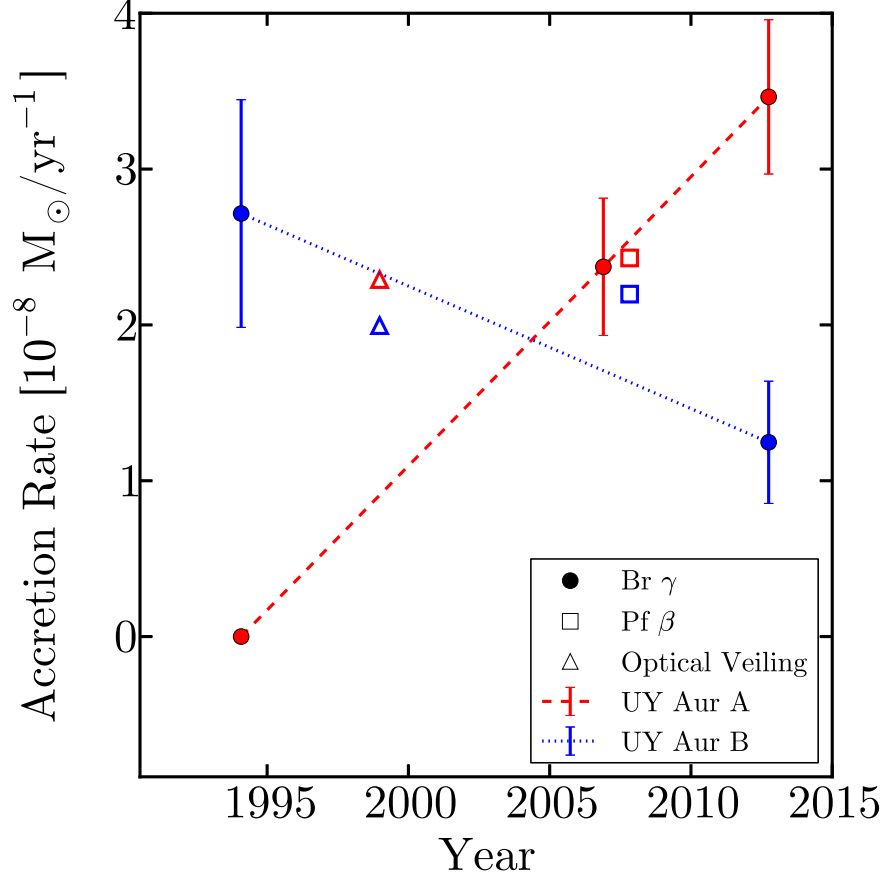


Figure 2.7: The mass accretion rate versus time for each component of the binary. Red symbols correspond to UY Aur A, and blue symbols correspond to UY Aur B. The filled circles, which have been connected by either a dashed (for UY Aur A) or dotted (for UY Aur B) line, represent measurements made using Br γ emission not corrected for extinction (Br γ data are from Herbst et al. (1995), Fischer et al. (2011), and this work). Errorbars include contributions from uncertainty in the continuum flux and in the EW. The open triangles show the accretion rate derived via a measurement of the optical veiling and are from Hartigan and Kenyon (2003). The open squares show the accretion rate measured using Pf β emission and are modified from Salyk et al. (2013) (see text). Since large systematic error ($\gtrsim 1$ dex) exists when comparing accretion rates from different indicators, we have not connected the open symbols to the line connecting the Br γ derived points.

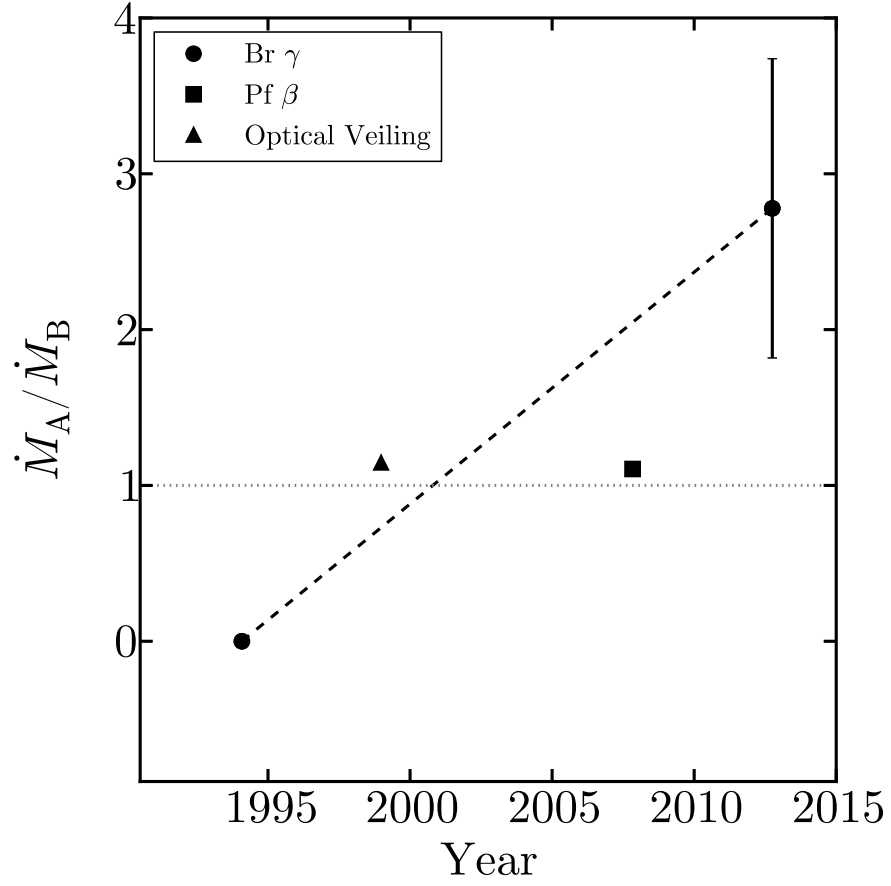


Figure 2.8: The relative accretion rate, \dot{M}_A/\dot{M}_B , for each epoch where the rate was measured for both sources. Accretion rate indicators are not corrected for extinction, which can be variable. The accretion rate ratios derived using Br γ luminosity have been connected by a dashed line. A dotted line indicates a ratio of unity. UY Aur A now appears to be accreting at a faster rate than UY Aur B.

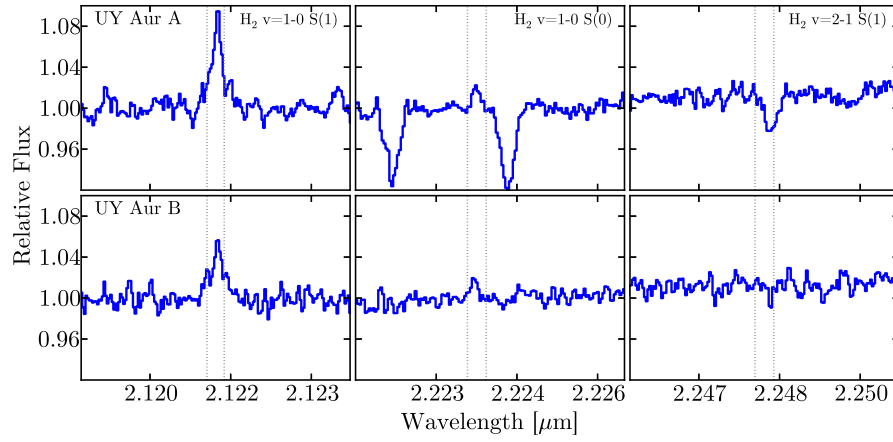


Figure 2.9: Molecular Hydrogen lines in the spectra of both UY Aur A (top), and UY Aur B (bottom). The $v=1-0$ S(1) and S(0) lines are detected in both sources, while the $v=2-1$ S(1) line is detected in neither. However, a photospheric absorption line in the spectrum of UY Aur A appears in the spectrum near where we would expect the $v=2-1$ S(1) line. We note that each order was independently normalized to make this figure.

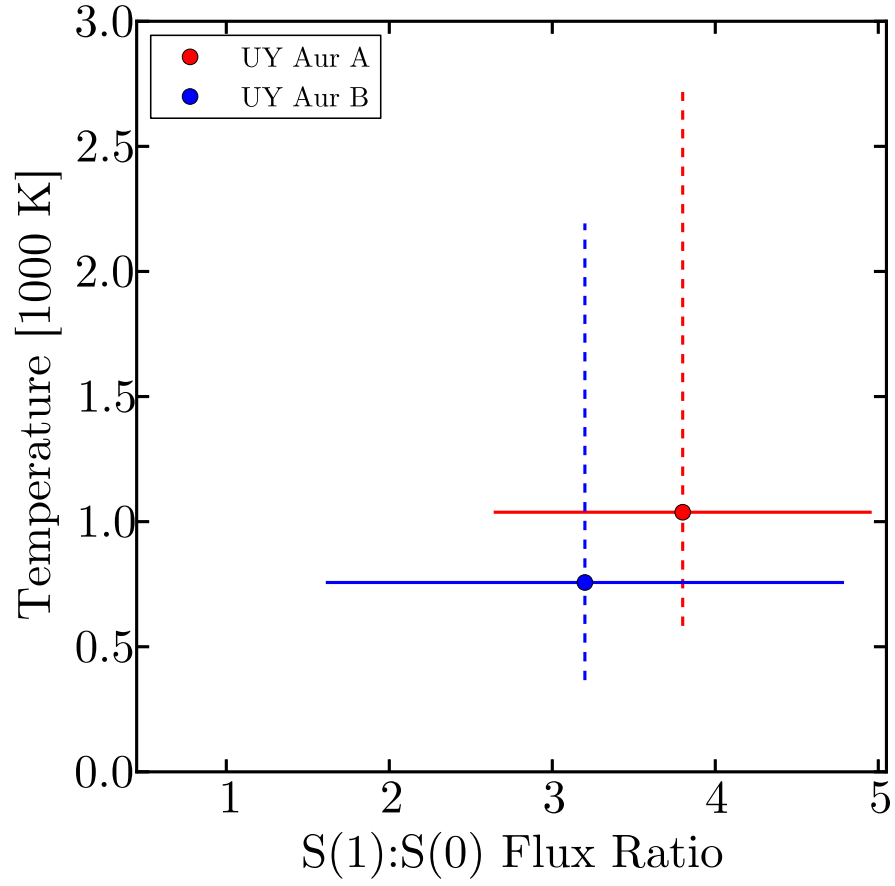


Figure 2.10: The molecular gas temperature deduced from the H₂ line ratios for each source, using an LTE model. The symbol for each source indicates the measured ratio and deduced temperature. The horizontal error bars indicate the range of ratios allowed given our uncertainty in the EW ratio of the lines. The vertical errorbars indicate the corresponding range of temperatures.

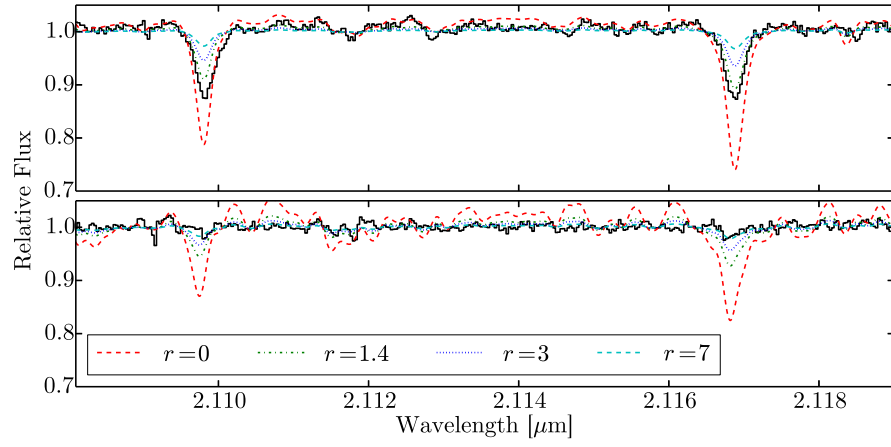


Figure 2.11: Top: A region of the observed spectrum of UY Aur A showing two Aluminum photospheric absorption lines (black histogram). We overplot a PHOENIX model photosphere ($T_{\text{eff}}=3900\text{K}$, $\log g=4.5$) veiled by $r = 0$ (dashed, red), 1.4 (dot dashed, green), 3 (dotted, blue), and 7 (dashed, cyan). The $r = 1.4$ value was reported by Fischer et al. (2011) for UY Aur A, and closely matches our observations. Bottom: UY Aur B observed spectrum and veiled synthetic spectra ($T_{\text{eff}}=3900\text{K}$, $\log g=4.5$). Photospheric lines in the spectrum are nearly absent, a significant change from the observations reported by Herbst et al. (1995).

CHAPTER 3

L-band Spectroscopy with Magellan-AO/Clio2: First Results on Young Low-Mass Companions[†]

L-band spectroscopy is a powerful probe of cool low-gravity atmospheres: The P, Q, and R branch fundamental transitions of methane near $3.3\ \mu\text{m}$ provide a sensitive probe of carbon chemistry; cloud thickness modifies the spectral slope across the band; and H_3^+ opacity can be used to detect aurorae. Here we describe commissioning the L-band spectroscopic mode of Clio2, the $1\text{--}5\ \mu\text{m}$ instrument behind the Magellan adaptive-optics system. We use this system to measure L-band spectra of young directly imaged gas-giant companions around nearby stars. Better constraints on the composition of extrasolar planet atmospheres could help in identifying their formation mechanism. Our spectra are generally consistent with the parameters derived from previous near-infrared spectra for these late M to early L type objects. The L-band spectrum of CD-35 2722 B is redder than field dwarfs with similar spectral type, suggestive of some dust settling. An increase in flux from $2.9\text{--}3.4\ \mu\text{m}$ in the spectrum of AB Pic b may be the result of methane opacity.

[†]This chapter is based on a manuscript in preparation by Jordan M. Stone, J. A. Eisner, A. Skemer, L. Close, K. Morzinski, J. Males, T. Rodigas, and P. Hinz. My roles included writing the necessary telescope proposal, planning the observations, designing the calibration strategy, executing the observations, developing the necessary computer software to perform calibrations, quantitative analysis of the results and writing the paper. I benefited from helpful conversations with the Co-authors, especially Josh Eisner and Andy Skemer. Other co-authors played a significant role in the development and implementation of the instrument.

3.1 Introduction

Low-gravity atmospheres, like those of young gas-giant planets, display distinct characteristics compared to their higher-gravity counterparts, even at the same effective temperatures (Marois et al., 2008; Bowler et al., 2010; Currie et al., 2011; Barman et al., 2011b; Skemer et al., 2012; Marley et al., 2012). Both cloudiness and dis-equilibrium chemistry are maintained as a result of the lower pressure: clouds because the photosphere is beneath the temperature-pressure location where refractory elements begin to condense to liquid and solid phases; and dis-equilibrium chemistry because the longer chemical timescales implied by the low pressure (and density) cannot keep up with vertical mixing timescales that deliver warm material from deeper layers (e.g., Hubeny and Burrows, 2007; Barman et al., 2011a; Marley et al., 2012).

As demonstrated in the cases of 2M 1207 b (Chauvin et al., 2004) and HR 8799 b, c, and d (Marois et al., 2008), dis-equilibrium chemistry, vertical mixing, and cloudiness are important factors in understanding the observed features of cool low-gravity atmospheres (Skemer et al., 2011; Barman et al., 2011b,a). Clouds and dis-equilibrium CH_4/CO chemistry have a large effect on L-band spectra because the P-, Q-, and R-branch methane bandheads trace the abundance of CH_4 , and cloudiness affects the general slope of the spectrum (Skemer et al., 2014). L-band measurements, augmenting near-IR spectra (throughout this work we will refer to Y, J, H, and K bands as near-IR, longer wavebands such as L and M-band we refer to as mid-IR), can also help to break degeneracies (e.g., between metallicity and gravity) when performing fits to model atmospheres (Skemer et al., submitted).

Atmospheric properties are crucial for understanding the nature and origin of directly imaged companions. The HR 8799 system contains four directly imaged companions with a non-hierarchical orbital architecture that closely resembles a planetary system, albeit much more massive than typical (Marois et al., 2008, 2010). Yet with uncertain companion masses ($\sim 10 M_{\text{Jup}}$) it is possible (though unlikely) that at least some of the companions exceed the $\sim 12 M_{\text{Jup}}$ minimum mass for deuterium burning (the maximum mass for an extrasolar planet according to the current IAU

definition). PSO J318.5-22, a $\sim 6 M_{\text{Jup}}$ isolated member of the β Pic moving group, occupies the same locus of color-magnitude space as HR 8799 b, c, d, e, and 2M 1207 b, but this object is not a planet because it was likely born in isolation (Liu et al., 2013).

PSO J318.5-22 and other low-mass brown dwarfs in the field appear to form through an extension of the star-formation process to very low masses (Luhman, 2012). Similarly, 2M 1207 b likely formed as an extension of the binary-star formation process (Lodato et al., 2005). The orbital architecture of the HR 8799 system suggests a distinct formation mechanism, such as core-accretion or gravitational-instability in a circum-stellar disk. Thus it appears nature is capable of producing fundamentally different objects, with distinct formation processes, that nevertheless have overlapping “planetary mass” masses.

Spectroscopy constrains the formation mechanisms of directly imaged companions by revealing their composition. If companion atmospheres gain a significant fraction of their mass via the accretion of solids in a disk, then they should show increased metallicity. The core-accretion process for gas-giant planet formation can produce metal enhanced planetary atmospheres compared to the host star (Pollack et al., 1996). Gravitational fragmentation of a massive protoplanetary disk can also result in a metal enriched atmosphere, as long as the fragment remains with a low mass ratio (Boss, 1997; Boley et al., 2011). Furthermore, because of the radial temperature gradient in protoplanetary disks, certain chemical species will be removed from the gas phase at radii corresponding to their freeze-out temperatures. This will result in distinct elemental ratios in the planetary atmosphere which may be diagnostic of the radial position at which a given planet formed in a disk (e.g., Öberg et al., 2011). On the other hand, if a companion is produced via gravitational fragmentation of the initial dense molecular cloud core, no large compositional differences are expected.

The Magellan adaptive-optics system (MagAO; Close et al., 2013), with its adaptive secondary mirror, is capable of providing low-background L-band images at the diffraction limit of the 6.5 m Magellan Clay telescope (providing a point-spread function with a width of 121 milliarcseconds). The mid-infrared camera, Clio2 (like Clio,

Sivanandam et al., 2006; Hinz et al., 2010, but with an upgraded HAWAII-1 array), that operates behind the MagAO system is equipped with a prism that can provide increasing spectral resolution from $R \sim 50\text{--}300$ across the L-band. Given the sensitive high-spatial resolution capabilities of MagAO, Clio2 spectroscopy is a powerful tool for providing the L-band spectroscopic constraints necessary for a complete understanding of directly imaged low-mass companion atmospheres. MagAO/Clio2 is an important complement to ongoing near-IR surveys for the detection and spectral characterization of new companions, such as the Gemini Planet Imager Exoplanet Survey (Macintosh et al., 2015), which are not sensitive in the L-band.

In this paper, we establish the L-band spectroscopic mode of MagAO/Clio2 and report first results on low-mass directly imaged companions. In Section 3.2 we describe our sample of targets and summarize near-IR constraints on the nature of their atmospheres. We also describe our data collection and reduction approach for the new mode. In Section 4.5 we summarize our L-band spectroscopic results for the sample. Finally, in Section 3.4 we discuss the implications of our findings.

3.2 Observations and Reduction

Data for this work were collected during two observing runs in 2014. The first was from 2014 April 5–6, and the second was from 2014 November 13–15. A summary of our observing logs is presented in Table 3.1. Our data collection and calibration approach is described below.

3.2.1 Target Selection and Parameters from Literature

Our target list, summarized in Table 3.2, was selected to include nearby young stars with low-mass companions visible from Las Campanas Observatory (declination $\lesssim 20^\circ$). Given the sensitivity of the MagAO wavefront sensor and of Clio2, we also selected targets to have guidestar I-band magnitudes $\lesssim 13$ and companion L-band magnitudes $\lesssim 14$ to facilitate obtaining adequate signal to noise in less than one night of observing. We focused on targets with well characterized near-IR spectra for direct

Table 3.1. Observing log

Target	Date	Plate Scale [mas/pix]	Tot. Int. [s]	R ^a	guidestar mag ^b	Comments
CD-35 2722 B	2014-04-07	15.9	280	50–200	$m_I = 9$	
TWA 5 B	2014-04-07	15.9	2240	50–200	$m_I = 9.1$	
HD 138575	2014-04-07	15.9	840	50–200	$m_V = 7$	A0V telluric calibrator
HD 32007	2014-11-14	25.7	540	150–300	$m_V = 8.5$	B9 telluric calibrator
AB Pic b	2014-11-14	25.7	3690	150–300	$m_R = 9$	
η Tel B	2014-11-15	25.7	720	150–300	$m_R = 5$	
2M 0103(AB) b	2014-11-15	25.7	1080	150–300	$m_I = 12.9$	guidestar is $\sim 0.2''$ binary
HD 10553	2014-11-15	25.7	360	150–300	$m_V = 6.6$	A3V telluric calibrator

^aThe prism provides increasing spectral resolution with wavelength across the L-band. The realized resolution is a function of the AO-performance when the PSF is smaller than the slit.

^bFor our companion sources we used the primary stars as the AO-guidestar. The wavefront sensor uses a non-standard filter covering the R and I bands.

comparison to our results. One of our targets, 2MASS J01033563-5515561(AB)b (hereafter 2M 0103(AB) b), which orbits a $0.2''$ M6-M6 binary-star system, does not have near-IR spectra available in the literature. We added this target to bolster our low-mass sample and to test the performance of MagAO while guiding on a close nearly equal-magnitude binary.

3.2.2 Instrumental Setup

The MagAO system is built around a 585 actuator adaptive secondary mirror that minimizes the number of optical elements necessary for correcting the blurring effects of Earth’s atmosphere. Compared to alternative implementations that position an adaptive element at a re-imaged pupil plane, adaptive-secondary systems provide higher throughput and lower thermal background (Lloyd-Hart, 2000). The system provides correction for up to 300 modes at up to 989 Hz. The pyramid wavefront sensor used by MagAO facilitates easy adjustments both in the number of modes corrected and the loop speed to help keep the AO-loop locked on faint guidestars or

Table 3.2. Summary of target information from the literature

Name	Dist. [pc]	Sep. [']	Sp. type	NIR template fit ^a			Assoc.	Est. Mass [M_{Jup}]	Est. Age [Myr]	references
				T_{eff} [K]	$\log(g)$ [cm s^{-2}]					
η Tel B	48	4.2	M8.5 \pm 0.5	2600 \pm 100	4 \pm 0.5	β Pic		\sim 30	\sim 12	12–14
TWA 5 B	50	2	M8.5 \pm 0.5	2500 \pm 100	4 \pm 0.5	TW Hya		\sim 20	\sim 10	8–11
CD-35 2722 B	21	3.1	L4	1700–1900	4.5 \pm 0.5	AB Dor		\sim 13	\sim 50	2,3
AB Pic b	46	5.5	L0 \pm 1	1800 $^{+100}_{-200}$	4.5 \pm 0.5	Tuc-Hor		\sim 12	\sim 30	4–7
2M 0103(AB) b	47	1.7	L	—	—	Tuc-Hor		\sim 13	\sim 30	1,7

^aThe near-IR spectrum of CD-35 27722 B was fit with an AMES-Dusty model atmosphere. For all the other sources best fit parameters from the BT-Settl 2012 grid are reported

References. — (1) Delorme et al. (2013); (2) Wahhaj et al. (2011); (3) Zuckerman et al. (2004); (4) Chauvin et al. (2005); (5) Bonnefoy et al. (2014); (6) Bonnefoy et al. (2010); (7) Torres et al. (2000); (8) Lowrance et al. (1999); (9) Neuhäuser et al. (2000); (10) Weinberger et al. (2013); (11) Webb et al. (1999); (12) Lowrance et al. (2000); (13) Neuhäuser et al. (2011); (14) Zuckerman et al. (2001)

in periods of poor seeing.

The prism in Clio2 provides increasing spectral resolution with wavelength. At J band the typical resolution is $R \sim 8$ and at M band it is $R \sim 500$. We used a 260 milliarcsecond slit to minimize the bright mid-infrared sky emission in our spectra. For observations with the PSF smaller than the slit, the size of the PSF is the relevant parameter for determining the spectral resolution (not the slit width). Thus, our observed spectral resolution changes with AO performance and wavelength. During the two runs reported here, we realized $R=50-200$ and $R=150-300$ across the L-band.

Due to the very different dispersions in the near- and mid-IR, there are different timescales for detector saturation in each band. In order to reduce practical complications related to saturation and cross-talk on the Clio2 detector, we observed through a blocking filter that only passes light from $\sim 2.8\mu\text{m} - \sim 4.2\mu\text{m}$.

Two camera lenses provide Clio2 with two plate scales, a coarse mode with 27.5 milliarcseconds pixel^{-1} , and a fine mode with 15.9 milliarcseconds pixel^{-1} . As part of our effort to define best practices for the use of the MagAO/Clio2 spectroscopy mode, we used a different plate scale for each of our runs. This also accommodated the observation of wider binaries. The optics used to set the plate scale also modify the position of the spectral trace on the Clio2 detector. The fine mode situates the trace on the left side of the detector, and the coarse mode positions the trace on the right side, which has more high dark current pixels and produces noisier spectra as a result.

3.2.3 Data Acquisition

We used the fine plate scale and observed both TWA 5 and CD-35 2722 during our first run. For our second run, we used the coarse plate scale and observed η Tel B, AB Pic b, and 2M 0103(AB) b. We saved frames differently for each run, saving single images per nod position during the first run and multiple images per nod during the second run. This difference slightly changes our reduction procedure for each dataset, as discussed below.

For each object, we aligned the binary position angle of our targets to be parallel

to the Clio2 slit so that we could collect spectra of both primary and companion sources simultaneously. This orientation allows us to use the primary star as a telluric calibrator for the companion. Because the slit position and angle are not repeatable, and because Clio2 does not have a slit viewer, we developed the following alignment procedure.

First, after acquiring our targets with the slit and prism out of the beam, we noted the position of the primary star and the position angle of the companion. Next, we introduced the slit and nudged the telescope horizontally until the primary star could be seen in the center. We then measured the angle of the slit on the detector and calculated the necessary slit rotation offset to align the target PA with the slit. The calculated rotation offset was implemented in small steps, $\lesssim 5^\circ$, without opening the AO loop. By keeping the AO-loop closed on the primary star while we offset the rotator to align our targets, we ensured that the star remained on the rotation axis, stationary in the slit.

Once both objects were aligned in the slit, we introduced the prism. In order to track variable background sky emission, we nodded our targets every 1–3 mins. When we could, we nodded along the slit so that we were always integrating on the target. At some rotation angles, when the entire weight of the wavefront sensor apparatus rested on just one motor, we had to nod off the slit because the motors were insufficiently powered to provide the desired nod vector. Currently both the previous weaker 1.6 Amp motors have been replaced by 3.0 Amp motors to hold the full weight.

On 2014 November 15, we observed η Tel during twilight because the source was setting. Since the sky was bright in the optical, we were unable to perform the normal telescope collimation steps. We ran the AO-loop closed with only 10-modes for five minutes in order to offload as much focus to the telescope as possible, and then increased the number of modes to begin observing. Twilight background light on the wavefront sensor still limited the accuracy of AO corrections and poor AO-performance was realized for this source.

3.2.4 Preliminary Reduction

Our data reduction process began by subtracting nod pairs. For the data from April this was simply an A-B and a B-A subtraction, where A and B represent our two nod positions. For the data from November, when we saved 6 images per nod position, we did $A_i - \text{median}(B)$ and $B_i - \text{median}(A)$, $i=1-6$. We then rotated each image to produce horizontal spectral traces. For the November data, we also applied a vertical shift to align each of the 6 images per nod, and co-added them. Typical rotations were $\sim 1.3^\circ$ and typical vertical offsets were $\lesssim 0.1$ pixels.

We created a master spectral trace for each object by combining the traces from each nod sequence. For our April observations we combined the traces using a simple mean. For our November observations, since we saved multiple images per nod position, we were able to measure the image variance in each pixel in each nod, so we derived a weight-image for each nod inversely proportional to the image variance before combining. For all of our sources we also bootstrapped the stacking procedure to produce stacks with randomly selected individual frames. This provides a variance image for use in determining optimal weights for spectral extraction (see below), and the raw data for bootstrapping the extraction, wavelength calibration, and telluric correction steps necessary for generating errorbars for our spectra.

For close companions, spectra may be contaminated by the wings of the primary if the primary flux at the position of the companion is larger than the background noise. TWA 5 B and 2M 0103(AB) b are the closest in our sample, requiring attention to this effect. To remove the light of the primary from the spectrum of the secondary, we created a model of the primary star trace using a high signal-to-noise image of a telluric calibrator spectrum observed just after observing the target. We rotated and shifted the telluric trace to overlap the trace of the primary. We then scaled each column of the telluric image so that the pixels in the core and first Airy ring best-fit the corresponding pixels in the image of the primary. This provided us with a model of the trace of the primary without the secondary. We smoothed this model with a circular gaussian kernel with $\sigma = 4$ pixels, and then subtracted it from the image before extracting the companion spectrum.

For the 2M 0103 system, we achieved much lower signal-to-noise than for TWA 5. Therefore our model trace was also noisy. Since the magnitude of the correction for 2M 0103(AB) b was much smaller than the noise, we decided not to subtract a noisy model from the images before extraction.

3.2.5 Spectral Extraction

We used the wavelength dependent spatial profiles of primary stars and our bootstrap generated variance maps to define optimal weights (Horne, 1986) for extraction. We found that including the first Airy ring in the spatial profile was important to avoid fringing in our spectra because spectral traces exhibit a fringe pattern where the core and Airy rings oscillate out of phase. For 2M 0103(AB) b, the circumbinary source, the primary spatial profile was corrupted by light from the nearby secondary. In this case we used the spatial profile of the telluric calibrator star observed shortly after we observed the target.

3.2.6 Wavelength Calibration

We derived our wavelength calibration based on the location of telluric absorption features in our spectra. First, we verified that the wavelength solution does not change—modulo horizontal offsets based on the variable slit position—with position on the detector. Then, for each night, we shifted and stacked all the telluric calibrator spectra using an inverse variance weighted mean to create a high signal-to-noise template spectrum of the telluric absorption.

To identify telluric absorption features in our stacked telluric spectra, we used a high-resolution ATRAN (Lord, 1992) synthetic transmission spectrum tuned for Cerro Pachon and made available by the Gemini Observatory¹. To make a proper comparison we first smoothed the template atmospheric spectrum to match the increasing spectral resolution in our data. We fit for the realized resolution each night, using a model that linearly increased in resolution over 20 steps from 2.93 μm to

¹<http://www.gemini.edu/sciops/telescopes-and-sites/observing-condition-constraints/ir-transmission-spectra>

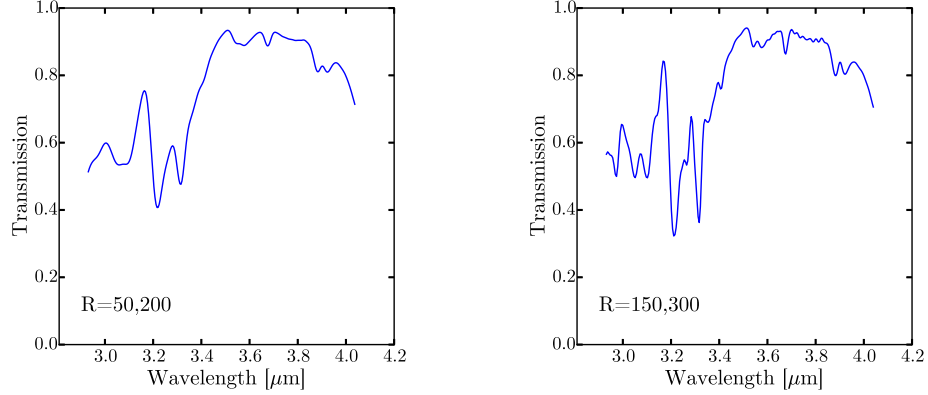


Figure 3.1: Smoothed ATRAN synthetic transmission spectra, demonstrating our spectral resolution during each run. The left side corresponds to our April run, and the right side corresponds to our November run.

4.04 μm . The best fit for 2014 April 7 was $R=50\text{--}200$. The best fit for both 2014 November 14 and 15 was $R=150\text{--}300$. We show the best fit models for each run in Figure 3.1. After compiling a set of pixel positions and reference wavelengths using our stacked template spectrum and our smoothed synthetic spectrum, we found the best fit second-order polynomial to convert pixel position to wavelength. The functional forms of the wavelength solutions for each run, modulo any horizontal pixel offsets, are

$$\lambda(x) = (-2.503 \times 10^{-6})x^2 + (0.004801)x + 2.822, \quad (3.1)$$

for our April run, and

$$\lambda(x) = (-3.634 \times 10^{-6})x^2 + (0.00548)x + 2.786, \quad (3.2)$$

for our November run. We wavelength calibrated the science target spectra by fitting for the best horizontal offset between target and calibrator, using a cubic interpolation scheme to perform the shift.

Two of our targets, CD-35 2722 B, and 2M 0103(AB) b, did not have high enough signal-to-noise to provide an adequate fit for the best horizontal offset. For these sources, we calculated the appropriate horizontal offset using the measured rotation angle of the slit and the separation from the primary. We verified using our other targets that this approach yields the correct offset to within 1–2 pixels.

3.2.7 Telluric Calibration

Our telluric calibration strategy used primaries to correct companions, and A-stars to correct primaries. We started by correcting primaries. We divided by the A-star spectrum obtained closest in time to a target spectrum and then multiplied by λ^{-4} to correct for the intrinsic black-body shape of the hot calibrator. Since most primaries have a more complicated intrinsic spectrum, before correcting companion spectra we fit for the best synthetic atmosphere spectrum from the grids of BT-Settl atmospheres (solar metallicity models from both the 2012 and 2015 grids were used; Allard et al., 2012; Baraffe et al., 2015). We smoothed the synthetic spectra using the same linearly increasing resolution parameters that we derived during our wavelength calibration process. We calibrated companions by dividing by primary spectra and then multiplying by the best-fit model for the primary. In two cases, η Tel (primary spectral type A0V; Torres et al., 2006) and CD-35 2722 (primary spectral type M1V; Torres et al., 2006), we did not obtain an adequate telluric calibrator spectrum. In these cases we used spectral types from the literature to select the appropriate model for the intrinsic shape of the primary spectrum, using the spectral-type- T_{eff} relationship of Pecaut and Mamajek (2013).

3.3 Results

3.3.1 Model Atmosphere Fits

Our reduced spectra are shown in Figure 3.2. For each object we determined the best fit model atmosphere from the latest BT-Settl grid (Baraffe et al., 2015). Many of our companions have had BT-Settl 2012 models (Allard et al., 2012) fit to their near-IR spectra, so we also fit to that grid to facilitate a direct comparison. We restricted ourselves to models with solar metallicity and with surface gravity between $\log(g)=3.0$ and $\log(g)=5.0$. Figure 3.3 illustrates why we chose the range of gravities that we did. At ages greater than 1 Myr, even $2 M_{\text{Jup}}$ objects should have surface gravity greater than $\log(g)=3.0$. Likewise, even 100 Myr old brown dwarfs at $80 M_{\text{Jup}}$ should have surface gravity less than $\log(g)=5.0$. These restrictions effectively serve

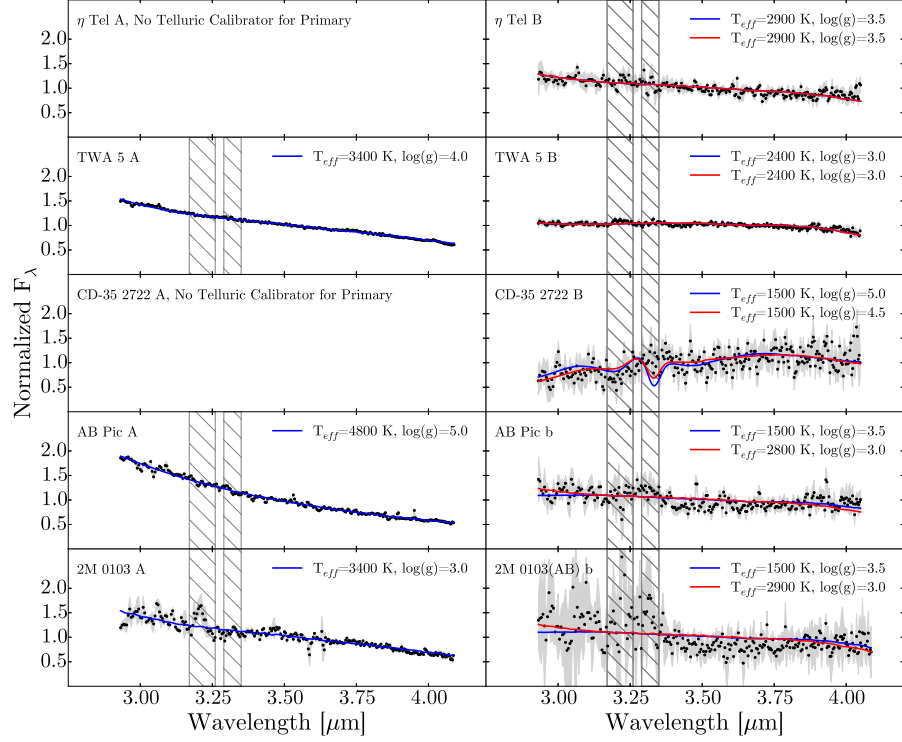


Figure 3.2: L-band spectra of young low-mass companions and their primary stars. Black points indicate measurements and the gray swath shows the $1 - \sigma$ confidence region derived via the bootstrap method and scaled up. Scale factors were determined for each run to provide $\chi_r^2 \sim 1$ for TWA 5 B, and η Tel B (see Section 3.3.1). We also show model atmosphere fits to our spectra. In blue, we show the best fit from the BT-Settl 2015 grid, and in red we show the best fit from the BT-Settl 2012 grid. For our primaries, there were no differences in appearance of best-fit models from either grid. Hatched regions near 3.2 and 3.3 μm indicate the location of strong telluric absorption features in our data. These regions were not considered during our model fitting. For two of our primaries, we did not collect appropriate telluric calibrator spectra, so we do not show their uncorrected spectra. We are still able to correct their secondaries because we assumed previously reported spectral types to determine their intrinsic spectral shape.

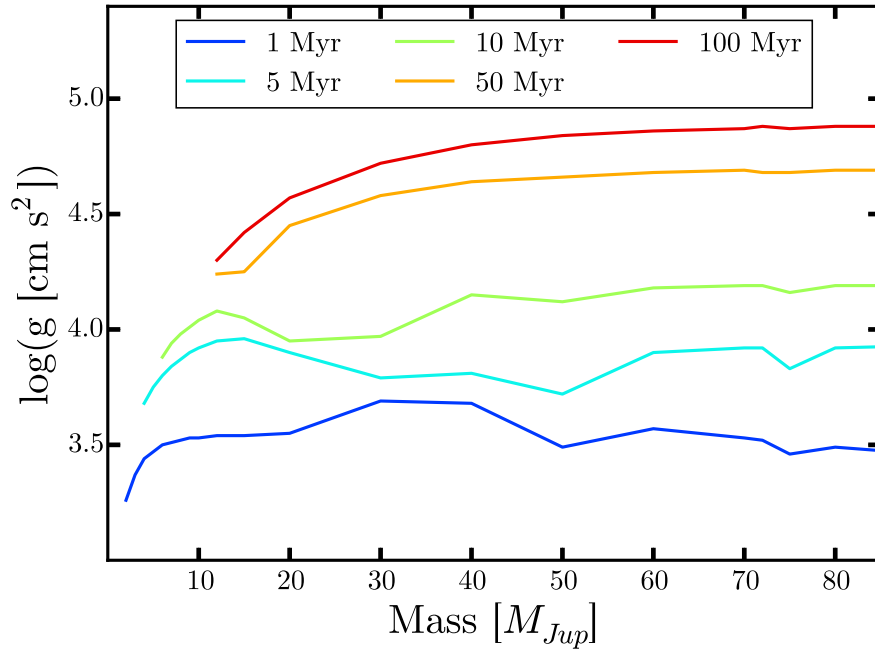


Figure 3.3: Predicted surface gravity as a function of mass from the BT-Settl 2015 models. Each curve represents a different snapshot in age, with the lowest surface gravities corresponding to 1 Myr, and the highest gravities corresponding to 100 My. Substellar objects with masses $\geq 2 M_{Jup}$ and ages older than 1 Myr should have $\log(g) > 3$. Likewise objects less massive than $80 M_{Jup}$ and younger than 100 Myr should have $\log(g) < 5$.

to fold in our prior knowledge on the age of our targets into the fitting process. After smoothing model spectra to the resolution of Clio2, fitting was done via χ^2 minimization using the inverse of our bootstrap errorbars as weights. Our fits ignored the spectral regions between 3.17–3.26 μm and 3.29–3.35 μm because these regions are affected by strong telluric absorption and are most susceptible to calibration errors. The best fits for each object are shown in Figure 3.2.

To identify the set of allowed model atmosphere parameters consistent with our measurements, we scaled up our bootstrap-derived errorbars for each source by a scale factor empirically determined for each run. We derived the correction factor by scaling the errorbars of our highest signal-to-noise spectra until the best-fit model atmosphere provided a reduced $\chi^2 \sim 1$. For the first run, we used TWA 5 B, and found a scale factor of 1.9. For the second run, we used η Tel, and we found a scale factor of 2.6. These scale factors are necessary to account for fixed-pattern noise—from flat field effects and bad pixels—that is not captured by our bootstrapping algorithm. The upgraded 3.0 Amp motors will provide greater access to more varied nod positions for future observations, allowing bootstrap algorithms to more effectively capture these errors.

Table 3.3 lists the best fit model parameters and uncertainty for each of the companions. The 1- σ uncertainties on each fit parameter were determined by finding all atmosphere models with scaled χ^2 values within 2.3 of the minimum and adding one grid-step. For example, if the best-fit model has $T_{\text{eff}}=2800$ K and a model with $T_{\text{eff}}=2700$ K is also allowed, then we report 2800^{+100}_{-200} K.

The 2015 and 2012 grids provide mostly similar fits to our spectra, and these fits reveal atmospheric parameters consistent with those deduced by fits to 1–2.5 μm spectra. Two of our sources, however, are fit by significantly different parameters when using the 2015 and 2012 grids. These sources are AB Pic b and 2M 0103(AB) b. Both exhibit a jump in the observed flux level near 3.4 μm that persists to the blue-end of the spectrum. This feature gives an overall blue shape to the spectrum and pushes the fit toward higher temperatures when using the 2012 grid. We discuss this peculiar feature in more depth in Section 3.4.

Table 3.3. BT-Settl Model Atmosphere Fits to L-band Spectra

Target	BT-Settl 2015		BT-Settl 2012		Fits to NIR spectra ^a	
	T_{eff}	$\log(g)$	T_{eff}	$\log(g)$	T_{eff}	$\log(g)$
η Tel B	2900^{+100}_{-200}	3.5 ± 0.5	2900^{+100}_{-200}	3.5 ± 0.5	2600 ± 100	4 ± 0.5
TWA 5 B	2400 ± 100	3.0 ± 0.5	2400 ± 100	3.0 ± 0.5	2500 ± 100	4 ± 0.5
CD-35 2722 B	1500 ± 100	5.0 ± 0.5	1500 ± 100	4.5 ± 0.5	$1700-1900$	4.5 ± 0.5
AB Pic b	1500 ± 100	3.5 ± 0.5	2800^{+200}_{-100}	3.0 ± 0.5	1800^{+100}_{-200}	4.5 ± 0.5
2M 0103(AB) b	1500 ± 100	3.5 ± 0.5	2900 ± 200	3.0 ± 1.0	—	—

^aSame as in Table 3.2, included here for convenience.

Some of our best fits have surface gravities at the edge of our restricted model grid: the 2015 and 2012 grid fits of TWA 5 B, the 2015 grid fit to CD-35 2722 B, and the 2012 grid fits to AB Pic b and 2M 0103(AB) b. As discussed above the 2012 grid fits to AB Pic b and 2M 0103(AB) b are inaccurate due to an increased flux feature seen in both spectra. The best fits for TWA 5 B from both grids for have $\log(g)=3$, a slightly bluer model than the $\log(g)=4$ version at the same effective temperature. The best fit model from the 2015 grid to CD-35 2722 B has $\log(g)=5$. The 3–4 μm spectrum of CD-35 2722 B is redder than field dwarfs with similar spectral type (see Section 3.3.2), thus our fit is pushed to the redder higher-gravity models.

3.3.2 Comparison to Field Dwarf Spectra

The L-band SEDs of directly imaged extrasolar planets appear distinct from the SEDs of older field dwarfs at the same effective temperatures (Skemer et al., 2014). The discrepancy needs better characterization to provide insight into the physical processes affecting their atmospheres. Comparison to model atmospheres can be helpful in identifying important spectral features, but models are challenged to capture the processes at play in cool atmospheres, particularly in providing accurate representation of clouds (e.g., Marley and Robinson, 2014). Here we compare our

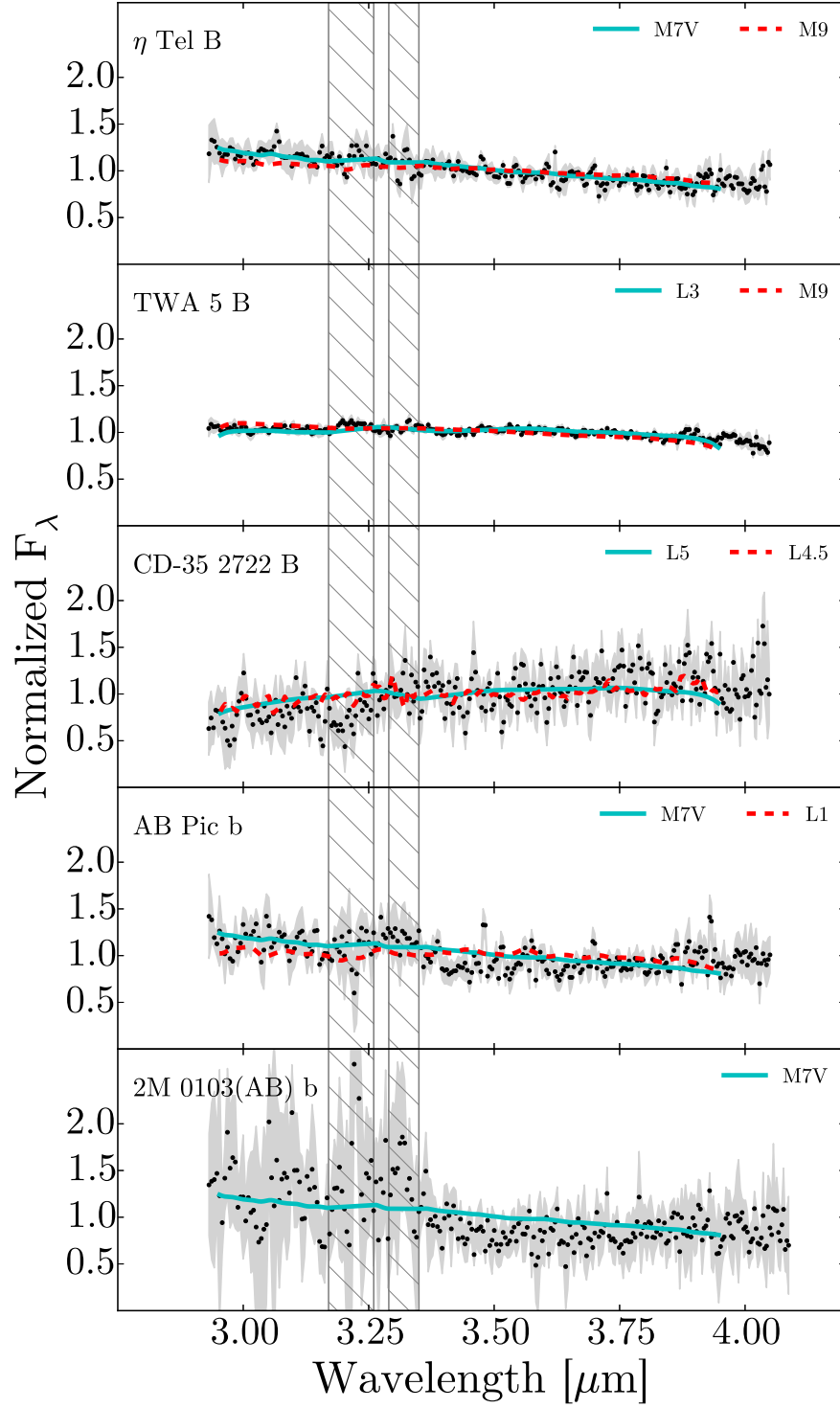


Figure 3.4: The same companion spectra as in Figure 3.2, now compared to empirical spectra of field dwarfs from Cushing et al. (2005). With a solid cyan line we show the best fit field dwarf spectrum. We show the spectrum corresponding to the optical/NIR spectral type of each of our targets (Table 3.2) with a red dashed line. The spectra for each spectral type correspond to the following targets: M7, GJ 644 C; M9, LP 944-20; L1, 2MASS J14392836+1929149; L3, 2MASS J15065441+1321060; L4.5, 2MASS J22244381-0158521; L5, 2MASS J15074769-1627386.

spectra of young directly imaged companions to the spectra of field dwarfs from the literature. We use the set of spectra, including spectral types M7 through T5, presented in Cushing et al. (2005). Figure 3.4 shows the best fitting field dwarf spectrum for each of our companion sources. We also overplot the field dwarf spectrum corresponding to the optical/NIR spectral type reported for each of our sources, except 2M 0103(AB) b, which does not have a NIR spectral type reported in the literature.

In general, the best-fit spectrum and the spectrum selected to match the optical/NIR spectral type are similar. Even though they often differ by a few spectral types, these generally provide an adequate match to our observations. Our data show that for late-M and early L type spectra, the L-band is not particularly diagnostic of spectral type. For example, the M9 and L3 type dwarf spectra both exhibit similar slopes and both track the spectrum of TWA 5 B. Previous authors have also noted that L-band spectra alone are not particularly powerful for deducing spectral types in this range (e.g., Cushing et al., 2008).

At later spectral types 3–4 μm spectra do exhibit distinct features compared to late M-dwarfs and early L-dwarfs because of increased methane opacity and decreased cloud opacity at cooler temperatures. The latest spectral type source in our sample, CD-35 2722 B, which is classified as L4 based on NIR spectra (Wahhaj et al., 2011), appears redder than the best fit L5 field dwarf spectrum, with most of our measurements below the dwarf spectrum at the blue end of the band, and most of our measurements above the dwarf spectrum at the red end. This example underscores the importance of L-band spectroscopy for objects with later spectral type than mid-L.

3.4 Discussion

3.4.1 Comparison to Directly Imaged Planets

Directly imaged extrasolar planets have L-band SEDs that are inconsistent with field brown dwarfs and the models that fit them. The low surface gravity prevalent in young planetary mass atmospheres is responsible for the presence of clouds and

dis-equilibrium chemistry at effective temperatures where more massive T-dwarfs appear cloud free and methane rich (Barman et al., 2011a; Skemer et al., 2012; Marley et al., 2012). Here we observe a warmer more-massive population of young companions. Most of our atmospheric fits are consistent with the fits found by previous authors using NIR spectra. The similarity of our L-band derived atmospheric parameters compared to near-IR results underscores the functionality of the MagAO/Clio2 spectroscopic mode and the general success of model atmospheres to capture the most important physics responsible for the appearance of spectra at these effective temperatures, where clouds are expected and CH_4 absorption is not.

Comparing our data to HR 8799 b, c, d and 2M 1207 b, we can constrain the discrepancy in L-band spectra to arise between ~ 1000 K, the best fit effective temperature for 2M 1207 b in Barman et al. (2011b), and ~ 1500 K, the best fit temperature for AB Pic b and 2M 0103(AB) B reported here. This range brackets the L-T transition for field brown dwarfs, emphasizing that the discrepancies in 3–4 μm spectra are related to the cloud clearing and chemical processes responsible for the evolution from L-dwarf to T-dwarf.

3.4.2 The Red Slope of CD-35 2722 B

CD-35 2722 B was classified as an L4 by Wahhaj et al. (2011) based on the similarity of its J, H, and K-band spectra to 2MASS J2224438-015852, an object whose very red color is distinct from other field dwarfs and implies large amounts of atmospheric dust (Cushing et al., 2005; Stephens et al., 2009). CD-35 2722 B has a bluer NIR color than 2MASS J2224438-015852 (Wahhaj et al., 2011), suggesting somewhat different cloud structure. Figure 3.4 shows that our L-band spectrum of CD-35 2722 B appears redder than the corresponding spectrum of 2MASS J2224438-015852. Cushing et al. (2008) vary the cloud sedimentation parameter for a model atmosphere with $T_{\text{eff}} = 1800$ and $\log(g)=5$ (similar to the atmospheric parameters of CD-35 2722 B deduced from NIR spectra by Wahhaj et al. (2011) and from L-band spectroscopy presented here) and show that a larger sedimentation parameter (resulting in less cloud opacity) results in a redder L-band spectrum because CH_4 absorption

is exposed. Thus the NIR colors and L-band spectral slope are consistent indicators that CD-35 2722 B exhibits somewhat less opaque clouds than 2MASS J2224438-01582. In Figure 3.4, we show our L-band spectrum of CD-35 2722 B and the spectrum of the L5-type 2MASS J15074769-1627386. CD-35 2722 B appears to be more red than the field dwarf. Thus, CD-35 2722 B may have less cloud opacity than some field dwarfs.

CD-35 2722 B is the oldest target in our young sample (~ 50 Myr, Zuckerman et al., 2004), and has the highest surface-gravity. If its red 3–4 μm spectral slope does indicate thinning clouds, our observations suggest some early atmospheric evolution including some cloud settling or dispersion on timescales $\lesssim 50$ Myr.

3.4.3 A Blue Feature in AB Pic b and 2M 0103(AB) b

The BT-Settl 2012 and 2015 grids provide significantly different best-fit effective temperatures for two of our sources: AB Pic b, and 2M 0103(AB) b. In each case, the best-fit temperature from one grid is outside the $3\text{-}\sigma$ estimate for the temperature in the other. This discrepancy highlights significantly different behavior of the 2015 grid for low-gravity atmospheres near 1500 K, compared to the 2012 grid. Both AB Pic b and 2M 0103(AB) b exhibit an increase in flux in the spectral region between $\sim 2.9\text{--}3.4$ μm . None of the atmospheric models predict such a feature and the high effective temperatures suggested by the BT-Settl 2012 fits are probably incorrect, caused by the average blue slope of the spectra due to the anomalous blue feature.

For 2M 0103(AB) b, the feature may be due to a combination of lower signal-to-noise and difficulties in observing and calibrating associated with orbiting a close binary (e.g., reduced AO performance). However, for AB Pic b, we achieved higher signal-to noise across the spectrum. The spectrum of AB Pic b was corrected for telluric emission using the spectrum of AB Pic A, which was positioned within the slit with AB Pic b and observed simultaneously; any atmospheric changes during the course of the observation should have been tracked perfectly by the primary. Furthermore, our model atmosphere fit for AB Pic A is exactly as expected for the

spectral type (K1V; Torres et al., 2006; Pecaut and Mamajek, 2013), suggesting we have properly calibrated AB Pic A and identified the correct model for its intrinsic spectral shape when correcting AB Pic b. Given the quality of the telluric correction of AB Pic A, we also checked whether correcting AB Pic b with the same A-star calibrator provided a different result. Regardless of whether HD 32007 or AB Pic A is used for telluric calibration, the increased flux short of $3.4 \mu\text{m}$ persists. We also verified that the feature is present in both A-nods and B-nods independently and in the first half of our integrations as well as in the second half.

If the increase in our spectrum is physical, the larger-than-expected flux in the spectral region corresponding to methane opacity could indicate an atmospheric inversion or possibly an aurora (e.g.; Hallinan et al., 2015). However, strong H_3^+ emission, often associated with aurorae (e.g., Brown et al., 2003), is not present at 3.5 and $3.7 \mu\text{m}$. Additional follow up observations of AB Pic b in the L-band are warranted to better understand the blue feature seen in our data.

Polycyclic aromatic hydrocarbon molecules (PAHs) are known to have broad emission bands centered at 3.3 and 3.4 microns. However, fluorescent PAHs in the vicinity of AB Pic b and 2M 0103(AB) b are unlikely given the system ages and the absence of strong UV-emitting sources.

3.5 Conclusions

We commissioned the L-band spectroscopic mode of Clio2 behind the MagAO system. We observed five young directly imaged companions orbiting nearby stars. The spectra of these companions are consistent with expectations based on fits to shorter wavelength data. This result constrains the temperature range where the L-band SEDs of young directly imaged planets begin to diverge from older field dwarfs to the range $1000 < T_{\text{eff}} \lesssim 1500$ K. This range brackets the onset of the L-T transition for field dwarfs, providing further evidence that observed discrepancies are due to clouds and non-equilibrium CO/CH₄ chemistry due to vertical mixing. The L-band spectrum of CD-35 2722 B is redder than field dwarfs and suggests some cloud settling in this ~ 50 Myr old object. We also see an increased flux feature from

2.95–3.4 μm in the spectra of 2M 0103(AB) b and AB Pic b. The feature coincides with significant methane opacity, and if physical, could indicate a thermal inversion. L-band spectroscopy with Clio2 will be an important complement to ongoing surveys for directly imaged extrasolar planets that are conducting their searches at shorter wavelengths.

This work was supported by NASA Origins grant NNX11AK57G and NSF AAG grant 121329. J.M.S. was also partially supported by the state of Arizona Technology Research Initiative Fund Imaging Fellowship. A.S. is supported by the National Aeronautics and Space Administration through Hubble Fellowship grant HSTHF2-51349 awarded by the Space Telescope Science Institute, which is operated by the Association of Universities for Research in Astronomy, Inc., for NASA, under contract NAS 5-26555. We thank M. Cushing for providing L-band spectra of field dwarfs.

CHAPTER 4

Disentangling Confused Stars at the Galactic Center with Long Baseline Infrared Interferometry[†]

We present simulations of Keck Interferometer ASTRA and VLTI GRAVITY observations of mock star fields in orbit within ~ 50 milliarcseconds of Sgr A*. Dual-field phase referencing techniques, as implemented on ASTRA and planned for GRAVITY, will provide the sensitivity to observe Sgr A* with long-baseline infrared interferometers. Our results show an improvement in the confusion noise limit over current astrometric surveys, opening a window to study stellar sources in the region. Since the Keck Interferometer has only a single baseline, the improvement in the confusion limit depends on source position angles. The GRAVITY instrument will yield a more compact and symmetric PSF, providing an improvement in confusion noise which will not depend as strongly on position angle. Our Keck results show the ability to characterize the star field as containing zero, few, or many bright stellar sources. We are also able to detect and track a source down to $m_K \sim 18$ through the least confused regions of our field of view at a precision of $\sim 200 \mu\text{as}$ along the baseline direction. This level of precision improves with source brightness. Our GRAVITY results show the potential to detect and track multiple sources in the field. GRAVITY will perform $\sim 10 \mu\text{as}$ astrometry on a $m_K = 16.3$ source and $\sim 200 \mu\text{as}$ astrometry on a $m_K = 18.8$ source in six hours of monitoring a crowded field. Monitoring the orbits of several stars will provide the ability to distinguish between multiple

[†]This chapter has been previously published as Stone et al. (2012). My roles included developing the necessary simulators, mock star fields, mock observing strategies, synthetic data, and data analysis tools. I performed the quantitative analysis and wrote the paper. I benefited from helpful conversations with Josh Eisner. Other co-authors are members of the Keck-Interferometer ASTRA team

post-Newtonian orbital effects, including those due to an extended mass distribution around Sgr A* and to low-order General Relativistic effects. ASTRA and GRAVITY both have the potential to detect and monitor sources very close to Sgr A*. Early characterizations of the field by ASTRA including the possibility of a precise source detection, could provide valuable information for future GRAVITY implementation and observation.

4.1 Introduction

Over the last 20 years, high resolution infrared imaging techniques have provided precise astrometric measurements of stellar sources at the Galactic Center. Focused astrometric monitoring campaigns have revealed a population of mostly young early-type stars (the S-cluster) in orbit about the location of the radio and infrared source dubbed Sagittarius A* (Sgr A*). In fact, Ghez et al. (2008) and Gillessen et al. (2009a) both analyze their own distinct data sets to deduce a mass of $4.5 \pm 0.4 \times 10^6 M_\odot$ located coincident with Sgr A*. This mass must all be within the periaapsis of the star S16/S0-16¹, which is only 40 AU. The implied mass density provides compelling proof that Sgr A* is the luminous manifestation of an accreting black hole. In addition to providing a measurement of the mass of Sgr A*, the orbits of the stars also provide a direct measurement of the distance to the black hole, 8.36 ± 0.44 kpc (Ghez et al., 2008).

If Sgr A* actually resides at the dynamic center of the Milky Way, then measuring its distance also represents a measurement of the solar distance from the Galactic Center (R_0). Monitoring stellar orbits about Sgr A* also provides a measurement of the sun's peculiar motion in the direction of the Galactic Center (Θ_0). As discussed by Olling and Merrifield (2000), R_0 and Θ_0 are ubiquitous parameters in the description of the structure and dynamics of the Milky Way (see also Reid et al., 2009). Uncertainty in the values of R_0 and Θ_0 are the largest sources of error in the determination of the ratio of the galactic halo's long and short axes (q , Olling

¹The UCLA and the MPE groups have adopted different naming conventions for the S-cluster

and Merrifield, 2000). The parameter q is sensitive to different galaxy formation scenarios and dark matter candidates, and if R_0 and Θ_0 were known at the 1% level, the constraints on q would help to differentiate theories of galaxy formation and dark matter (Olling and Merrifield, 2000). In addition, a very precise knowledge of R_0 could affect our calibration of the lowest rungs of the cosmic distance ladder by improving our distance measurements to galactic sources such as Cepheids and RR Lyrae variables (Ghez et al., 2008).

The existence of the S-cluster is intriguing because it is rich with young stars and because forming these stars in situ represents a theoretical problem given the strong tidal forces in the region. The alternative of formation at larger radii and subsequent migration is strongly constrained by the deduced young age of the stars. However, because the S-stars are known to be younger than the relaxation time in the environment (a B star's main-sequence lifetime is $\sim 10^7$ years compared to the relaxation time of $\sim 2 \times 10^8$ years; Weinberg et al., 2005) their orbits should encode some information about the kinematics of the cluster at the time it formed. Thus, perhaps as a bonus, astrometric monitoring of the stars in our Galaxy's nuclear cluster has the potential to inform the community not only on matters of General Relativity and galaxy formation, but also on star formation in extreme environments.

The deduced mass and distance of Sgr A* make it the largest black hole on the sky, in terms of angular diameter, and an excellent candidate for study. Improving astrometric measurements and discovering stars on even shorter period orbits will improve our understanding of the gravitational potential that binds the stars, possibly exposing a dark matter cusp at the center of our galaxy, and should inform our understanding of gravity on scales not yet explored by precise experiments. For example, Weinberg et al. (2005) modeled a distribution of stars on very short period orbits about Sgr A* and showed that post-Newtonian effects on the orbital paths could be detected with the astrometric precision and sensitivity of a future thirty-meter telescope. Existing and upcoming near-IR interferometers can provide even better resolution, and enable some of the same science. In their treatment Weinberg et al. (2005) assumed Gaussian point spread functions, which tend to zero in the

wings faster than the more realistic Airy pattern which distributes light in rings away from the central core. These rings present a contrast barrier in conventional imaging. Likewise, the even more complicated point spread functions (PSFs) provided by interferometers result in contrast and detection limits and can bias astrometric measurements.

Fritz et al. (2010) showed that halo noise and source confusion are the factors limiting astrometric accuracy. These effects, which are both related to the angular resolution of the telescope and the luminosity function of the sources in the region (i.e. the dynamic range), present a fundamental astrometric hurdle that cannot be overcome with even the largest single aperture telescopes of today (Ghez et al., 2008; Gillessen et al., 2009a). In fact, simulations by Ghez et al. (2008) and Gillessen et al. (2009a) showed that astrometric errors could be as large as 3 milliarcseconds due to confusion with undetected sources. This level of astrometric uncertainty, present close to Sgr A* where stars experience the deepest part of the potential, has precluded the detection of any post-Newtonian effects on stellar orbits to this point and has limited the precision with which the distance to the Galactic Center can be measured.

The limiting magnitude and astrometric precision of Galactic Center observations has improved as early speckle observations (e.g. Eckart et al., 1992) were supplemented by adaptive optics (AO) and laser guide star AO (e.g. Ghez et al., 2005). The current state of the art is a limiting magnitude of ~ 19 at K and an astrometric precision of $\sim 100 \mu\text{as}$. However, these limits are only achieved far from the crowded central region immediately surrounding Sgr A*. In this paper we investigate whether, with the increased resolution of infrared interferometers and the concomitant reduction in confusion, we can detect heretofore undetected or unnoticed stars on orbits with very short periods within 50 mas of Sgr A*. We also explore the astrometric precision with which such sources could be monitored with an IR interferometer. According to Ghez (2010) a factor of ~ 3 more stars with periods less than 20 yrs is expected to be orbiting Sgr A*. These stars, if they can be detected and monitored, will provide a detailed description of the central potential (a minimum of three

short-period orbits is required for a complete characterization; Rubilar and Eckart, 2001). Additionally, such stars will provide the best targets for observing General Relativistic effects since they are deepest in the potential well of Sgr A*.

Although the higher resolution provided by interferometry is beneficial for increasing the detectability of sources in the crowded region and for increasing the astrometric precision attainable, there are many potential complicating factors that do not apply to conventional full aperture imaging. For example, in full aperture imaging, collecting area increases as the square of the resolution. In interferometers, however, the collecting area is independent of the effective spatial resolution. This means that although the confusion limit is somewhat alleviated by the higher angular resolution available, photon noise quickly becomes a problem in the detection of faint sources. This fact is further exacerbated by the low typical throughput of interferometers (e.g., $\sim 2\%$ for the Keck Interferometer). Additionally, the sparse nature of an interferometer's collecting area results in an incomplete sampling of the Fourier components of the source distribution on the sky. This causes an incomplete knowledge of the sky-plane light distribution resulting in PSFs with large sidelobes. Finally, Michelson interferometers like the Keck Interferometer and the VLT Interferometer (VLTI) have small fields of view, ~ 50 mas, which typically only include a single object; clearly this presents difficulty for astrometry. We attempt to understand the scale of these effects by simulating data and inferring results.

The outline of the paper is as follows. In Section 2 we discuss the construction of mock star fields within 50 mas of the Galactic Center. In Section 3 we discuss our observation simulator and all included sources of noise and uncertainty. Section 4 covers our algorithm for making relative astrometric measurements by fitting to the visibility curves. Section 5 includes a presentation of our results. Section 6 provides a discussion of the potential advances and difficulties. Although we try to keep the discussion general, we focus on ASTRA at the Keck Interferometer as we are most familiar with that instrument and it is currently capable of making these observations. We also provide a discussion of VLTI GRAVITY (Eisenhauer et al., 2008) simulations.

4.2 Simulating a Star Field within 50 Milliarcseconds of Sgr A*

Interferometric observations of the Galactic Center will be conducted through the K band. We construct mock star fields in orbit about the black hole at the Galactic Center using as much information about the number of sources and the distribution of K band magnitudes as is available. Previous observations, while limited by confusion noise, have provided a wealth of information regarding the stellar population and K-band luminosity function (KLF) of the central cluster. Genzel et al. (2003) showed that the KLF of the inner 1.5'' around Sgr A* is well fit by a power law with a slope of $\beta = \frac{d \log N}{dK} = 0.21 \pm 0.03$. Weinberg et al. (2005), for example, used this luminosity function normalized to the photometry of Schödel et al. (2002) of the stars within 0.8'' of Sgr A* to extrapolate the population of stars even closer to the Galactic Center.

Additionally, some clues about the content of the confused region can be gleaned from observations of well-monitored stars—stars on orbits that spend most of their time outside of the confused region—when they pass through the confused region during their orbital periapsis. For example, when the star S0-2 passed through periapsis in 2002 its centroid was offset from its fitted orbital path. This offset strongly suggests a confusion event with an undetected source (or multiple undetected objects). By measuring the offset and the ellipticity, or lack thereof, of the S0-2 PSF during 2002, some constraints on the unseen source(s) can be derived (e.g. Gillessen et al., 2009a).

Further, both Do et al. (2009b) and Dodds-Eden et al. (2011) provide analyses of Sgr A* light curves and show a median magnitude in K-band of $\gtrsim 16$ and a minimum magnitude of $\gtrsim 17$. While absolute photometry in the region is complicated by confusion noise, we use the analyses of Sgr A* lightcurves to normalize two separate star fields for use in our study. In our first star field, Field1, we set the flux from Sgr A* equal to its median observed value, the flux from the brightest star in the field we set to be consistent with the minimum observed flux from the region as reported in Do et al. (2009b) and Dodds-Eden et al. (2011), and we include three fainter stellar

Table 4.1. Model star field parameters for our simulated fields.

Source	Field1 [m_K]	Field2 [m_K]	spectral slope	Period [yrs]	e	τ [yrs]	Ω [rad]	i [rad]	ω [rad]
Sgr A*	16.3	17.3	4.5	—	—	—	—	—	—
Star 1	16.9	17.9	2.28	1.75	0.44	0.93	5.32	0.68	4.19
Star 2	18.8	19.8	2.34	2.65	0.12	0.60	2.61	1.36	4.89
Star 3	20.3	21.3	2.31	0.24	0.90	0.20	4.64	-0.61	2.95
Star 4	20.6	21.6	2.14	2.31	0.74	1.53	1.16	1.07	0.91

Note. — We assumed random Keplerian orbits for our modeled sources. τ is the time of periapsis passage in years since January 1, Ω is the longitude of the ascending node, i is the inclination, and ω is the argument of periapsis.

sources consistent with an extrapolation of the KLF reported in Genzel et al. (2003) (see their Table 2). To be cautious, we also model a second star field in which we have decreased the flux of each source by one magnitude. This fainter star field we call Field2. We believe that these two fields should encompass a fair representation of the true source distribution very close to Sgr A*.

While we took care that our star fields are consistent with available observations, the true source content within 50 milliarcseconds is unknown. The potential to further constrain the stellar content within the region is one the scientific motivations for observing the Galactic Center with long-baseline infrared interferometers.

We assigned spectral slopes to our sources to be consistent with the observed slopes of sources near the Galactic Center, namely $\alpha = 2.3 \pm 0.1$ for $F_\lambda \propto \lambda^\alpha$. The spectral slope of Sgr A* was taken to be $\alpha = 4.5$ (Tuan Do, private communication; see also Do et al. (2009a) and Paumard et al. (2006)).

While we modeled Sgr A* as stationary, the stellar sources were assigned random Keplerian orbits with semi-major axes in the range of 0.1-400 AU. We chose this range of semi-major axes to coincide with the confused region around Sgr A*. Any source with a larger semi-major axis should leave this region, and would likely have been detected in previous AO observations. Table 4.1 shows the modeled parameters for our star fields.

4.3 Synthesizing Visibility Data

4.3.1 Basic Concepts

Interferometers combine light from a source collected at more than one aperture, forming an interference pattern. This interference pattern encodes high spatial frequency information of the light distribution under observation. The maximum spatial frequency which can be detected by an interferometer can be expressed succinctly as $\frac{B_{\text{proj}}}{\lambda}$, where λ is the wavelength of the observation and B_{proj} is defined as the projection of the vector connecting the two apertures onto the plane of the sky in the direction of observation. The interference pattern of light created by a monochromatic source can be described as

$$P(\delta) = P_1 + P_2 + 2\sqrt{P_1 P_2} \text{Re}\{V e^{ik\delta}\} \quad (4.1)$$

or

$$P(\delta) = P_1 + P_2 + 2\sqrt{P_1 P_2} |V| \cos(k(\arg(V) + \delta)) \quad (4.2)$$

where P_1 and P_2 are the incident power from each aperture, k is the wave number, δ is the relative path-length delay between the two apertures, and V is the complex visibility (see e.g. Lawson, 2000).

The polychromatic case is slightly more complicated, and a brief discussion of the effects of a finite bandwidth on interference fringes will help elucidate some of the challenges of practical interferometry. In general, astronomical sources radiate polychromatic light such that each wavelength of light is mutually incoherent with every other wavelength. The result of this mutual incoherence is that polychromatic fringes are a sum of fringes produced by each individual wavelength of light. Since a fixed δ will result in a different phase offset between the two apertures for each wavelength of light (i.e. $\phi = k\delta$), it is impossible to keep fringes arising from different wavelengths of light in phase everywhere. Polychromatic fringes are only present in the neighborhood of zero delay and are attenuated as δ increases. In fact, the fringes are attenuated by an envelope function which takes the shape of the Fourier transform of the spectral bandpass. For the case of a top-hat bandpass centered at

λ_0 and with a width of $\Delta\lambda$, the envelope takes the shape of a sinc function, and fringes are detected inside the coherence length

$$\Lambda \equiv \frac{\lambda_0^2}{\Delta\lambda}. \quad (4.3)$$

For a typical case of five spectral channels in the K band, $\Lambda \sim 25\lambda$ (see Table 4.2). This imposes a strict requirement on the implementation of interferometric measurements. In general, the path lengths of light incident on different telescopes must be similar to within Λ before being combined if fringes are to be observed at all. Even more strictly, δ must be less than $\frac{\lambda}{B_{\text{proj}}}$ if the central unattenuated “white-light” fringe is to be observed. This necessitates delay lines to precisely correct for the optical path length difference between the two apertures. Further, the existence of a coherence envelope also imposes a restriction on our field of view. For a Michelson Interferometer the field of view can be calculated according to

$$\text{FOV} = \frac{\Lambda}{B_{\text{proj}}}. \quad (4.4)$$

Table 4.2 lists Λ and the corresponding field of view for each of the modeled spectral channels using the Keck Interferometer.

Atmospheric turbulence induces a differential delay between the two telescopes, $\delta_{\text{atmosphere}}$, which is variable on timescales of $t_{\text{turb}} \sim \frac{D}{v_{\text{wind}}}$, with D the diameter of each aperture and v_{wind} the wind velocity. If an exposure time of longer than $\sim t_{\text{turb}}$ is required, the delay lines at the interferometer, which are responsible for keeping $\delta \approx 0$, cannot only compensate for sidereal motion or else fringes will be smeared; atmospheric delay must be detected and corrected for dynamically.

Because the Galactic Center is faint, a dual field system is required to incorporate a bright reference star for fringe tracking. In dual field phase referencing (DFPR) a field separator is used to create two beam trains, one with a bright reference source and one with a fainter science target. Similar to natural guide star adaptive optics, light from the bright reference star is used to detect and measure the differential atmospheric delay. These measurements are enabled by the high flux of the reference source, which allows for short exposures of less than t_{turb} .

Table 4.2. Coherence Length

λ_0 [microns]	$\Delta\lambda$ [microns]	Λ [microns]	Field of View [mas]
2.0	0.087	45.97	141.99
2.09	0.091	48.00	148.25
2.18	0.095	50.02	154.49
2.28	0.099	52.50	162.15
2.38	0.104	54.46	168.21

Note. — The central wavelength and width of the spectral channels for our observations. Also shown are the corresponding coherence length and implied field of view. As we will see in Section 4.3.2, the true limiting factor for our field of view will be the fiber response function which is modeled to have a full width at half maximum of 55 mas.

Precise metrology is required for the application of a dual field system. Delay line commands need to be precise on the order of a fraction of the fringe spacing, which is typically ~ 0.03 microns for our scenarios observing in the K band. Also important, a precise baseline measurement is needed to perform the conversion from delay offset of the reference fringes to a delay line command in the science beam. The situation is complicated since there are two beamtrains, each with distinct path lengths which must be measured continuously to monitor fluctuations due to thermal drifts and other effects.

4.3.2 Sources of Uncertainty for Phase Referenced Interferometric Imaging

Visibility measurements entail measuring the amplitude and phase of interference fringes using a light detector. Any corruption of fringe amplitude, fringe phase, or flux levels on the detector must be taken into account. Below we describe all such influences considered.

A fringe-tracker measures the phase of the fringes in the reference beam and sends corrections to delay lines. The finite servo bandwidth in the fringe-tracker will cause the observed fringes to be smeared, and lowering the observed amplitude by a factor

which we take to be:

$$C_{\text{servo}} = 0.75, \quad (4.5)$$

consistent with the performance of phase referencing at the Palomar Testbed Interferometer (Lane and Colavita, 2003).

In DFPR the reference source and the science target are observed through different portions of the atmosphere, each with slightly different piston aberrations (anisopistonism, Esposito et al., 2000; Colavita, 2009). Thus the assumption that light from the science target can be held in phase by monitoring the phase of the brighter reference source will introduce an error. This error will smear the fringes and reduce the modulus of the visibility. The size of this effect is discussed in Esposito et al. (2000) and Colavita (2009) and is given as

$$C_{\text{aniso}} = \exp(-0.44(\frac{\theta}{\theta_p})^2) \quad (4.6)$$

where θ_p is the isopiston angle given by Esposito et al. (2000), and θ is the angle to the reference star.

After the cophased beams are combined, the light passes through single-mode fiber optic cables and then to the camera. Fibers respond best to on-axis sources and transmit only a fraction of the light from off-axis sources. This reduces the observed flux of each source by a factor of $F(\alpha, \beta)$, where F is the fiber function defined below and α and β are the position of each source relative to the phase center. We model the fiber response function as achromatic with a Gaussian function having a full width at half maximum of 55 milliarcseconds:

$$F(\alpha, \beta) = \exp(-4 \log(2) \frac{\alpha^2 + \beta^2}{(55\text{mas})^2}). \quad (4.7)$$

Pointing errors also affect our astrometric precision. In interferometry, pointing errors are manifest as phase errors in the complex visibilities. We account for phase errors arising from a handful of instrumental effects primarily related to measuring and monitoring the baseline and internal paths. We label the combined contribution of these effects $\sigma_{\text{metrology}}$. Another phase error that affects our ability to point arises due to the different paths light from separate sources take through the atmosphere.

As discussed by Shao and Colavita (1992), the uncertainty in the observed phase of interferometric fringes can be written as

$$\sigma_{\text{atmosphere}} \approx 300 B^{\frac{-2}{3}} \theta t^{\frac{-1}{2}} \text{ arcseconds}, \quad (4.8)$$

where B is the projected baseline in meters, θ is the angular separation between the science target and a reference source in radians, and t is the integration time in seconds. This relationship is calibrated using models of the atmosphere above Mauna Kea. We combine the two sources of phase error to produce a total pointing error:

$$\sigma_{\text{point}}^2 = \sigma_{\text{metrology}}^2 + \sigma_{\text{atmosphere}}^2. \quad (4.9)$$

We measure the visibility amplitude and phase using the four-bin ABCD algorithm (Colavita, 1999). In the ABCD algorithm the average intensity in each quarter fringe (A,B,C,and D) is measured and used to deduce the complex visibility. The real and imaginary parts of the visibility can be calculated according to:

$$\text{Re}\{V\} = A - C, \quad (4.10)$$

and

$$\text{Imag}\{V\} = B - D. \quad (4.11)$$

Since each measurement A through D is a flux measurement, each is susceptible to normal photometric uncertainties including Strehl fluctuations, photon noise, and readout noise. We assume $\sigma_{\text{Strehl}} = 10\%$ injection fluctuations, which account for Strehl variations and for the variable coupling of speckles from bright sources beyond our field of view into the fiber (speckle coupling). We assume an average Strehl in the K band of 35%. While this value of the Strehl is consistent with typical values in previous laser guide star AO observations (e.g Ghez et al., 2005), it may represent an optimistic estimate for performance with ASTRA. This is because reported Strehl ratios in the literature are likely to be biased high by frame selection. In our simulations, a reduced Strehl ratio will result in a lower level of flux in the fringes. In our results section below, we demonstrate how our performance scales with flux

by modeling two starfields which are identical except that in one all source fluxes have been scaled by one magnitude.

Bright stars on the periphery of our field of view also have the potential to affect our simulated visibilities. This is because, as shown in Table 4.2, the interferometric coherence envelope extends out to a radius ~ 70 mas and because the fiber will have at least some response there. We assume that such bright sources at large radii have already been detected with laser guide star AO observations and that their effect on our visibilities could be modeled out accordingly.

We report our modeled background flux levels in each spectral channel in Table 4.3. They are based on observed background performance using the Keck Interferometer fringe tracker (e.g. Woillez et al., 2012). The read noise, σ_{rdnz} , is taken to be 10 counts, consistent with the performance of the Hawaii arrays at Keck. Thus we take the uncertainty in each read in each spectral channel to be

$$\sigma_{\text{detect}}^2 = t_{\text{int}} \left(\sum_j (F(\alpha_j, \beta_j)(0.35 + \eta_1 + 0.35 + \eta_2)(P_j)) \right) + P_{\text{bg}} + \sigma_{\text{rdnz}}^2 \quad (4.12)$$

where j indexes each source in the field, α_j and β_j are the position of each source on the fiber, P_j is the flux on each aperture emanating from each source, and P_{bg} is the background flux. The exposure time t_{int} is the time spent on each read, and η_1 and η_2 are sampled values of the injection fluctuations drawn from a Gaussian distribution of standard deviation σ_{Strehl} .

Our modeled observational setup uses 60 five-second subreads per 300-second block. Each subread includes one second of integration on each fringe quadrature and one second on a bias frame. A summary of our simulator parameters can be found in Table 4.3.

4.3.3 Producing Mock Fringes

In the previous section, we described the magnitude of several corrupting influences including several random noise sources. Actual values for each of these random sources of noise must be realized before we can produce our simulated fringes. We assign to the variable ϕ_{err} a sampled value of the random pointing error drawn from

a Gaussian distribution of width σ_{point} . For each aperture we draw a value for the random injection fluctuation from a Gaussian of width σ_{Strehl} ; we assign these values to the variable η_i , where i indexes the aperture. Finally, we generate a value, n_{detect} , for the detection noise by drawing from a Gaussian distribution of width σ_{detect} .

Next, we combine the random noise sources with calculated values for C_{aniso} , the fiber attenuation function, and the visibility of each individual point source to model and measure the fringes as follows

$$\hat{E}(\delta) = t_{\text{int}}((0.5 + \eta_1)P + (0.5 + \eta_2)P + 2\sqrt{(0.5 + \eta_1)(0.5 + \eta_2)P^2}|\hat{V}| \cos(k(\arg(\hat{V}) + \delta))) \quad (4.13)$$

where the amplitude and phase of the fringes are specified by the complex visibility given by

$$\hat{V} = \frac{\sum_j F(\alpha_j, \beta_j) P_j C_{\text{servo}} C_{\text{aniso}} V_{\text{point}}(\alpha_j, \beta_j, u, v) e^{2\pi i \phi_{\text{err}}}}{\sum_j F(\alpha_j, \beta_j) P_j}. \quad (4.14)$$

Here $V_{\text{point}}(\alpha, \beta, u, v)$ is the complex visibility of a point source (see e.g. Lawson, 2000), t_{int} is the exposure time (1 second in our model). The quadratures are then determined using

$$\hat{A} = \frac{\int_0^{\frac{\pi}{2}} \hat{E}_A(\delta) d\delta}{\frac{\pi}{2}} + n_{\text{detectA}} \quad (4.15)$$

$$\hat{B} = \frac{\int_{\frac{\pi}{2}}^{\pi} \hat{E}_B(\delta) d\delta}{\frac{\pi}{2}} + n_{\text{detectB}} \quad (4.16)$$

$$\hat{C} = \frac{\int_{\frac{3\pi}{2}}^{\pi} \hat{E}_C(\delta) d\delta}{\frac{\pi}{2}} + n_{\text{detectC}} \quad (4.17)$$

$$\hat{D} = \frac{\int_{\frac{3\pi}{2}}^{2\pi} \hat{E}_D(\delta) d\delta}{\frac{\pi}{2}} + n_{\text{detectD}} \quad (4.18)$$

For each hour angle and wavelength observed, the real and imaginary parts of the visibility are then reported as $\hat{A} - \hat{C}$ and $\hat{B} - \hat{D}$ respectively. It is important to note that a new realization of \hat{E} is made for each quadrature, exposing each quadrature to independent injection fluctuations. This inter-ABCD fluctuation affects both the deduced amplitude and phase of the complex visibility, and is often the dominant noise source.

Table 4.3. Parameters

Parameter	Keck	VLTI	Shared
Number of baselines	1	6	—
Time on source each observing night	3 hours	6 hours	—
Blocktime	—	—	300 seconds
Transmission ^a	1.7%	0.9%	—
Fiber full width half maximum	—	—	55 milliarcseconds
Strehl	—	—	35% ^b
Injection Fluctuations (η)	—	—	10%
Background flux rate in each channel	—	—	60, 167, 430, 1112, and 2677 photons/second ^c
$\sigma_{\text{readnoise}}$	—	—	10 counts ^d
Decoherence Due to the servo (C_{servo})	—	—	0.75 ^e
Isopiston angle (θ_p) ^f	13.5 arcseconds	16.1 arcseconds	—
Distance to fringe tracking star (θ) ^g	7 arcseconds	1.2 arcseconds	—
Decoherence due to anisopistonism (C_{aniso})	0.90	0.998	—
$\sigma_{\text{atmosphere}}$ ^h	32 – 42 μas	4 – 7 μas	—
$\sigma_{\text{metrology}}$	20 μas ⁱ	14.5 μas ^j	—

^aDemonstrated at Keck Woillez et al. (2012); GRAVITY reference: Vincent et al. (2011)

^bConsistent with AO performance at Keck (e.g. Ghez et al., 2005), and the expected performance for the GRAVITY instrument (Gillessen et al., 2006b)

^cBackground flux rates refer to the flux in the spectral channels centered at 2.0, 2.09, 2.18, 2.28, and 2.38 microns respectively and are consistent with the observed performance on the Keck Interferometer (Woillez et al., 2012)

^dconsistent with the performance of the HAWAII IIRG arrays (e.g. Woillez et al., 2012)

^eFrom Lane and Colavita (2003)

^fFrom Esposito et al. (2000)

^gIRS 7 at Keck, and IRS 16C at the VLTI

^h $\sigma_{\text{atmosphere}}$ is defined by Equation 4.8 and depends on the projected baseline length and guide star distance. We report the range of values for our 300-second blocks over one night of observing.

ⁱWoillez et al. (2010)

^jDerived using values from Table 3 of Gillessen et al. (2006b) and includes contributions from the narrow angle baseline determination, the beam combiner phase measurements, metrology, dispersion, and relativity.

Note. — Our error values are reported for 300 second blocks. Where applicable they will average down. For example, in three hours, $\sigma_{\text{atmosphere}}$ for Keck Interferometer is $\sim 7.2\mu\text{as}$. For the VLTI in six hours, $\sigma_{\text{atmosphere}} \sim 1\mu\text{as}$ and is a function of baseline (Equation 4.8). For the VLTI we report the mean value for the six baselines.

4.3.4 Observing Routine, UV-coverage, and PSFs

We simulate observations for two instruments: ASTRA at the Keck Interferometer and GRAVITY at the VLTI. For the Keck Interferometer/ASTRA our adopted observing routine assumes 10 visits to Sgr A* per night at even intervals between the hour angles of -1.5 and 1.5. This is the maximum hour angle range for which Sgr A* is above $\sim 50^\circ$ Zenith Angle. For the VLTI, we modeled 20 visits to Sgr A* per night between the hour angles of -3 and 3. This reflects the higher transit of Sgr A* at the location of Cerro Paranal and assumes a similar observational cadence is attainable at both the Keck Interferometer and VLTI. Individual observations are assumed to last 10 minutes with 5 minutes of on-source integration. We model fringes in 5 spectral channels dispersed across the K-band (see Table 4.2). Ten observations in five spectral channels per night provide 50 visibilities from the Keck interferometer. 20 observations in five spectral channels over 6 baselines provide 600 visibilities per night at the VLTI.

The resulting uv-coverage and PSF for the Keck Interferometer is shown in Figure 4.1. The PSF is narrow, ~ 5 mas at half maximum, along the direction of the interferometer baseline, but extended in the perpendicular direction. Because of the distinct shape of the Keck Interferometer PSF, we will measure astrometry much more precisely along the baseline than in the orthogonal direction. The extended wings or sidelobes of the PSF will have the tendency to overlap when the separation between sources has only a very small component along the baseline direction. Such overlapping sidelobes bias astrometric measurements (see below). However, within ~ 50 mas of the Galactic Center, where stars are expected to be orbiting with periods ~ 1 year and $1 - 2$ bright sources are expected in the field, multi-epoch observations with the Keck Interferometer stand a good chance of observing the sources with significant separation along the baseline angle (see Section 4.5.1 below).

The extended wings of the Keck Interferometer PSF shown in Figure 4.1 will result in a restricted contrast limit. This is because flux from a bright source is distributed throughout the field in the wings of the PSF. To be detectable in the vicinity of a bright source, a faint source must be brighter than the noise in the

wings.

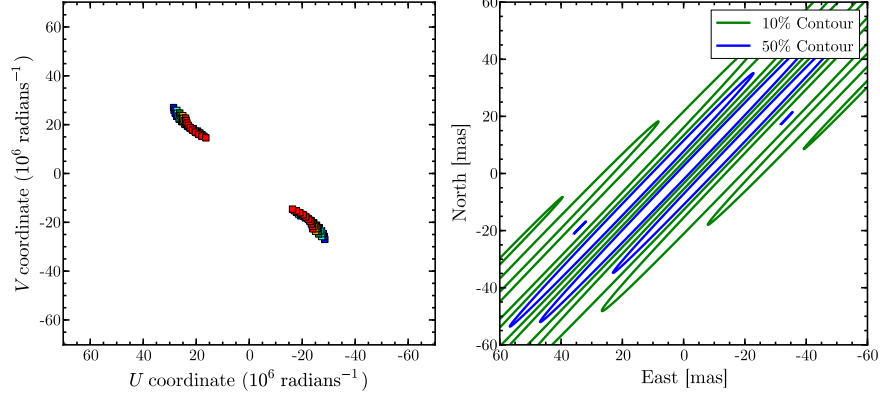


Figure 4.1: The uv-coverage (left), and the 10% and 50% contours of the resulting PSF (right) produced by our adopted observing routine at the Keck Interferometer.

Our adopted VLTI observing routine provides the uv-coverage shown in the left panel of Figure 4.2. The increased uv-coverage provided should have an easier time distinguishing sources in a crowded field.

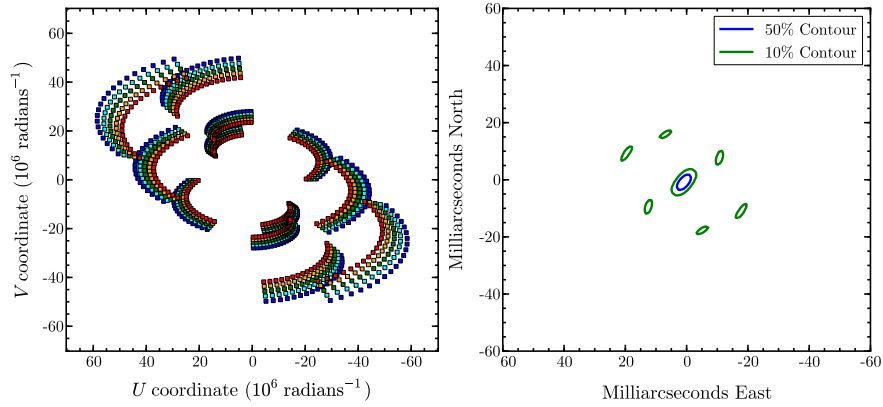


Figure 4.2: Left: The uv coverage provided by the VLTI in six hours of observing the Galactic Center. Right: The 10% and the 50% contours of the synthesized beam.

4.4 Fitting Stellar Positions to Visibility Data

There are four free parameters for each source in the field: position (x, y) , flux, and spectral slope. For real data, the number of sources in the field will not be known a priori. In order to efficiently search the large parameter space for a best fit to the synthesized data, we implement a hybrid grid fit and Levenberg Marquardt (LM) minimization algorithm to minimize the χ^2 function of the parameters given the synthesized data.

The interferometric visibility produced by a distribution of point sources is expected to be undulating versus baseline (Figure 4.4) and thus the χ^2 surface in the x_k, y_k plane is expected to be similarly undulating (see Figure 4.3 for a slice through the range of the χ^2 function in the x_k, y_k plane). Since the Levenberg Marquardt algorithm is a gradient fitting algorithm which always proceeds “downhill” from an initial starting point—which must be supplied by the user—the undulating nature of the χ^2 surface can present a problem because the LM algorithm will converge on a local minimum if the initial parameters are not in the neighborhood of the global minimum. We have therefore adopted a grid-based approach to ensure that starting values supplied to the LM fitter sample the χ^2 surface well enough to ensure at least one seed begins in the neighborhood of the global minimum. Since local minima on the χ^2 surface mirror local maxima in the PSF, local minima will be separated by about the interferometer fringe spacing. Thus, we used a grid spacing of $\frac{\lambda_{\min}}{B_{\max}}$, where λ_{\min} is the shortest wavelength observed and B_{\max} is the longest projected baseline used. Figure 4.3 shows our grid of seed parameters.

To begin, we start with a model consisting of two point sources. For the fit, we seed an LM fitter with a grid of starting locations (shown in Figure 4.3) and a guess of the flux and spectral slope of each source. We then use the best-fit values of this fit together with an additional grid of starting locations to seed a 3-source model fit. This process can then be repeated to fit for any number of sources. We do not know how many sources will be present in real data, so we are guided by the significance of the fits and the deduced flux of the fitted sources. Highly significant fits and sources

with large fitted fluxes are taken to be real, and less significant fits are disregarded.

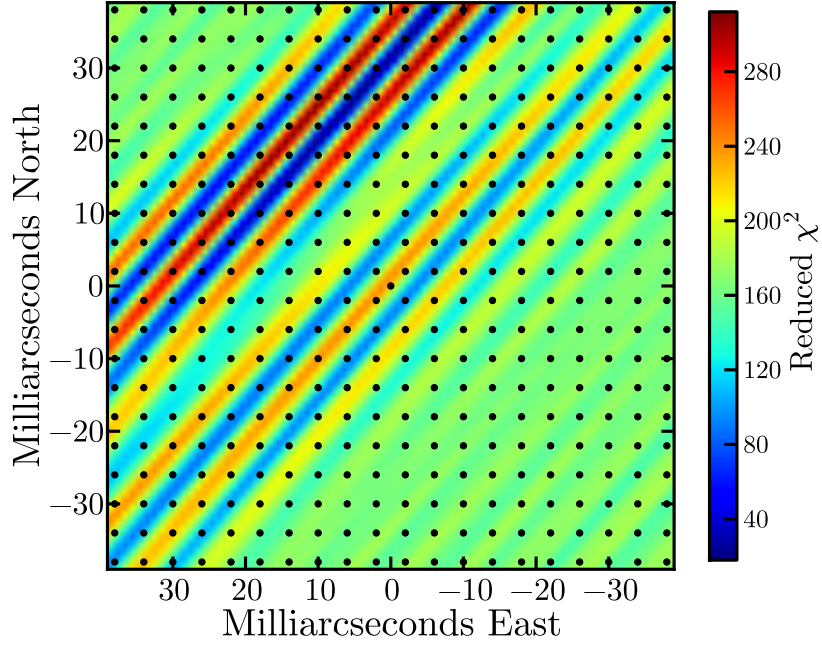


Figure 4.3: A slice through the reduced χ^2 surface for a fit of a two-source model to Keck Interferometer data. The undulations present a hurdle to the naive application of a gradient fitting algorithm since there is the potential to converge on a local minimum. Over plotted on the χ^2 surface is the grid of seed positions provided to the gradient fitting algorithm. The grid spacing ensures that the global minimum is sampled.

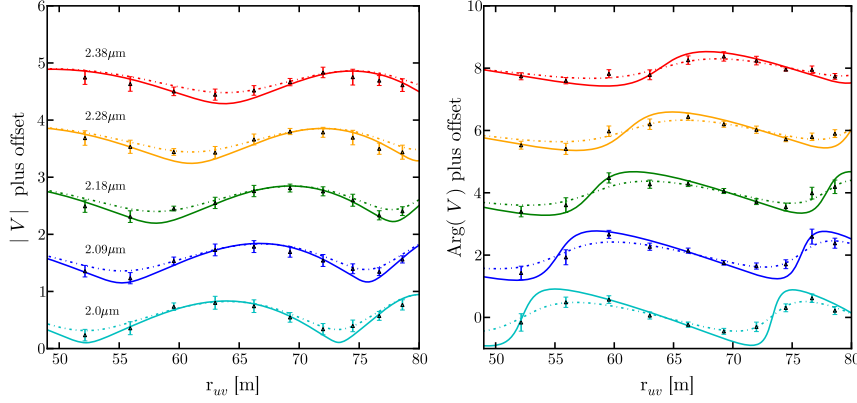


Figure 4.4: The triangular points mark synthesized visibility data with measurement uncertainties for one night of observing with ASTRA at the Keck Interferometer. We generate 50 complex visibility measurements over 3 hours of observation. Each measurement is made with 300 seconds of on-source integration. The average measurement uncertainty in both the amplitude and phase is $\sim 15\%$. The solid curve shows the visibility vs. baseline expected for our star field ignoring instrumental effects. The dashed curve shows the visibility vs. baseline for the star field with the source fluxes scaled by the Gaussian fiber response function.

4.5 Results

4.5.1 Star Fields Observed with ASTRA at the Keck Interferometer

For our simulated Keck Interferometer observations of the orbiting star field Field1, we adopt a two-year observing routine that includes two three-night observing runs per year, one in the spring and one in the late summer. In Figure 4.5 we show our fitted source positions as well as the input positions for one of the nights. The positions of Sgr A* at $m_K = 16.3$ and of Star 1 at $m_K = 16.9$ are recovered (small error ellipses), but the positions of the fainter stars are not recovered (very large error ellipses) and are hereafter disregarded.

Figure 4.6 shows the fitted position for Sgr A* and Star 1 for all 12 nights of observing Field1. The fainter stars have not been plotted because their positions are not recovered by the fitter. The astrometric residuals for Sgr A* and Star 1 are shown in the right panel of Figure 4.6. The astrometric precision in our fits can be estimated

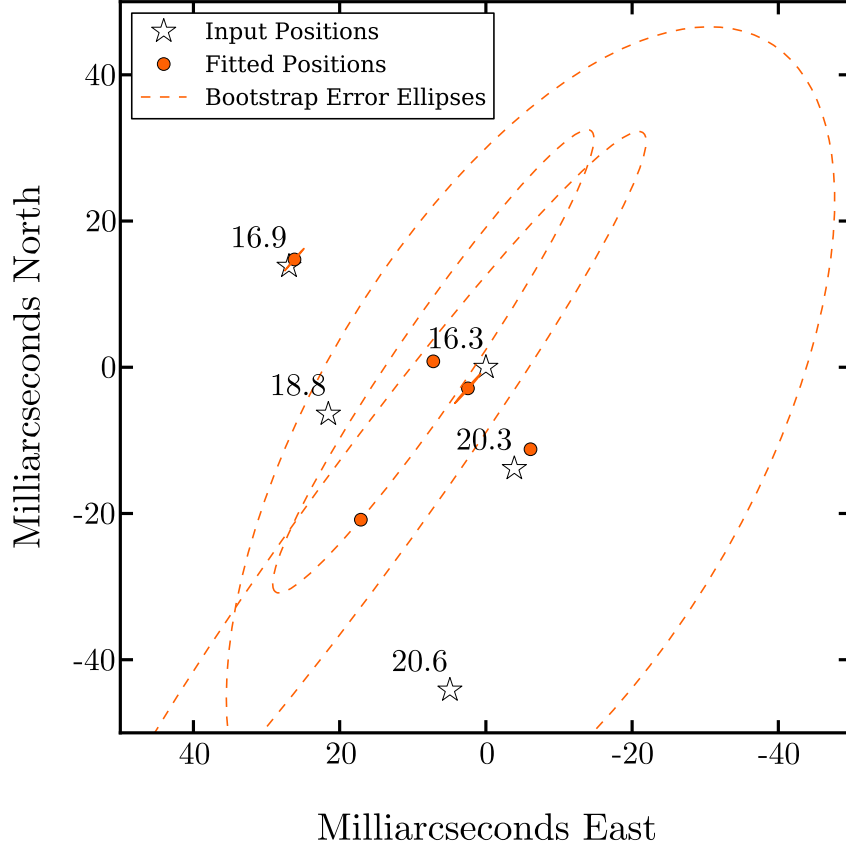


Figure 4.5: One epoch of the orbiting star field Field1 (white star symbols). Our recovered positions and astrometric error ellipses are also plotted (orange symbols). Only the positions of Sgr A* and Star 1 are accurately recovered. The positions of the fainter sources are not recovered. We have plotted the error ellipses of these sources using a dashed line. Note that these dashed curves are error ellipses, and not orbits.

in three ways. First, we are able to characterize the quality of fits by computing the true residuals (right panel of Figure 4.6). Second, by assuming no significant orbital motion over the three-day time period, the dispersion in fitted positions over consecutive nights provides a rough measure of the astrometric precision for each observing run. Lastly, in Figure 4.7 we show calculated error ellipses generated using a standard bootstrapping algorithm.

Bootstrapping randomly re-samples the data, with replacement, several times and

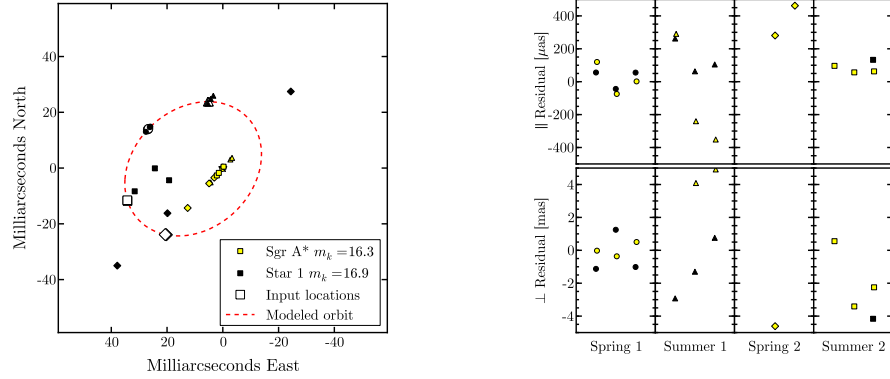


Figure 4.6: Left: We show the recovered positions of Sgr A* (yellow symbols) and Star 1 (black symbols) for four three-night runs of simulated Keck Interferometer data. The fits from each run are plotted with a unique symbol shape. The input orbit of Star 1 is also plotted (red dashed line) together with the expected location of Star 1 for each epoch (larger white symbols). Right: The astrometric residuals along the average baseline direction (top row) and the perpendicular direction (bottom row). Note the change from microarcseconds in the top row, to milliarcseconds in the bottom row.

re-runs the fitter on each new sample. The process of drawing and replacing ensures that for most resampled data sets some of the data is redundant and some of the original data is missing. When our source fitter is run on the re-sampled data sets, a range of fitted parameter values is returned. The spread in the returned parameter values defines the shape of the uncertainty ellipses.

In Figure 4.7 we split the recovered positions shown in the left panel of Figure 4.6 into two plots, the left showing the results from the first year and the right plot showing the results from the second year of observation. We also show the astrometric error ellipses derived via our bootstrapping routine. As expected based on the shape of the Keck Interferometer PSF (Figure 4.1), our ability to accurately recover the position of the star depends on the position angle between the star and Sgr A*. During the first year (left panel of Figure 4.7), Star 1 is well separated in the direction of the baseline from Sgr A* and the astrometric residuals are $\sim 100\mu$ as along the baseline direction and ~ 4 mas in the perpendicular direction. In the second year (right panel) when Star 1 and Sgr A* are not well separated in the direction of

the interferometer baseline, our astrometry is poor as indicated by the larger spread in fitted positions over the three-night runs, the larger residuals, and the significantly larger error ellipses derived for the epochs shown in 4.7. This is due, as discussed above, to overlapping sidelobes. The distinct shape of the bootstrap error ellipses which are much narrower in the direction of the interferometer baseline than in the direction perpendicular, reflects the shape of the Keck Interferometer PSF which has similar features.

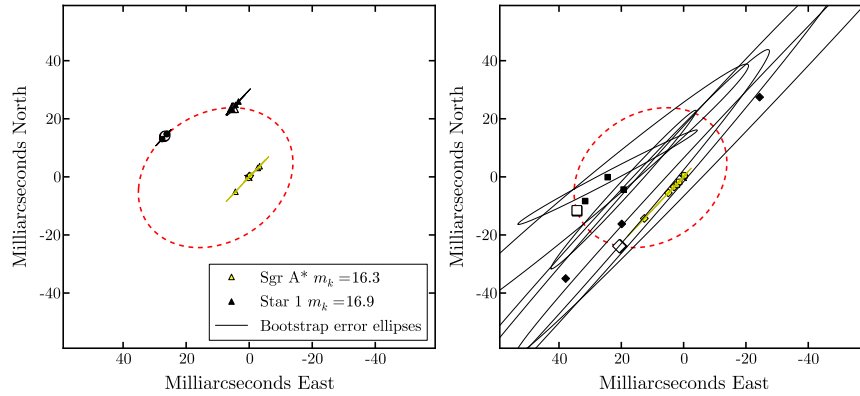


Figure 4.7: We have split the left panel of Figure 4.6 into two parts showing the recovered positions from the first year of data in the left panel, and the recovered positions for the second year of data in the right panel. Astrometric uncertainties for each fitted point are indicated with a solid line. Due to the large sidelobes in the Keck Interferometer PSF (Figure 4.1) our recovered positions are most precise when Star 1 and Sgr A* are well separated along the direction of the interferometer baseline.

We adopt the same observing program as for Field1, namely four three-night runs over two years for our simulated observations of Field2. Our fit to one night's data is shown in Figure 4.8. We recover the position of Sgr A* and Star 1 but we are unable to recover the positions of the fainter stars.

Figure 4.9 shows our fitted positions for Sgr A* and Star 1 for each of the 12 nights of observing Field2. As is the case for Field1, our ability to recover the positions of Sgr A* and Star 1 is hindered when the sidelobes of each source overlap

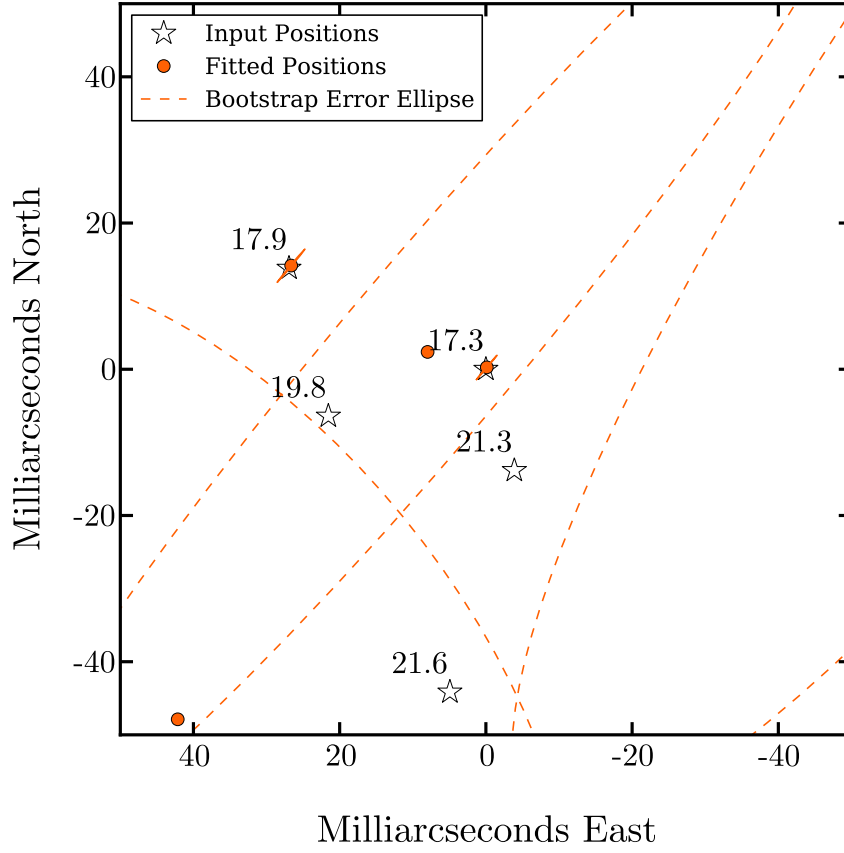


Figure 4.8: This plot is the same as Figure 4.5 but for Field2. We are unable to recover the positions of the fainter stars. The astrometric error ellipses for the unrecovered sources are plotted as dashed lines; note that these are not orbits.

in the Spring and Summer of the second year. In Figure 4.10 we split the left panel of Figure 4.9 into two panels, showing the data from each year separately. For the observations during the first year our astrometric residuals on Sgr A* ($m_K = 17.3$) and Star 1 ($m_K = 17.9$) are $\sim 200 \mu\text{as}$ along the baseline direction and $\sim 4 \text{ mas}$ in the perpendicular direction (first two columns in the right panel of Figure 4.9).

To generate a complete picture of why we are unable to recover the fainter sources, we investigate: 1) the signal-to-noise ratio of each source; and 2) source confusion, which incorporates source density and source contrast.

In Table 4.4 we show an upper limit to the signal-to-noise ratio for each source in

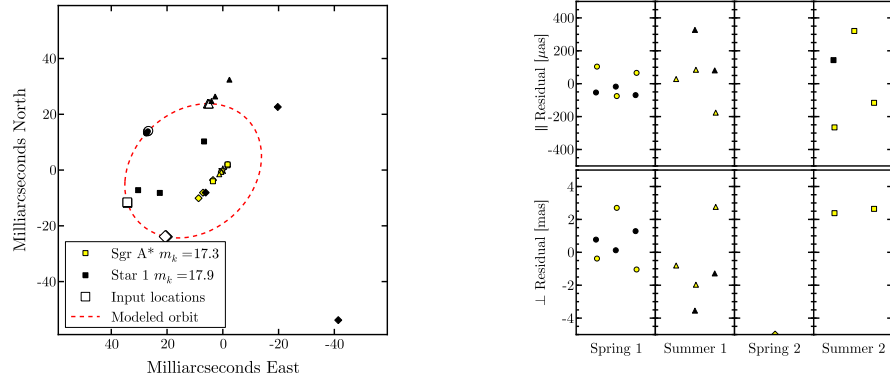


Figure 4.9: Left: Our recovered astrometric positions for each night of observing Field2. Black symbols represent Star 1 recovered positions, and yellow symbols refer to Sgr A* recovered positions. Symbol shapes are unique to each of the four three-day observing runs. Right: The astrometric residuals for each night are shown. Along the baseline direction the residuals are plotted in microarcseconds, while in the perpendicular direction they are plotted in milliarcseconds.

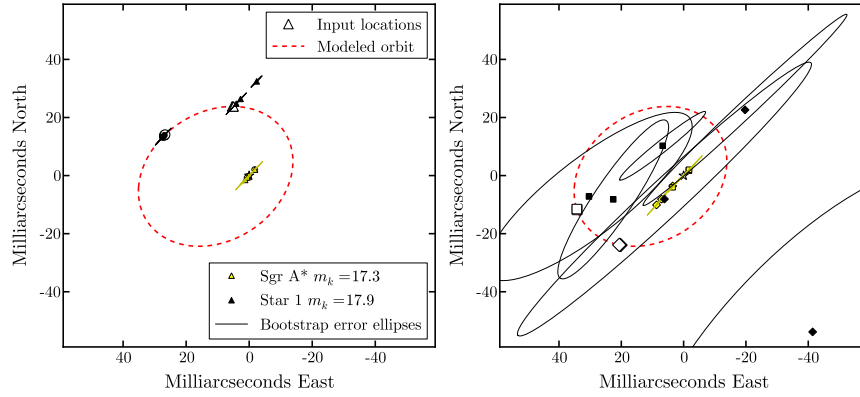


Figure 4.10: In this plot we split the left panel of Figure 4.9 showing the data from the first year in the left plot, and the data from the second year in the right plot. Black symbols still refer to Star 1 recovered positions, and yellow symbols refer to Sgr A* recovered positions. The symbol shapes designate the observing run in the same way as in Figure 4.9. Solid curves indicate the astrometric uncertainty. As discussed, our astrometry is worse in the second year due to overlapping sidelobes.

Field1. To compute the values in Table 4.4 we made some simplifying assumptions

to help elucidate some of the issues without the application of a more opaque formal treatment. Namely, we assume that there is no flux attenuation from the optical fiber and that each source is the only source present in the field. These two assumptions imply that our signal-to-noise ratios are strict upper limits. For example, a source with a reported upper limit to the signal-to-noise ratio of 10 or greater may provide no detectable signal in the presence of photon noise from brighter nearby sources or if the signal of an off-axis source is attenuated by the optical fiber response. Additionally, including only one source in the field assumes a maximum visibility amplitude. With multiple sources in the field the fringe signal is diminished and the signal-to-noise ratio of the fringes of the more complex star field will be similarly reduced. In the limit of a crowded and complex star field, even large values in Table 4.4 do not necessarily imply a high signal-to-noise in simulated data. However, small values do ensure non-detections.

We list signal-to-noise values for each source with and without injection fluctuations. The large change in the upper limit to the signal-to-noise ratio when injection fluctuations are included indicate that they introduce a large source of noise. Since even the upper limits indicate a marginal signal-to-noise ratio for Stars 3 and 4, these sources are likely undetectable in the presence of the brighter sources included in our actual simulated data.

Table 4.5, like Table 4.4 for Field1, illustrates our upper limits to the signal-to-noise ratio simulated for each source in Field2. Even the upper limits on the signal-to-noise ratio indicate that no real signal is detected for Stars 3 and 4.

As we discussed in Section 4.3.4 the sidelobes of the Keck Interferometer PSF will impose a confusion limit in the Keck Interferometer data both because the lobes will set a contrast limit and because they will tend to overlap when sources are not well separated. In Figure 4.11 we show the 1% (red), 10% (green), and 50% (blue) contours of the Keck Interferometer PSF. We also plot the fiber response function and the orbital path of one of our stars. This plot shows that detecting a faint source will be easiest when the star enters a region where the sidelobe flux from Sgr A* is lowest. However, there is the competing factor of the fiber response function which

Table 4.4. Keck simulated data signal to noise for each spectral channel for Field1

Spectral Channel	Sgr A* ($m_K = 16.3$)	Star 1 ($m_K = 16.9$)	Star 2 ($m_K = 18.8$)	Star 3 ($m_K = 20.3$)	Star 4 ($m_K = 20.6$)
Without injection fluctuations					
2.00 microns	246	164	30	7	6
2.09 microns	242	146	26	6	5
2.18 microns	220	120	21	5	4
2.28 microns	200	94	17	4	3
2.38 microns	230	172	32	8	6
With injection fluctuations					
2.00 microns	81	77	29	7	6
2.09 microns	81	75	25	6	4
2.18 microns	80	70	21	5	4
2.28 microns	78	64	16	4	3
2.38 microns	80	78	30	8	6

Note. — This table shows the simulated signal-to-noise values for the sources in Field1. As discussed in the text these values are upper limits and are included here to give a rough feeling of the sensitivity limits. Injection fluctuations dominate the noise for the brighter sources while background and readnoise are significant for the fainter sources. As a convenience, we include the simulated signal-to-noise ratio constructed without any injection fluctuations for reference.

Table 4.5. Keck simulated data signal to noise for each spectral channel for Field2

Spectral Channel	Sgr A* (k=17.3)	Star 1 (k=17.9)	Star 2 (k=19.8)	Star 3 (k=21.3)	Star 4 (k=21.6)
Without injection fluctuations					
2.00 microns	108	70	12	3	2
2.09 microns	103	61	10	3	2
2.18 microns	91	48	9	2	2
2.28 microns	82	39	7	2	1
2.38 microns	102	73	13	3	2
With injection fluctuations					
2.00 microns	68	55	12	3	2
2.09 microns	67	49	11	3	2
2.18 microns	64	42	9	2	2
2.28 microns	60	36	7	2	1
2.38 microns	67	56	13	3	3

Note. — Simulated upper limits to the signal-to-noise ratio for each source in Field2.

tends to attenuate the flux from sources which are located far from the center of the field. Thus while there are some regions in the field beyond the 1% contours of the PSF, detecting a source there is made difficult by the low transmission of the fiber.

An independent limit distinct from contrast but prominent in confusion noise is source crowding. In an attempt to isolate the effects of crowding and provide evidence of whether crowding is limiting all the previous fits, we also simulate data for four star fields, each with a different number of $m_K = 17$ stars. These simulations also provide some insight into the potential performance of the Keck Interferometer if the KLF at the Galactic Center is significantly flatter than Field1 or Field2. The four panels of Figure 4.12 show our fits to these star fields. The star fields were constructed as follows: First, one source with $m_K = 16.3$ is placed at the origin and another with $m_K = 17.0$ is placed randomly within a 100 x 100 milliarcsecond field (panel one). To this star field, an additional $m_K = 17.0$ source is placed randomly in the field (panel two), and so on until a total of four $m_K = 17.0$ sources are present

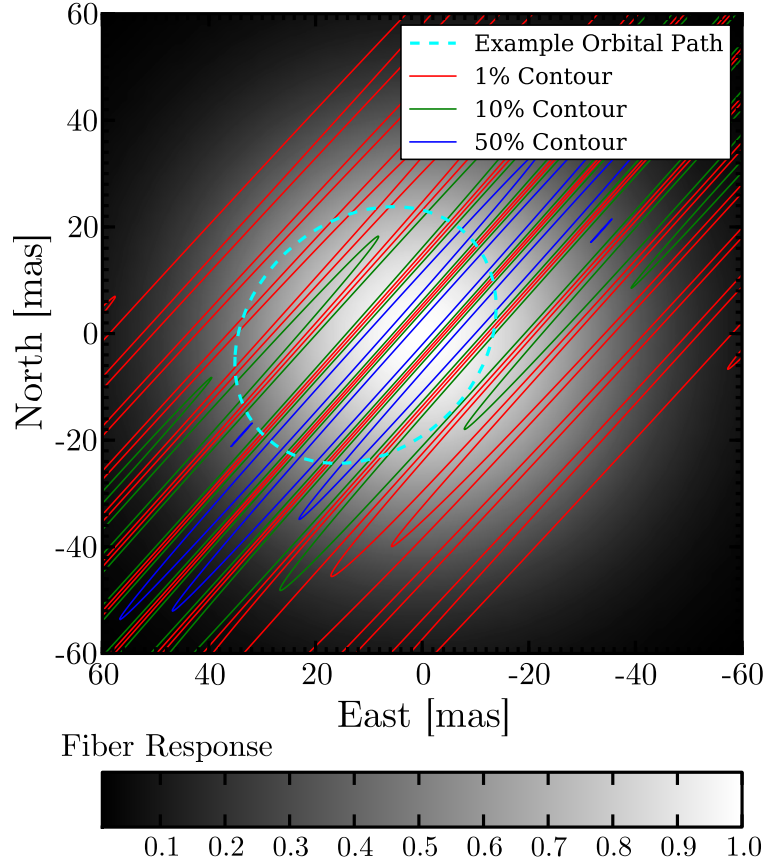


Figure 4.11: In order to illustrate some of the difficulties in detecting a stellar source in orbit about Sgr A* we overplot one of our adopted stellar orbits (cyan dashed curve) on top of the Keck Interferometer PSF (solid red, green, and blue contours at 1%, 10%, and 50% power respectively). We also show the optical fiber response in grayscale.

in addition to the central $m_K = 16.3$ magnitude source (panels 3 and 4).

In panel one of Figure 4.12, our fits to the simulated visibility data recover the input positions of both sources. Our confidence in these fits is implied by the small error ellipses generated by our bootstrapping routine. In panel two, a second $m_K = 17$ magnitude source has been added to the star field beyond the half-maximum radius of the optical fiber attenuation function. Note that due to the fiber function, the flux of the unrecovered star is attenuated by ~ 1 magnitude. We are still able to

recover the positions of the first two sources but we cannot recover the position of this third source due mostly to the increased contrast caused by the fiber-function-attenuated flux. In the third panel, a third $m_K = 17$ magnitude source is added to the field, this time very near the origin. Our fits to this field do recover the positions of the three sources within the half-maximum radius of the fiber function with some confidence; the star placed outside this radius is still not recovered.

The accuracy and the precision of the recovered source positions in panel 3 are somewhat degraded compared to the recovered positions in panels 1 and 2. This degradation in precision is due to the increased crowding of the field with relatively bright sources and the effects of overlapping sidelobes. In the fourth panel of Figure 4.12, with 5 bright sources in the field, the effects of overlapping sidelobes are so severe that we cannot recover the position of any source.

4.5.2 Star Fields Observed with GRAVITY

Figure 4.13 shows the recovered positions for Sgr A*, Star 1, and Star 2 for four three-night observing runs following the same schedule that was used for the Keck simulations. The astrometric residuals (shown in the right panel of Figure 4.13) are $\sim 10 \mu\text{as}$, $\sim 100 \mu\text{as}$, and $\sim 200 \mu\text{as}$ for Sgr A*, Star 1, and Star 2 respectively. In Figure 4.14 we also show the bootstrap error ellipses associated with our fitted positions; where none are seen they are smaller than the plotting symbols. Stars 3 and 4 are not plotted because their positions are not well recovered.

For one run, when Star 2 is farthest from the center of the field, we are unable to recover its position on any of the three nights. The optical fiber transmission function attenuates the flux most during this run. We investigate some of the limiting factors to recovering source positions in GRAVITY data below.

Figure 4.15 shows our results fitting to simulated GRAVITY data of Field2. We plot only the fitted positions for Sgr A* and Star 1 because no other sources were confidently recovered. At input magnitudes of $m_K = 17.3$ and $m_K = 17.9$, our astrometric residuals for Sgr A* and Star 1 are $\sim 50 \mu\text{as}$ and $\sim 150 \mu\text{as}$ respectively.

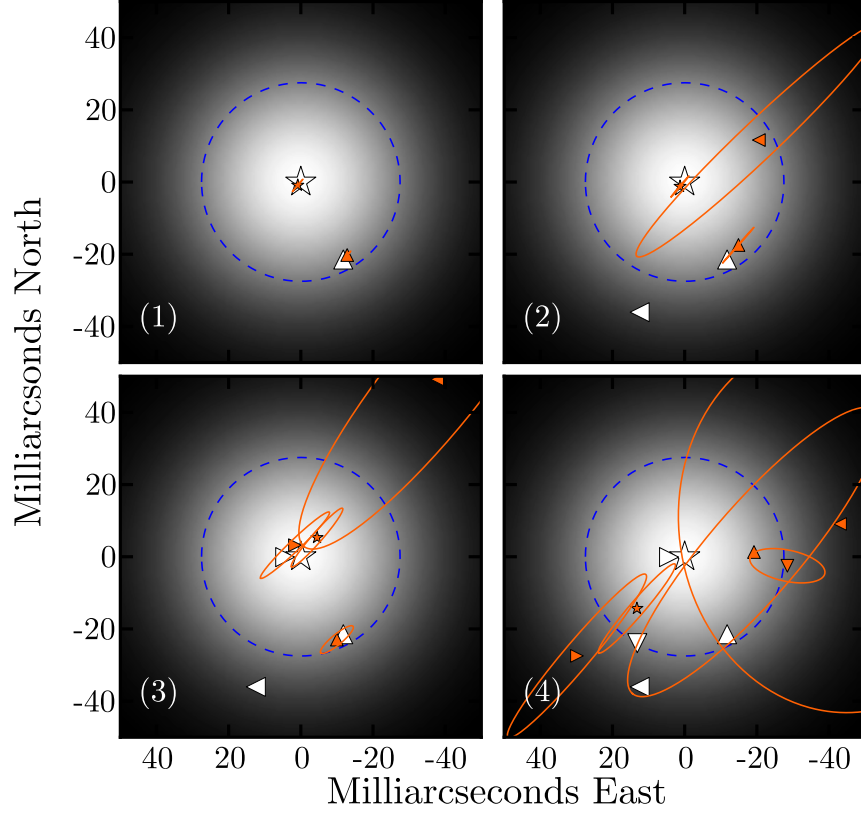


Figure 4.12: In these panels our recovered positions (orange symbols) and error ellipses are plotted showing our performance recovering source positions from Keck Interferometer data when more and more sources are present. The input star field for each panel includes Sgr A* at the origin with $m_K = 16.3$ (star symbol). In addition to Sgr A* each star field also includes from 1 to 4 $m_K = 17$ stars (isosceles triangles with vertices pointing up, right, left, and down corresponding to the first, second, third and fourth added star respectively). Also plotted is the Gaussian fiber response function (grayscale) and the 50% contour of this function (blue dashed line). Source fluxes are attenuated by this function before detection.

To evaluate the limiting factors in our GRAVITY observations, we run diagnostic tests similar to those we perform for our ASTRA simulations. We start by calculating upper limits to the signal-to-noise ratio of each source. Each fringe generated by GRAVITY will have less photons than the corresponding observation with ASTRA

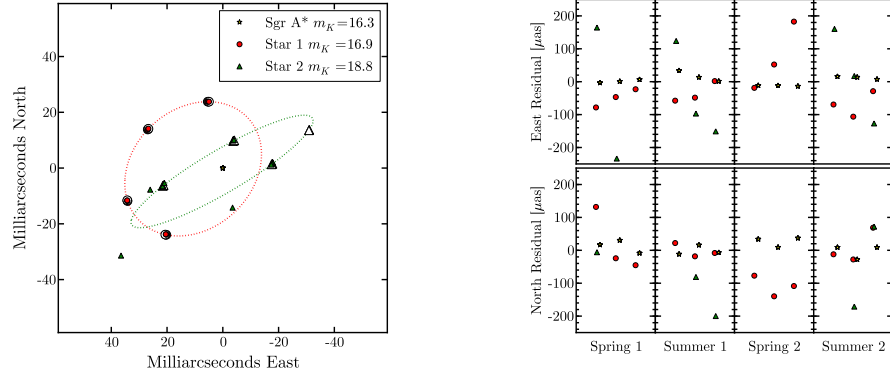


Figure 4.13: This plot is similar to Figure 4.6 but shows the results for our GRAVITY simulations. Left: The recovered positions of Sgr A* (yellow star symbols), Star 1 (red circle symbols), and Star 2 (green triangle symbols) for 12 nights of simulated GRAVITY data. The input orbits of Star 1 and Star 2 are also plotted (red and green dashed lines respectively). White symbols show the input location for each source. Note that in our GRAVITY plots, symbol shape is used to identify sources, not observing epoch. Right: The astrometric residuals in the North and East directions are plotted for both Sgr A*, Star 1, and Star 2.

at the Keck Interferometer. First, because GRAVITY combines the light from four telescopes between six baselines, only $\frac{2}{3}$ of the flux incident on each aperture is available for combination. Second, the individual apertures at the VLTI are smaller than the apertures at Keck. Finally, the transmission of the GRAVITY instrument is expected to be less than the transmission of ASTRA at Keck.

Table 4.6 shows upper limits to the signal-to-noise ratio in our GRAVITY simulations calculated for each source in Field1. We see that for the brightest sources, where injection fluctuations dominate the noise at Keck, GRAVITY will provide a higher signal-to-noise ratio because with 6 baselines, the effect of injection fluctuations averages down. For fainter sources, GRAVITY will provide a lower signal-to-noise because, as mentioned above, the light is split more ways and the transmission is lower. Table 4.6 indicates, even with upper limits to the signal to noise, that Stars 3 and 4 will not be detectable in our simulations.

Table 4.7 shows upper limits to the signal-to-noise ratios for the sources in Field2. These ratios indicate that no detectable signal is present from Stars 2, 3, and 4 in

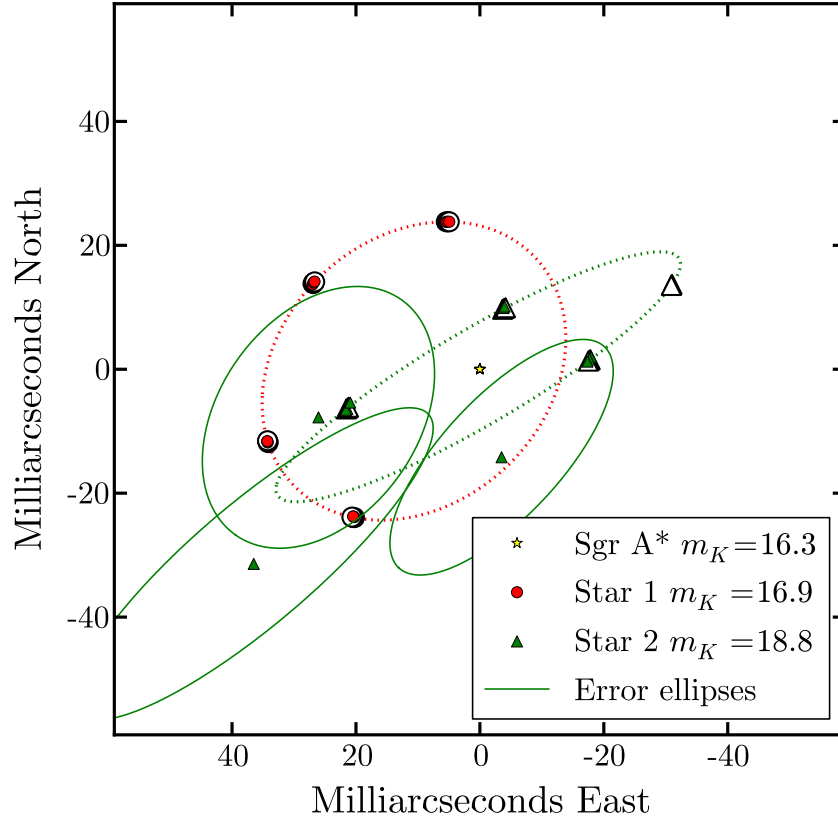


Figure 4.14: The left panel of Figure 4.13 but here we include the bootstrap error ellipses. Where ellipses cannot be seen they are smaller than the plotting symbols. White symbols indicate input locations.

Field2.

In Figure 4.16, we see that our ability to accurately detect and track stars in the vicinity of Sgr A* will depend on the exact location of the star. For example, within 25 mas of Sgr A*, where the optical fiber transmits light most strongly, the PSF is at or above the 1% level. Thus, as in the Keck case discussed above, there is a tug-of-war of considerations affecting the detectability of a source in the vicinity of Sgr A*. Faint sources are more easily detected outside of the 1% contours of the PSF. Because of the fiber attenuation function, when sources are far from the center of the field their flux level is likely to drop below the detection limit ($m_K \sim 19$ in six

Table 4.6. VLTI simulated signal-to-noise ratios for each spectral channel for
Field1

Spectral Channel	Sgr A* (k=16.3)	Star 1 (k=16.9)	Star 2 (k=18.8)	Star 3 (k=20.3)	Star 4 (k=20.6)
With injection fluctuations					
2.00 microns	101	74	12	3	2
2.09 microns	109	69	10	3	1
2.18 microns	102	58	9	4	3
2.28 microns	92	50	9	3	1
2.38 microns	82	40	6	1	1

Note. — This table shows upper limits to the simulated signal-to-noise ratio of each source in Field1 provided by our model of the VLTI GRAVITY instrument.

Table 4.7. VLTI simulated signal-to-noise ratios for each spectral channel for
Field2

Spectral Channel	Sgr A* (k=17.3)	Star 1 (k=17.9)	Star 2 (k=19.8)	Star 3 (k=21.3)	Star 4 (k=21.6)
With injection fluctuations					
2.00 microns	43	30	4	2	0
2.09 microns	43	30	4	1	0
2.18 microns	42	26	3	0	0
2.28 microns	36	18	1	1	1
2.38 microns	33	16	1	0	1

Note. — This table shows simulated upper limits to the signal-to-noise ratio of each source in Field2 provided by our model of the VLTI GRAVITY instrument.

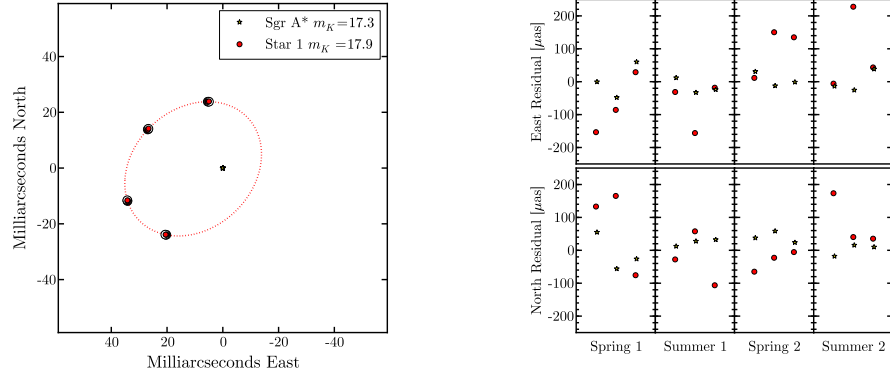


Figure 4.15: This plot is the same as Figure 4.13 but for Field2. In this case only the positions of Sgr A* and Star 1 are recovered. Error ellipses are plotted for each point. White symbols indicate input locations.

hours).

While more beam splits reduce the number of photons combined between each pair of telescopes at VLTI, the trade off is significantly increased uv-coverage. In fact, the confusion limit for GRAVITY will be better than for ASTRA at Keck. In Figure 4.17, as in Figure 4.12 for the ASTRA, we attempt to isolate the contribution of source crowding to the confusion noise by observing star fields with more and more equal magnitude stars. As in Figure 4.12, we start with Sgr A* at $m_K = 16.3$ and one star with $m_K = 17$. We then add one $m_K = 17$ star at a time until a total of four stars are in the field. Since the VLTI provides good uv-coverage of the Galactic Center, precise astrometry on even five bright sources within ~ 50 mas of Sgr A* is possible.

Since Table 4.6 indicates that GRAVITY will be unable to recover Stars 3 and 4 due to inadequate signal-to-noise, we also tested the performance on a brighter star field labeled Field0. Field0 is identical to Field1 but with the flux of each source increased by one magnitude. Our fits are plotted in Figure 4.18. We are again able to recover the positions Sgr A*, Star 1 and Star 2 for three out of four runs. During the run when Star 2 is farthest off axis we again run into some difficulty, because our fitter interchanges Star 2 and Star 3. This is due to the effects of the

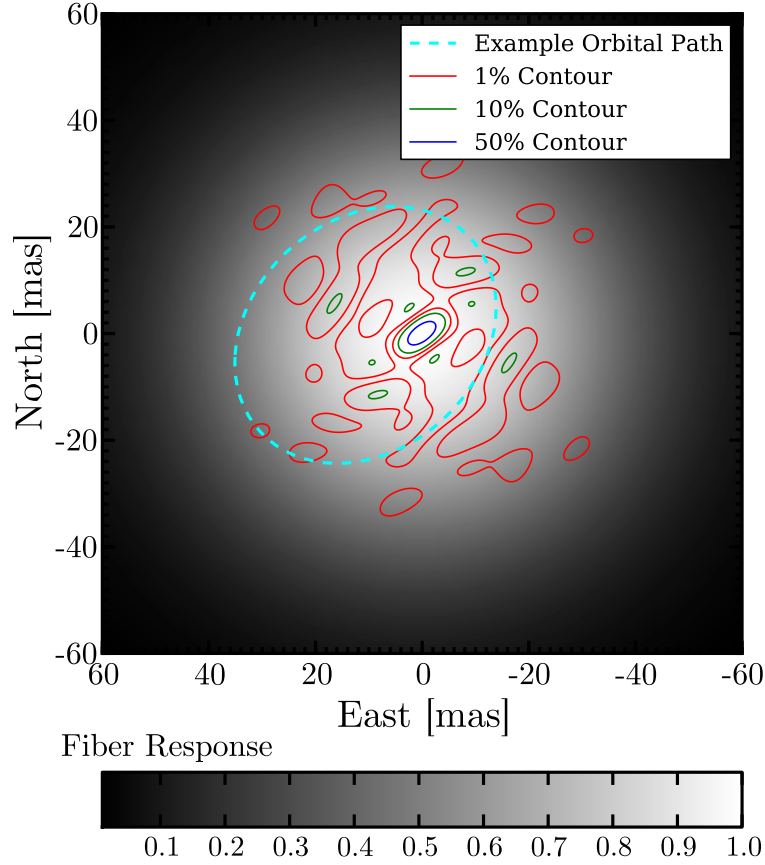


Figure 4.16: This figure is the same as Figure 4.11 but shows the GRAVITY PSF (red, green, and blue contours at 1%, 10%, and 50% respectively). In addition, the fiber response function (grayscale) and an example stellar orbit (cyan dashed line) are also plotted.

fiber response function which attenuates the flux from Star 2 most during this run while Star 3 remains at a nearly constant brightness near the center of the field. The interchange is a result of our iterative fitting algorithm. This interchange does not affect the results of multi-epoch observations which can track the sources and identify the switch.

Star 3 in Field0 is recovered only less than half of the time, indicating that the star is only marginally detectable in the data and suggesting a sensitivity limit around $m_K \sim 19$. Even so, these results imply the potential to detect and monitor several

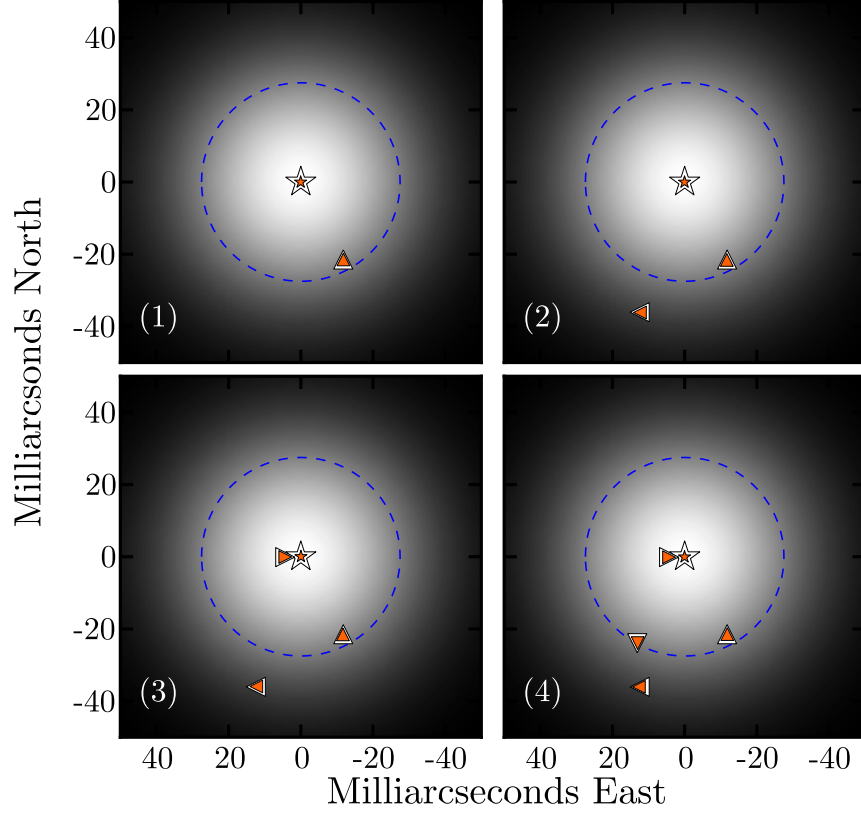


Figure 4.17: Our recovered positions (orange symbols) are plotted showing our performance recovering source positions from GRAVITY data when more and more sources are present. The input star field for each panel includes Sgr A* at the origin with $m_K = 16.3$ (star symbol). In addition to Sgr A* each star field also includes from 1 to 4 $m_K = 17$ stars (isosceles triangles with vertices pointing up, right, left, and down corresponding to the first, second, third and fourth added star respectively). Bootstrap error ellipses are smaller than the plotting symbols. Also plotted is the Gaussian fiber response function (grayscale) and the 50% contour of this function (blue dashed line). Source fluxes are attenuated by this function before detection.

moderately bright sources within ~ 50 mas of Sgr A* should they exist.

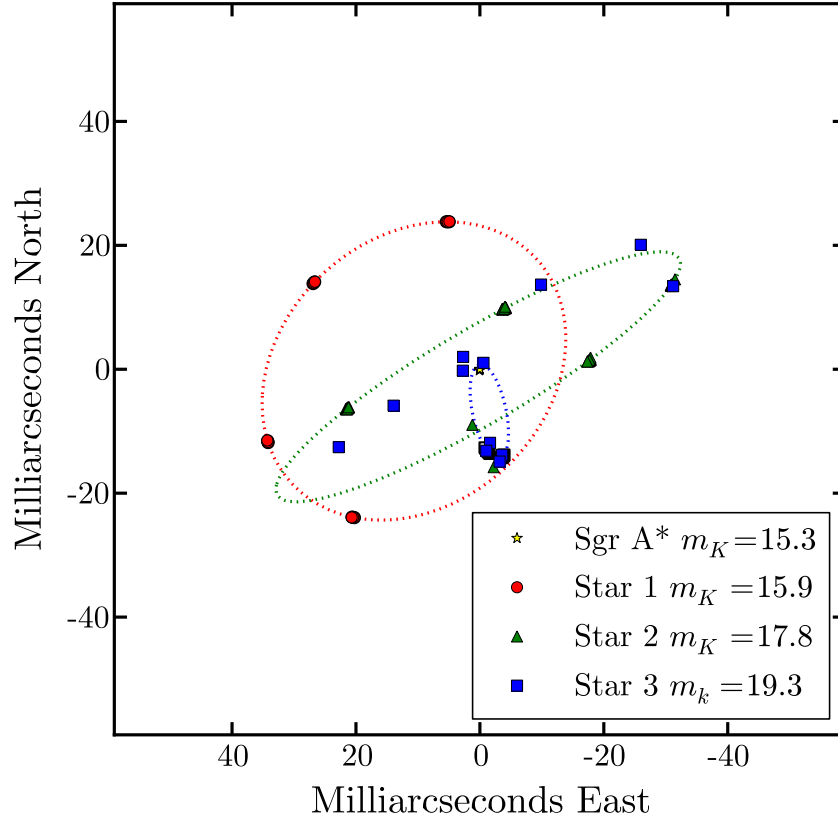


Figure 4.18: Here we show our fits to 12 nights of simulated GRAVITY data for Field0. Some difficulty in deducing the position of Star 2 occurs when it is farthest off axis. During these nights, the flux of Star 2 is most attenuated by the fiber response. Since Star 3 is located close to on-axis for all epochs, it appears as similarly bright to Star 2 during these nights. For two nights during this run, our fitter has interchanged Star 2 and Star 3.

4.6 Discussion

In Section 4.5, our Keck Interferometer ASTRA simulations show the ability to detect and track a stellar source on an orbit within ~ 50 mas of Sgr A* with a single baseline interferometer. This performance depends on the source contrast and position angle with respect to Sgr A*. However, we demonstrate the potential to detect and track an $m_K \sim 18$ star when Sgr A* is at $m_K = 17.3$ and the star and

Sgr A* are well separated along the baseline direction (left panel of Figure 4.10). We show that $\sim 150 \mu\text{as}$ astrometry is possible along the baseline direction and $\sim 3 \text{ mas}$ precision is possible in the transverse direction during unconfused epochs. Our precision improves if the sources are brighter. Since a single baseline interferometer produces an extended PSF, confusion still affects our ability to accurately detect and track sources when their sidelobes overlap.

While at first glance ASTRA seems quite limited compared to GRAVITY in its ability to detect and track stars within $\sim 50 \text{ mas}$ of Sgr A*, we show that the single baseline instrument could significantly contribute to the Galactic Center science case. Specifically, we show that multi-epoch observations have the ability to distinguish whether the region contains no bright sources, one or two bright sources, or several bright sources (see Figures 4.7, 4.10, and 4.12). Since the source content in the region is truly unknown, any additional information about the stellar density near the Galactic Center would be quite valuable. New information could inform, for example, dynamical theories of the nuclear cluster that must explain the positions of the stars. Further, the higher throughput, larger apertures, and fewer beam splits provide a larger signal in the ASTRA fringes (compare for example Tables 4.5 and 4.7). While confusion noise will constrain ASTRA observations, if no star brighter than $m_K \sim 19$ exists in the field ASTRA may have an advantage in making a detection. Because ASTRA is currently capable of making these observations the potential exists to provide the community with some constraints before GRAVITY comes online at the VLTI and before ASTRA operations cease at Keck.

While long-term operations of ASTRA are not currently planned, we note that if ASTRA and GRAVITY observations could be obtained contemporaneously, some improvement in the recovery of faint sources may be possible. In simulations where we combined ASTRA and GRAVITY data (using the assumptions in Table 4.3 for each instrument), we found that we can recover the $m_K = 19.8$ source in some epochs where it is not recovered using either ASTRA or GRAVITY data alone.

Our GRAVITY simulations show that that instrument will attain a lower confusion limit than ASTRA. This lower confusion in GRAVITY observations is due to

the increased uv-coverage provided by the VLTI array. This makes it possible to detect and monitor multiple sources in the field. We demonstrate the potential for $\sim 10 \mu\text{as}$ precision astrometry on Sgr A* at $m_K = 16.3$ and $\sim 100 \mu\text{as}$ precision astrometry on sources as faint as $m_K = 18.8$ in six hours of observing our simulated star fields. However, we show that the decreased throughput at GRAVITY and the larger number of beam splits required to create six baselines will impose a detection limit at GRAVITY which will make it difficult to detect sources at $m_K \gtrsim 19$. In fact, we show that for one simulated three-night run using GRAVITY, we are unable to recover the position of the $m_K = 18.8$ source. While this reflects contrast and fiber function issues to some extent, it shows that in real observations GRAVITY may struggle to detect sources at this brightness level.

GRAVITY’s ability to recover precise astrometry for multiple sources within ~ 50 mas from Sgr A* suggests it should be able to constrain the shape of an extended mass distribution at the Galactic Center (Rubilar and Eckart, 2001; Weinberg et al., 2005). Any model of the central structure must include the mass of the black hole and the mass and radial profile of an extended distribution of matter. To constrain these parameters and to break the first-order degeneracy between the retrograde precession due to the extended matter and the prograde precession attributable to General Relativity, multiple stars with distinct angular momenta will be needed (Rubilar and Eckart, 2001; Weinberg et al., 2005). Since the astrometric signal of orbital precession increases linearly with the number of revolutions, monitoring stars on short-period orbits within ~ 50 mas is preferred, since a larger signal can be detected in shorter time.

Our GRAVITY simulations also demonstrate the astrometric precision needed to detect relativistic effects on stellar orbits. Our simulated performance of $\sim 100 \mu\text{as}$ suggests that low order effects of relativity, such as the prograde precession, will be detectable (Weinberg et al., 2005). However, higher order relativistic effects, such as detecting the influence of the black hole spin on stellar orbits, will be more difficult, requiring measurements more precise than those demonstrated here (Weinberg et al., 2005; Merritt et al., 2011).

A recent paper by Vincent et al. (2011) modeled the imaging mode astrometric performance of GRAVITY, applying the CLEAN algorithm to images formed using the interferometric visibilities. In that paper, the authors mainly investigate the astrometric precision attainable on Sgr A* when it is very bright. They compare their performance after a whole night of observing to individual 100 second exposures. They show that $\sim 40 \mu\text{as}$ precision is attainable on Sgr A* in 100 seconds when it is very bright and the field is simple. Our simulations show that astrometric precision on the order of the angular extent of the inner-most stable circular orbit of the black hole ($\sim 30 \mu\text{as}$) is attainable on Sgr A* even in the midst of our more complicated star field. However, $\sim 10 \mu\text{as}$ precision is attained after 6 hours of observing; time resolved astrometry in our fields will necessarily be less precise. Not only are shorter observations less sensitive to sources in the field, but with less time spent on-source the uv-coverage is reduced. Both of these effects combine to degrade the astrometric precision by decreasing the signal-to-noise ratio and increasing the confusion. We demonstrate that as astrometry on Sgr A* becomes more difficult due to confusion with bright stars in the small field, astrometry on those bright stars becomes easier. Thus GRAVITY should provide some traction on investigating General Relativistic effects, either through observations of Sgr A* itself given a faint star field or by tracking stars in the vicinity of Sgr A* given a brighter star field.

Although our simulations did not include Sgr A* variability explicitly, variability could provide an interesting paradigm for making these observations. During high states, we will be able to conduct precise astrometry of Sgr A*, anchoring our field. During low states, the decreased contrast will provide an opportunity to probe for fainter stellar sources in the region. This back-and-forth approach could be harnessed to precisely monitor faint sources. To demonstrate these effects, we ran our simulator with Sgr A* set to very low brightness but with the star field magnitudes kept constant. During these runs, we were able to recover stellar positions more easily, since confusion with Sgr A* was reduced. On the other hand, a very bright Sgr A* is easily detected with a high level of precision. The timescales of Sgr A* variability are conducive to seeing both high and low states while observing. Flares are observed

on timescales of $\sim 10 - 100$ minutes and Sgr A* often changes flux by more than one magnitude.

4.7 Summary and Future Work

Our simulations demonstrate that ASTRA and GRAVITY will be able to provide different insights into the star field near Sgr A*. The Keck instrument will excel if the inner ~ 50 mas is a simple field, with a steep luminosity function including at least one relatively bright star. We demonstrate the ability to recover a source with $m_K = 17.9$ in a field with other similarly bright sources and we show in Table 4.5 that a source as faint as $m_K = 19.8$ might be detected if the star field is faint and the visibility amplitude is high. Multi-epoch observations will be necessary to mitigate source confusion as the astrometry will be most precise when the star orbits through position angles where the astrometric offset along the projected baseline direction is large. GRAVITY's sensitivity to sources will not depend strongly on orbital phase as is the case with ASTRA since GRAVITY provides a more symmetric PSF. Moreover, GRAVITY will be better able to track orbits if the stellar field has a shallower luminosity function, as it is not as affected by confusion noise and because it will have difficulty detecting sources fainter than $m_K \sim 19$.

The minimal uv-coverage provided by the single baseline of the Keck Interferometer, which is furthermore situated in the northern hemisphere where Sgr A* transits low, is not insufficient for providing valuable information for scientific advance. In fact, we demonstrate the ability to detect and monitor stars when there is sufficient astrometric offset along the baseline direction. These results could be extended to infer the performance of a single baseline of the VLTI. Given the technical and practical challenges of using all four VLT apertures to create six baselines, it is important to consider that even a reduced array at VLTI could make important contributions to Galactic Center science. Because the VLTI is situated in the southern hemisphere where Sgr A* transits high, even a single baseline of the VLTI would provide much more uv-coverage of Sgr A* than Keck. If no bright stars are detected in the region, then a reduced array could be used to provide more photons in each fringe, increasing

the sensitivity of the interferometer at the expense of a more extended PSF, which would even so be less extended than the Keck Interferometer PSF we show above.

Moving forward, further GRAVITY simulations incorporating a variable Sgr A* and stars on post-Newtonian orbits will be useful in the interim before that instrument comes online. Such simulations will aid in predicting the challenges of characterizing the gravitational potential at the Galactic Center with stellar orbits and in creating the necessary analysis tools which will be needed for fitting the complicated orbits which are expected to be observed.

Finally, some interferometric observations of Galactic Center sources have been made at Keck and the VLTI (e.g., Pott et al., 2008b). Pott et al. (2008a) observed IRS 7 with the VLTI and showed it is suitable for use as a phase reference source; similar observations have been made with the Keck Interferometer. Dual field phase referencing has been demonstrated on-sky with ASTRA (Willez et al. in prep), and the instrument is poised to observe the field around Sgr A*. An obvious next step is to actually observe Sgr A* and to search for real sources.

CHAPTER 5

Far Infrared Variability of Sagittarius A*: 25.5 hours of Monitoring with *Herschel*[†]

Variable emission from Sgr A*, the luminous counterpart to the super-massive black hole at the center of our Galaxy, arises from the innermost portions of the accretion flow. Better characterization of the variability is important for constraining models of the low-luminosity accretion mode powering Sgr A*, and could further our ability to use variable emission as a probe of the strong gravitational potential in the vicinity of the $4 \times 10^6 M_\odot$ black hole. We use the *Herschel* Spectral and Photometric Imaging Receiver (SPIRE) to monitor Sgr A* at wavelengths that are difficult or impossible to observe from the ground. We find highly significant variations at 0.25, 0.35, and 0.5 mm, with temporal structure that is highly correlated across these wavelengths. While the variations correspond to $<1\%$ changes in the total intensity in the *Herschel* beam containing Sgr A*, comparison to independent, simultaneous observations at 0.85 mm strongly supports the reality of the variations. The lowest point in the light curves, ~ 0.5 Jy below the time-averaged flux density, places a lower bound on the emission of Sgr A* at 0.25mm, the first such constraint on the THz portion of the SED. The variability on few hour timescales in the SPIRE light curves is similar to that seen in historical 1.3 mm data, where the longest time series is available, but lack a tail of large-amplitude variations seen at longer wavelength. Simultaneous X-ray photometry from XMM-Newton shows no significant variation within our observing period, which may explain the lack of very large variations if

[†]This chapter is based on a manuscript submitted to the Astrophysical Journal by Jordan M. Stone, D. P. Marrone, C. D. Dowell, B. Shulz, C. O. Heinke, and F. Yusef-Zadeh. My roles included developing and implementing calibration strategies, light-curve extraction, and quantitative analysis. I also wrote the article. I benefited from helpful conversations with Dan Marrone, Bernhard Schulz, Darren Dowell and Craig Heinke. I did not participate in the proposal writing process.

X-ray and submillimeter flares are correlated.

5.1 Introduction

Sagittarius A* (Sgr A*) is the luminous source ($L \sim 10^{-8} L_{\text{Edd}}$; Genzel et al., 2010) associated with the super-massive black hole at the center of our Galaxy ($M = 4 \times 10^6 M_{\odot}$, $D = 8.3$ kpc; Ghez et al., 2008; Gillessen et al., 2009b). Due to its mass, relative proximity and faintness, Sgr A* is the premier target for studies of strong gravity, low-luminosity accretion flows, and quiescent galactic nuclei.

Variable emission from Sgr A* arises from deep in the potential well of the black hole in the innermost regions of the accretion flow (Baganoff et al., 2001; Genzel et al., 2003; Doeleman et al., 2008; Fish et al., 2011; Dexter et al., 2014). Thus, features in the light curve of Sgr A* could provide a powerful probe of both the physics of the flow and the gravitational potential around the black hole, yet the nature of the variability is not fully understood.

Constraining the radiative mechanisms responsible for the luminosity of Sgr A* is complicated by the difficulties associated with measuring the spectral energy distribution (SED). At many wavelengths, Sgr A* is either obscured by the galaxy or confused with gas (radio and X-ray), dust (submillimeter), or stars (near-infrared), and source variability imposes a need for simultaneous observations in as many bands as possible. Many groups have coordinated multi-facility observing campaigns to constrain the shape of the quiescent, or time-averaged, SED and the spectral shape of variable emission (e.g., Falcke et al., 1998; Eckart et al., 2004; An et al., 2005; Eckart et al., 2008; Yusef-Zadeh et al., 2006; Marrone et al., 2008; Dodds-Eden et al., 2009; Haubois et al., 2012; Brinkerink et al., 2015). The quiescent SED rises from centimeter to millimeter wavelengths, peaks around 0.8mm (in flux density units; Marrone et al., 2006; Bower et al., 2015), and declines through the IR and X-ray, the only other wavelengths where Sgr A* has been clearly detected. The $S_{\nu} \sim \lambda^{-0.5}$ radio spectrum is consistent with optically thick, stratified synchrotron emission (de Bruyn, 1976), and the increasing slope ($S_{\nu} \sim \lambda^{-1}$) near the spectral peak, the “submillimeter bump” (Falcke et al., 1998), has been interpreted as coming from the innermost

regions of the accretion flow (Falcke et al., 1998; Doeleman et al., 2008; Dexter et al., 2010). The transition from optically thick to thin emission appears to occur over a range of wavelengths in the millimeter/submillimeter regime (Bower et al., 2015; Marrone et al., 2006).

Studies of the variability of Sgr A* have revealed some patterns in the changes between wavelengths. X-ray and IR monitoring has shown that X-ray flares are accompanied by IR flares whenever there is simultaneous IR data (Hornstein et al., 2007) but that IR flares are very often not accompanied by X-ray flares. The relationship between millimeter/submillimeter light curves and features in NIR/X-ray light curves is less well understood. Some report evidence for increased emission in the millimeter/submillimeter after spikes in the NIR/X-ray (Yusef-Zadeh et al., 2006; Marrone et al., 2008; Eckart et al., 2008). These authors argue that the delay is due to the adiabatic expansion of a synchrotron-emitting plasma, whose peak emission shifts toward longer wavelengths as the expanding blob cools and becomes less dense. Models including multiple expanding synchrotron-emitting blobs have been tuned to provide adequate fits to simultaneous submillimeter, NIR, and X-ray flares (Eckart et al., 2006, 2009, 2012; Yusef-Zadeh et al., 2006, 2008, 2009). These models often predict that the spectrum of observed flares should peak $\lesssim 0.3$ mm, impossible to constrain from the ground. The expanding blob scenario is consistent with the results of Hornstein et al. (2007), who did not observe a change in the NIR spectral slope during a flare. The absence of a change in spectral slope can be explained with a non-radiative cooling mechanism, such as adiabatic expansion (Marrone et al., 2008). However, other groups do report NIR spectral slope changes during flux increases (e.g., Gillessen et al., 2006a).

Other authors suggest that millimeter/submillimeter light curves are anti-correlated with NIR/X-ray features (Yusef-Zadeh et al., 2010; Haubois et al., 2012). This could be due to reduced millimeter/submillimeter emissivity caused by a reduction of the magnetic field strength or a loss of electrons due to acceleration or escape, all of which are expected outcomes of a magnetic reconnection event (Dodds-Eden et al., 2010; Haubois et al., 2012). Alternatively, the reduced millime-

ter/submillimeter flux density coincident with NIR/X-ray features could be due to obscuration of the quiescent emission region by the excited NIR/X-ray emission region (Yusef-Zadeh et al., 2010). Dexter and Fragile (2013) model time-dependent emission from Sgr A* and show that NIR/X-ray features and submillimeter features arise from different electrons so are not necessarily related, yet they demonstrate how cross-correlation analysis can produce spurious peaks. Thus, not all reported correlations between IR and millimeter/submillimeter wavelengths may be evidence for a physical connection.

Another challenge for ground-based studies of Sgr A* variability is adequately sampling the relevant timescales. Recently Dexter et al. (2014) revealed a characteristic timescale for variability that is similar to the ~ 6 h observing windows available to Northern hemisphere submillimeter telescopes.

Relatively little is known about Sgr A* at the wavelengths probed by the *Herschel* Spectral and Photometric Imaging Receiver (SPIRE, Griffin et al., 2010). SPIRE observes in three bands simultaneously: 0.5 mm, 0.35 mm, and 0.25 mm. A few ground-based observations at 0.45 mm and 0.35 mm have been made when excellent weather provided adequate atmospheric transparency. At 0.45 mm, single dish measurements have detected Sgr A* at ~ 1.2 Jy and at ~ 4 Jy, although ~ 1 Jy uncertainty in the absolute flux density is incurred due to confusion with extended dust emission (e.g., Pierce-Price et al., 2000; Marrone et al., 2008; Yusef-Zadeh et al., 2009). Marrone et al. (2006) made interferometric measurements at 0.45 mm that resolved Sgr A* from surrounding emission. Those measurements revealed a flat 1.3 mm – 0.45 mm spectral slope and detected variability of ~ 3 Jy. At 0.35 mm, atmospheric opacity and confusion with dust are even more severe, yet a small number of measurements have been made from the ground that suggest variability by a factor ~ 3 (Serabyn et al., 1997; Marrone et al., 2008; Yusef-Zadeh et al., 2009).

Both theoretical predictions from model-fits to multi-wavelength flare data (Eckart et al., 2006, 2009), and observational hints from sparse inhomogeneous ground-based observations suggest that the variability of Sgr A* in the SPIRE bands may be stronger than the variability seen at ~ 1.3 mm (the typical variability am-

plitude at 1.3 mm is ~ 1 Jy on long timescales Dexter et al., 2014). SPIRE provides a unique opportunity to test the model predictions and to compile a uniform and sensitive dataset at 0.5 mm, 0.35 mm, and 0.25 mm. In this paper we use 25.5 hours of *Herschel* SPIRE data, together with overlapping X-ray and 0.85 mm observations provided by *XMM-Newton* and the CSO to monitor for variability and constrain the spectral shape of flares.

5.2 Observations and Reduction

The data we present in this paper were collected as part of a multi-facility observing campaign to monitor Sgr A*. The participating observatories included *Herschel*, CSO, *XMM-Newton*, and the SMA.

5.2.1 *Herschel* SPIRE

SPIRE data were collected in two 12.75 hour blocks: the first from 2011 Aug 31 22:04 UT through 2011 Sep 01 10:51 UT and the second from 2011 Sep 01 20:33 through 2011 Sep 02 9:20. Each interval includes 668 scans across the Galactic Center. Table 5.1 shows the observation identifiers (ObsIDs) downloaded from the *Herschel* Science Archive for this work.

We reprocessed the SPIRE data products using the *Herschel* HIPE software to include the extended flux density gain calibration data products in version 3.1 of the HIPE calibration tree. This step normalizes the response of each bolometer integrated over the beam area, rather than to the peak flux density, which is more appropriate for fields with extended emission. We also chose to include the scan turnarounds in our reprocessing and map making. This option provides additional points on the sky where bolometers make overlapping measurements, increasing the constraints on the calibration algorithms.

For each interval, we concatenated all the Level 1 scans from each ObsID for each SPIRE array into a single Level 1 context to feed to the HIPE destriper¹ (Schulz

¹We used the destriper included with the unreleased development version of HIPE 14.0.2035,

Table 5.1. *Herschel* SPIRE ObsIDs

First Interval	Second Interval
1342227655	1342227733
1342227656	1342227734
1342227657	1342227735
1342227658	1342227736

Note. — Observations were split into two intervals separated by 1 day. We reduced each interval individually due to the large computer memory demands of the calibration algorithms included in HIPE.

et al. in prep.). The destriper iteratively determines offsets for all scans crossing the mapped region on the sky. Each scan consists of many detector readouts. The iterations stop when the variances of the readouts within the boundaries of the map pixels cannot be further improved. By running the destriper in “perScan”-mode, individual offsets—we used a 0-degree polynomial—are fitted for each scan of a given detector, compensating for any long-term variations in the scans. We ran the destriper twice, using the output diagnostic table and destripped scans as inputs for the destriper on the second iteration. This provided small improvements.

Although our relative detector calibration is optimized for extended sources, we produced maps calibrated in units of Jy beam^{-1} . To do this, we binned the scans into groups of 4, and made a single map for each bin, resulting in a time resolution of 4.6 min per map. We assigned the same sky coordinates to each pixel in each map, taking care to center the location of Sgr A* in the central pixel.

Preliminary review of the maps revealed motion of the flux density distribution with respect to the pixels. This motion is due to insufficiently reconstructed pointing drifts of the telescope that result in inaccurate sky coordinates associated with each

which provided improved convergence

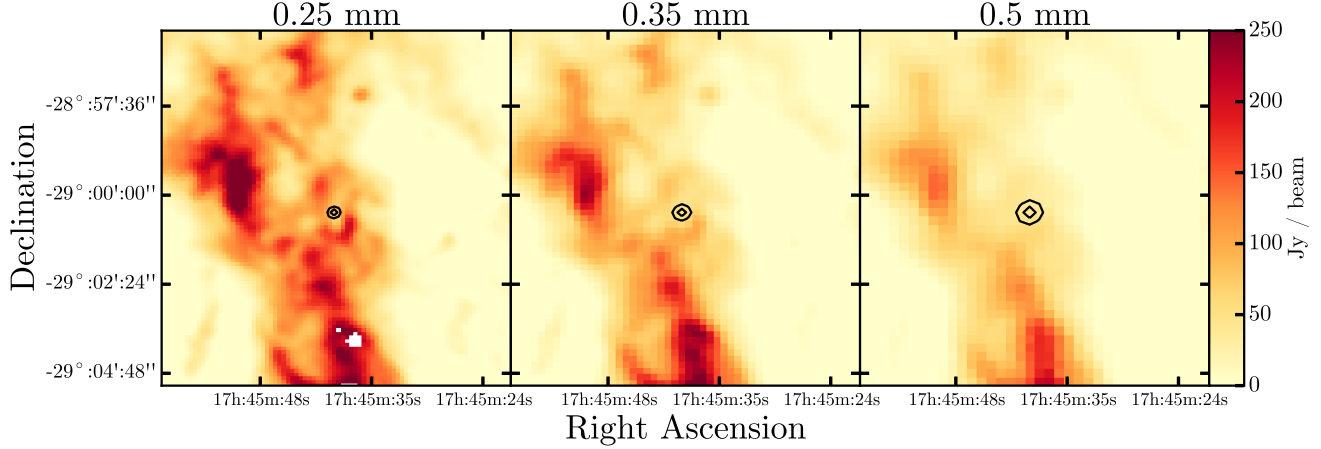


Figure 5.1: *Herschel* SPIRE maps of the galactic center. From left to right are the maps at 0.25 mm, 0.35 mm, and 0.5 mm, respectively. Each map is $11' \times 10'$. On each, we show the 80% and 50% contours of the *Herschel* beam centered at the location of Sgr A*. Sgr A* is not resolved from its surroundings. For some map pixels the strong extended emission from the Galactic Center region exceeded the dynamic range of the SPIRE readout electronics in our chosen instrument setup, which was an accepted trade-off to achieve a maximum sensitivity. This leads to some holes in the 0.25 mm map (white pixels)

bolometer readout. Uncorrected, these drifts limit the precision with which we can calibrate the bolometers and extract light curves.

We solved for pointing offsets as a function of time by shifting each map to best align with the first map produced for each observing interval. Total drifts over the 12.75 hour observing intervals were $\sim 2''$ and $\sim 1''$ for the observations starting 2011 Aug 31 and 2011 Sep 01, respectively. This is consistent with pointing uncertainties given by Sánchez-Portal et al. (2014).

After solving for the best-fit shifts, we updated the coordinates of the SPIRE scans in HIPE and re-ran the destriper and our mapping routine. We iterated the whole process once, and the results showed that our shifts had converged. A small residual drift, $\sim 0.2''$, remains in the data.

Due to the bright extended emission of the Sgr A complex at the Galactic Center, and because of the relatively large beam size delivered by *Herschel* ($18''$, $25''$, and $36''$ at 0.25 mm, 0.35 mm, and 0.5 mm, respectively) Sgr A* is not separated from its

surroundings. However, Sgr A* is expected to be the only intrinsically variable source in our maps (There is a magnetar, SGR J1745-2900, that is about $2.4''$ away from Sgr A*, but the magnetar was in its quiescent phase when these X-ray/submillimeter observations were carried out; Kennea et al., 2013). Therefore, we extract variability light curves from difference images, subtracting the mean map of each 12.75 h observation from the 4-min sub-maps.

We performed photometry on the difference maps by scaling a 1 Jy beam^{-1} reference PSF to best fit our observations. We downloaded the reference beams from the SPIRE public wiki². Specifically, we combined our observed difference maps (D_{ij}), a variance map created by calculating the variance of all bolometer readouts contributing to a given map pixel (σ_{ij}^2), and the PSF (P_{ij}) as follows:

$$\bar{f} = \frac{\sum_{ij} \left(\frac{P_{ij}^2}{\sigma_{ij}^2} \right) f_{ij}}{\sum_{ij} \left(\frac{P_{ij}^2}{\sigma_{ij}^2} \right)}, \quad (5.1)$$

which is the inverse variance weighted mean of the scale factor

$$f_{ij} = \frac{D_{ij}}{P_{ij}}. \quad (5.2)$$

The variance of our measured scale factor can then be computed using

$$\bar{\sigma}^2 = \frac{\sum_{ij} \left(\frac{P_{ij}^2}{\sigma_{ij}^2} \right) (f_{ij} - \bar{f})^2}{\sum_{ij} \left(\frac{P_{ij}^2}{\sigma_{ij}^2} \right)}. \quad (5.3)$$

We extracted light curves from the location of Sgr A* and several reference locations. Reference light curves should show no intrinsic variability so serve as indicators of time variable systematic problems. We chose reference locations as follows: First, we generated 100 random locations within 2 arcminutes of Sgr A*. From that set we excluded any points whose underlying flux density was not within a factor of two of the underlying flux density of Sgr A*. We also excluded points whose underlying gradient had a magnitude that was not within a factor of two of the underlying gradient at the location of Sgr A*. We then searched the remaining locations for a

²<https://nhscsci.ipac.caltech.edu/sc/index.php/Spire/PhotBeamProfileDataAndAnalysis>

maximal set with no two references within $40''$. This ensures that the 0.5 mm beam does not overlap at the 50% level for any of our reference locations. This approach yielded 12 locations on the map for use as references.

We noticed that many of our reference light curves were affected by a small linear trend across the observing interval. This trend was largest in the 0.25 mm band where the average slope was measured to be $\sim -0.02 \text{ Jy h}^{-1}$. The steepest slope removed from our reference light curves was $\sim -0.1 \text{ Jy h}^{-1}$. These values are consistent with the trends expected given the residual pointing drift that remains in the maps and the underlying flux density gradients at the locations of our references. Since these drifts strongly affect the appearance of the inter-band cross-correlations (resulting in relatively high power over a large range of lags) we subtract a best-fit line from each light curve.

Our calculated errorbars (Equation 5.3) were over estimated for each location, including Sgr A*. This was obvious given the magnitude of the point to point variations in the light curves and the much larger size of the calculated errorbars. The over-sized errorbars result from the way that our variance maps are produced. In HIPE, variance maps are produced by binning all bolometer readouts that occur within a given pixel without respect to where within a pixel a readout occurs. In regions of complex structure, such as Sgr A, spatial flux density gradients will lead to variations in flux density values within a pixel, inflating the variance. To account for this, we scaled the errorbars for each reference light curve to provide a good fit to a constant zero-flux model (reduced $\chi^2 = 1$). Typical scale factors were ~ 0.3 . We took the mean scale factor and applied it to the errorbars for the light curve of Sgr A*. This approach provides empirically accurate errorbars that maintain appropriate relative size as a function of time and location on the map.

5.2.2 Caltech Submillimeter Observatory 0.85 mm

Ground-based observations with the SHARC II camera at the CSO provided 0.85 mm monitoring from 2011 Sep 1 04:25 UT through 09:04 UT, and from 2011 Sep 2 03:35 UT through 09:00 UT, overlapping each of our *Herschel* observing intervals.

A $3'$ field surrounding Sgr A* was observed with Lissajous scanning of the telescope with an amplitude of $100''$ and a period of 20 s (Yusef-Zadeh et al., 2006, 2008). On both evenings, the conditions were suitable for observation for the full periods, with clear skies or light cirrus, low wind, and moderate humidity. The zenith atmospheric opacity at 225 GHz was ~ 0.14 on Sep. 1 and ~ 0.10 on Sep. 2. The telescope focus was monitored and, as needed, adjusted during separate observations of point sources, accounting for the gaps in the light curves; the larger gap around 6:00 UT on Sep. 2 was due to a brief observation of Sgr A* at 0.35 mm which did not yield useful results.

Data analysis, including absolute calibration, followed the method described by Yusef-Zadeh et al. (2009). Sgr A* is not well resolved from surrounding dust emission with the $19''$ resolution of CSO at 0.85 mm. This adds ~ 1 Jy uncertainty to the absolute flux level of Sgr A* measured at 0.85 mm, but the measurement of variations is much more precise. Uncertainties for each 0.85 mm measurement were derived from the rms in the image, from which the mean image and a gaussian at the position of Sgr A* have been subtracted.

5.2.3 *XMM-Newton*

XMM-Newton data were collected in two blocks, the first (ObsID 0658600101) from 2011 Aug 31 at 23:37 UT to Sep 1 at 12:58 UT, and the second (ObsID 0658600201) from 2011 Sep 1 at 20:26 to Sep 2 at 10:42 UT. Sgr A* was placed at the center of the *XMM-Newton*/EPIC field of view (away from any chip gaps). The medium filter, and full-frame mode, was used for all three EPIC instruments. The more sensitive pn camera (Strüder et al., 2001) had exposures of 41.9 and 45.2 ks in the two observations, respectively. The less sensitive MOS1 and MOS2 cameras (Turner et al., 2001) had exposures of 48.6 and 52.3 ks in the two observations. Below we focus on results from the pn camera; the MOS results were similar.

The data were processed with the XMM Science Analysis Software (version 11.0.0) to select PATTERN ≤ 12 , energies between 2 and 10 keV, and FLAG=0. We extracted light curves at 300 second binning from a radius of 10 arcseconds (as

typical for Sgr A*, e.g., Porquet et al., 2003), centered at the location of Sgr A*. This radius unfortunately encloses a significant amount of emission unrelated to Sgr A*, both diffuse and point-like; the quiescent flux of Sgr A* (2-10 keV $L_X \sim 2.4 \times 10^{33}$ erg s⁻¹) is only $\sim 10\%$ of the flux enclosed within $10''$ of Sgr A* (Baganoff et al., 2003), but only encloses $\sim 50\%$ of the energy flux from Sgr A* itself (Read et al., 2011).

No statistically significant (3σ) flares were observed in any of the EPIC light curves, and the highest points in each lightcurve did not correspond with the highest points in other light curves. The most interesting possible peak occurred at 4.85 hours into the first observation, reaching 0.153 ± 0.023 counts s⁻¹, compared to an average rate of 0.10 counts s⁻¹. We can thus set an upper limit on the Sgr A* flare luminosity (for flares of 300 seconds in length) during our observations, of 7.6 times the quiescent value, or L_X (2-10 keV) $< 1.8 \times 10^{34}$ erg s⁻¹; longer flares have stricter upper limits ($< 6 \times 10^{33}$ erg s⁻¹ on average for 1 ks flares).

5.2.4 SMA 1.3 mm

In an attempt to provide overlapping 1.3 mm data, Sgr A* was also observed with the SMA. Unfortunately, it was afternoon in Hawaii during our *Herschel* and *XMM-Newton* observations. SMA observing conditions are typically worst in the afternoon because the unstable atmosphere corrupts the interferometer phases. Given the poor quality of the data we can only put a $\sim 30\%$ upper limit on the amplitude of variations of Sgr A* during our observations. This corresponds to ~ 1 Jy, which is about the size of the largest variations seen at 1.3 mm (Dexter et al., 2014).

5.3 Results

We show our average SPIRE maps of the Galactic Center in Figure 5.1. On each map, we overlay contours of the *Herschel* beam at the location of Sgr A*. While the beam size at 0.25 mm is smaller than at the longer wavelengths, the dust emission at this wavelength is significantly stronger. The net result is a more challenging

measurement at 0.25 mm. For an analysis of the dust properties at the Galactic Center, using SPIRE maps as well as additional far infrared data, see Etxaluze et al. (2011).

We show our Sgr A* X-ray and submillimeter light curves for both observation intervals in Figures 5.2 and 5.3. There are significant variations in all of the SPIRE bands. Ground-based 0.85 mm data closely track the SPIRE bands during the first interval. The most significant feature, a flux density decrement, occurs just before 05:00 UT on September 1st, and is captured by both *Herschel* and the CSO, at all four submillimeter wavelengths. We highlight this feature with a vertical dashed line. It aligns in time with a marginal feature in the X-ray light curve, reminiscent of the behavior between the X-ray and longer wavelength data reported in previous studies (Yusef-Zadeh et al., 2010; Haubois et al., 2012). The magnitude of the decrement was nearly the same in all 4 submillimeter bands, ~ 0.5 Jy. This corresponds to 0.6%, 0.8%, and 0.5% of the flux density in the *Herschel* beam containing Sgr A* for the 0.5 mm, 0.35 mm, and 0.25 mm bands, respectively.

The significance of features seen in the SPIRE light curves is supported by cross-correlation. In Figure 5.4 we show the cross-correlation of the light curves for each pair of SPIRE bands, for each observing interval. We show cross-correlations for Sgr A* (black curves), and each of the 12 reference locations (gray curves).

All pairs of Sgr A* light curves are more correlated than pairs from the reference locations. This implies the presence of a shared signal, stronger than the residual systematics that could result in spurious zero-lag correlations for the references (e.g., pointing inaccuracies and thermal drifts). The absence of dominant systematics in these $\sim 0.5\%$ difference measurements is also indicated by the agreement with the independent measurements made by the CSO. Cross-correlation peaks for curves including the 0.25 mm light curve from our first observing interval occur lagged by 4 min, or one sample. All the other cross-correlation curves show zero lag.

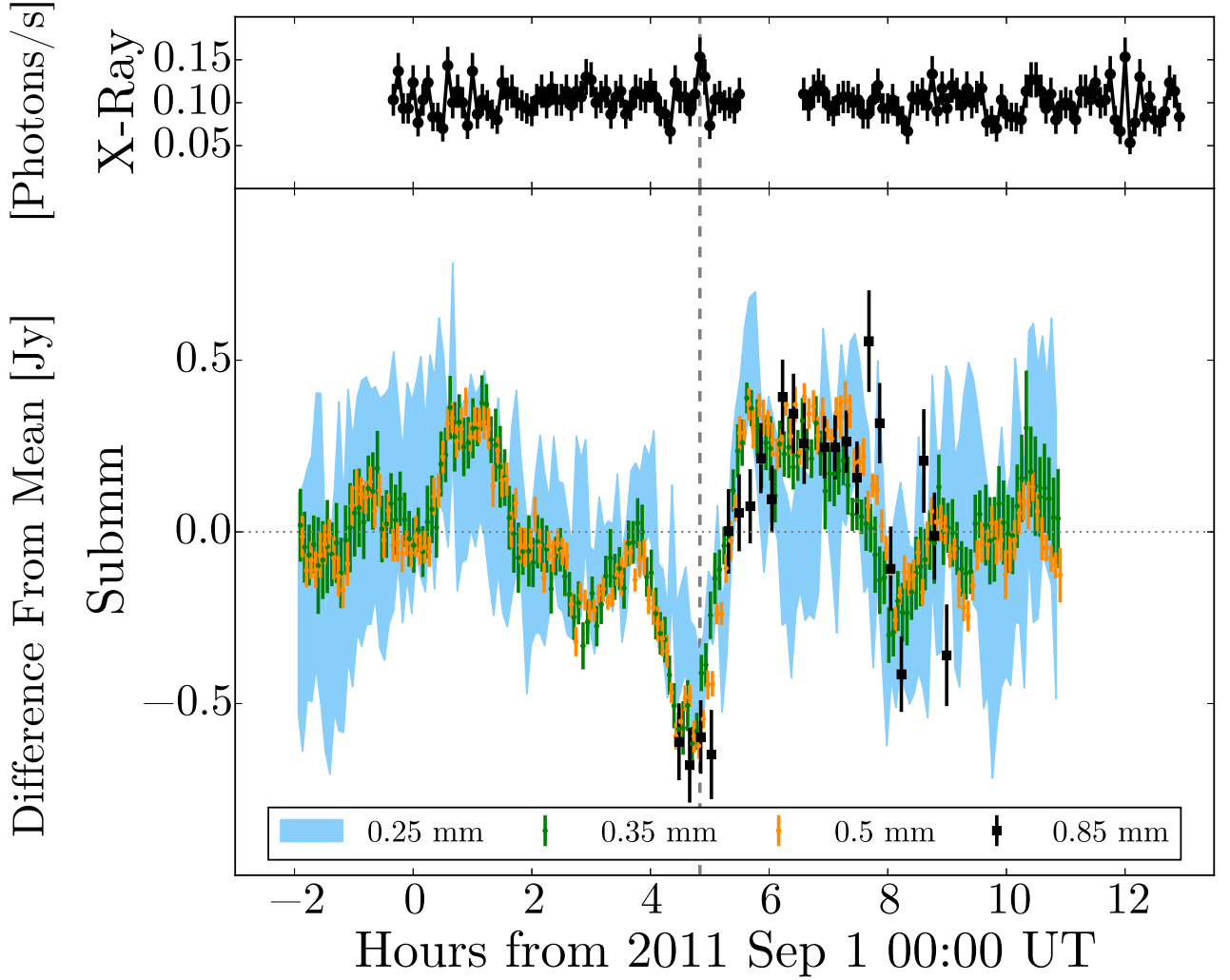


Figure 5.2: Light curves from our first observing interval. Upper panel: *XMM-Newton* pn camera X-ray light curve. Lower panel: SPIRE and CSO submillimeter light curves. For clarity in presenting four overlapping light curves, we have employed two different plotting methods. The 0.25 mm light curve is shown with a light-blue swath that indicates the $1\text{-}\sigma$ confidence region. The 0.35 mm, 0.5 mm, and 0.85 mm light curves are displayed with dots and errorbars indicating $1\text{-}\sigma$ confidence. The SPIRE bands have each been offset slightly in time to avoid overlap.

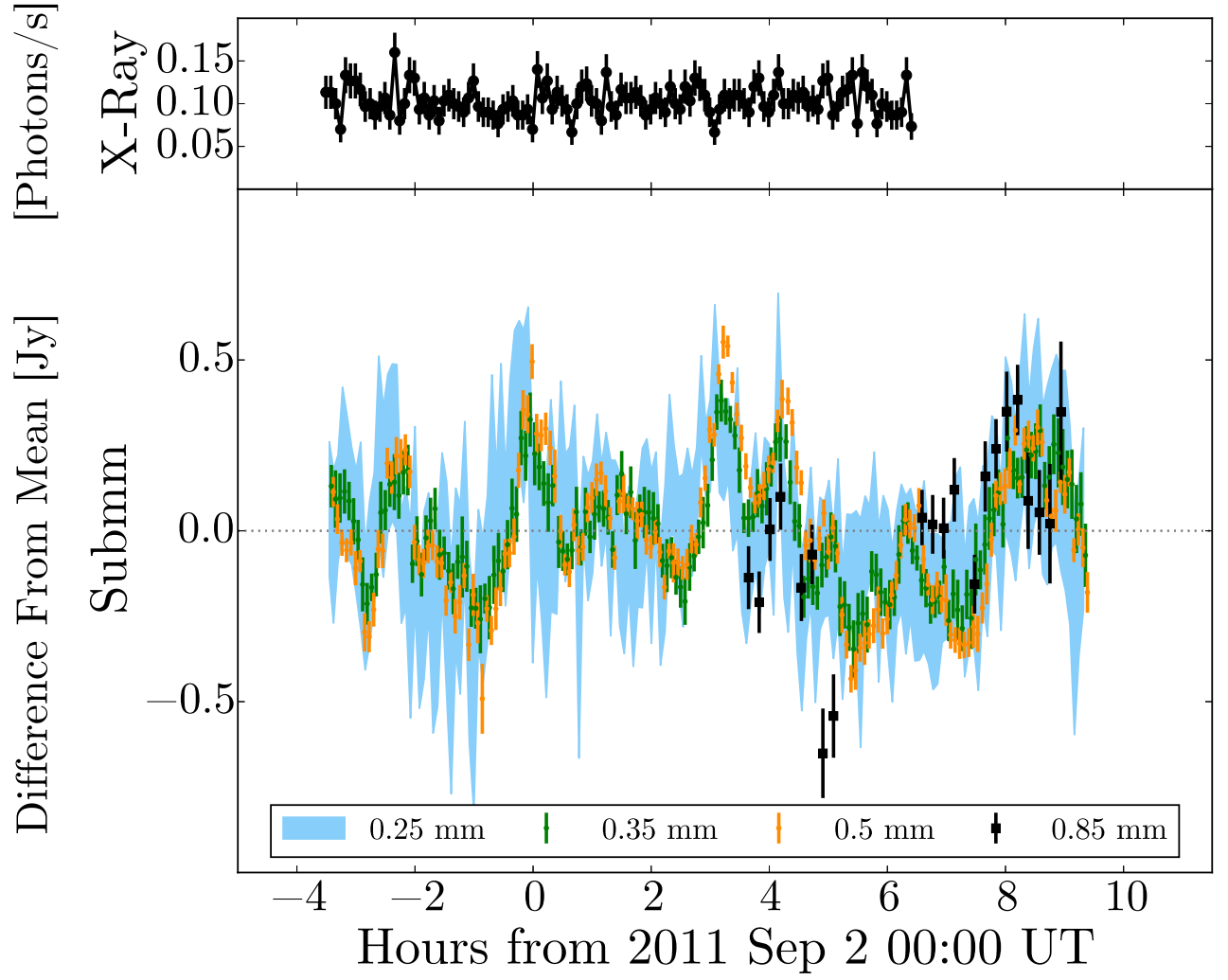


Figure 5.3: Same as Figure 5.2 but for our second observing interval.

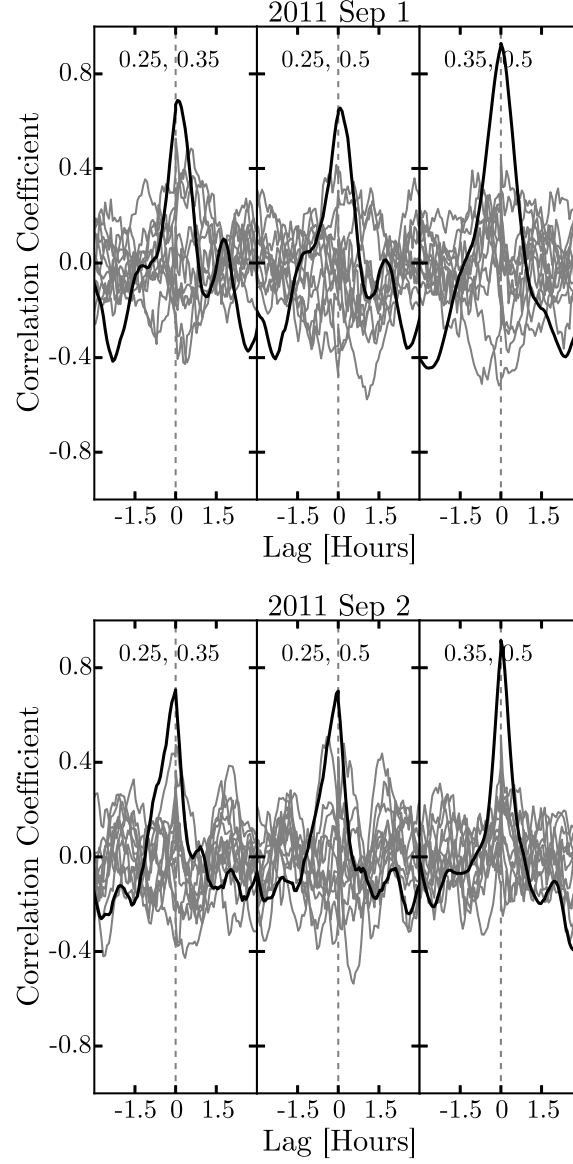


Figure 5.4: Cross correlations for all three pairs of SPIRE bands for Sgr A* (black line) and reference locations (gray lines). Left: data from the first observing interval. Right: data from the second observing interval. In each panel, the left column shows the cross-correlation of the 0.25 mm light curve with the 0.35 mm light curve, the middle column shows the cross-correlation of the 0.25 mm light curve with the 0.5 mm light curve, and the right column shows the cross-correlation of the 0.35 mm light curve and the 0.5 mm light curve.

5.4 Discussion

We observe strong variations in all three SPIRE bands with similar amplitude in each. We do not know the absolute flux density of Sgr A* at any of these wavelengths due to confusion with the surrounding dust emission (though interferometer measurements at 0.43 mm in Marrone et al. (2006) show a minimum flux density of 2 Jy in 4 epochs). However, the negative deviation around 5 UT in the first interval implies that for all three bands there must be a minimum time-averaged flux density of at least 0.5 Jy even at 0.25 mm, where the SED is not presently constrained.

We quantify the distribution of flux density variations in Sgr A* at submillimeter wavelengths in Figure 5.5. Using the SPIRE light curves, as well as the ~ 70 h of 1.3 mm light curves compiled by Dexter et al. (2014), we determine most-likely variability amplitudes for 4-hour subsets of the data at each wavelength and compile them into a distribution function. This segmentation time is chosen to span typical variations in the light curves, though our results are not very sensitive to the choice. Explicitly, for each four-hour block, we binned the data to 20-minute time resolution for better signal-to-noise, subtracted the bin mean, and then constructed the function

$$P_{\text{block}}(\sigma|f_i, \delta_i) = \Pi_i\left(\frac{1}{\sqrt{2\pi}(\sigma^2 + \delta_i^2)}\right)e^{\left(\frac{-f_i^2}{2(\sigma^2 + \delta_i^2)}\right)}, \quad (5.4)$$

for the probability that a given σ is the actual width of the underlying random process, given the binned mean-subtracted flux densities in the block f_i , and their uncertainties δ_i . By taking the most likely variability amplitude from each block, we can create a single cumulative distribution function (CDF) for each band. In order to illustrate the range of possible CDFs that are consistent with our data, we numerically sample the probability function for each block 100 times to create 100 additional CDFs. Figure 5.5 shows the central 68 CDFs created in this way.

The CDFs for the SPIRE bands exhibit a trend toward lower absolute variability amplitude with shorter wavelength. Numerical simulations predict constant or increasing fractional variability with decreasing wavelength in this portion of the Sgr A* SED (e.g., Goldston et al., 2005; Dexter and Fragile, 2013; Chan et al., 2015), which, combined with the larger variability amplitude at 0.5 mm, suggests that the

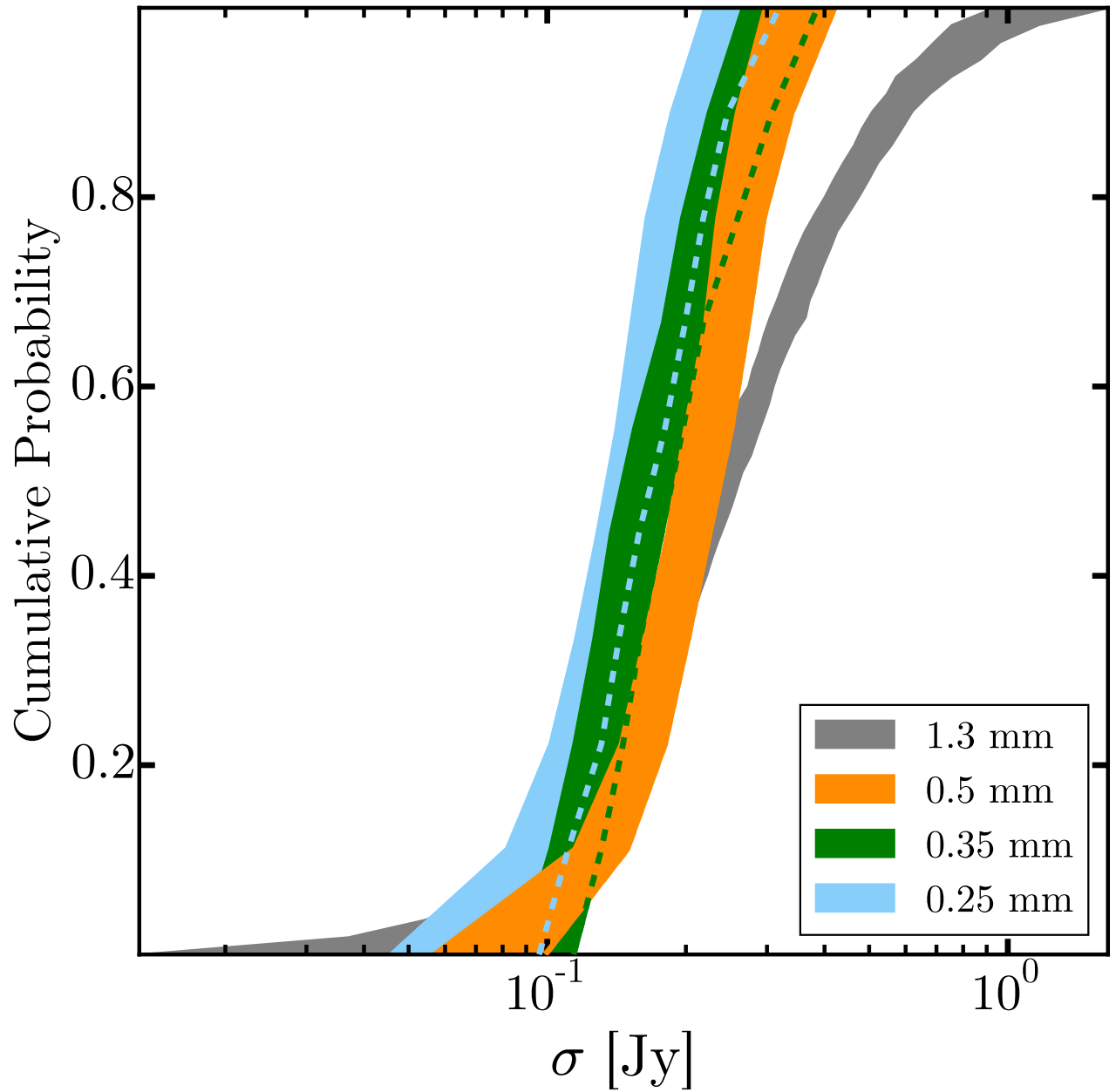


Figure 5.5: Cumulative distribution of variability amplitude in overlapping 3-hour blocks. The width of each swath contains the central 68% of CDFs for each light curve, generated by sampling the likelihood function of σ for each 4-hour block. (See text for details.) Where obscured, dashed lines indicate the edge of each swath.

SED is falling from 0.5 to 0.25 mm. This is consistent with expectations based on increasingly optically thin emission toward shorter wavelength.

The distribution of 1.3 mm variability is notably different from the SPIRE curves in Figure 5.5. There is a long tail of high-amplitude variations not seen in the submillimeter light curves. This may be the result of catching Sgr A* during a quiet state, as past ground-based measurements of Sgr A* in the 0.45 and 0.35 mm atmospheric windows differed by several Jy (Dent et al., 1993; Serabyn et al., 1997; Pierce-Price et al., 2000; Yusef-Zadeh et al., 2006; Marrone et al., 2006, 2008). A quiet state is also suggested by the *XMM-Newton* light curves shown in Figures 5.2 and 5.3, which show no flare event with a 2-10 keV luminosity greater than 1.8×10^{34} erg s⁻¹. The absence of a larger flare in our X-ray light curves is consistent with the flare rate inferred from more than 800 hours of *Chandra* monitoring of Sgr A* (~ 1 day⁻¹ above 10^{34} erg s⁻¹; Neilsen et al., 2013). The 1.3 mm light curve has a duration nearly three times that of the SPIRE light curve, and also extends over many years and therefore includes more of the long term fluctuations that can be expected from AGN variability.

Our SPIRE light curves reveal interesting color changes. In Figure 5.6 we again plot the SPIRE light curves, but now show how the 0.5–0.35 mm flux density difference changes with time. In the first interval, we see a red color following our largest observed feature, from 05:00 to 08:00 UT. Notably, the flare falls off even faster at 0.25 mm than it does at 0.35 or 0.5 mm. The reddened color as flux density decreases is suggestive of a cooling process. The expanding-blob model for features in the submillimeter light curve of Sgr A* should exhibit a blue-first fall off in flux reminiscent of what we observe, yet the simultaneous rise at all wavelengths is not consistent with the most naive blob models. It is somewhat harder to predict how color changes should manifest in more complex occultation models where both absorption and adiabatic expansion take place simultaneously (Yusef-Zadeh et al., 2010).

During our second observing interval, the light curves exhibit a clear pattern of relatively red local maxima, and relatively blue local minima. This pattern indicates

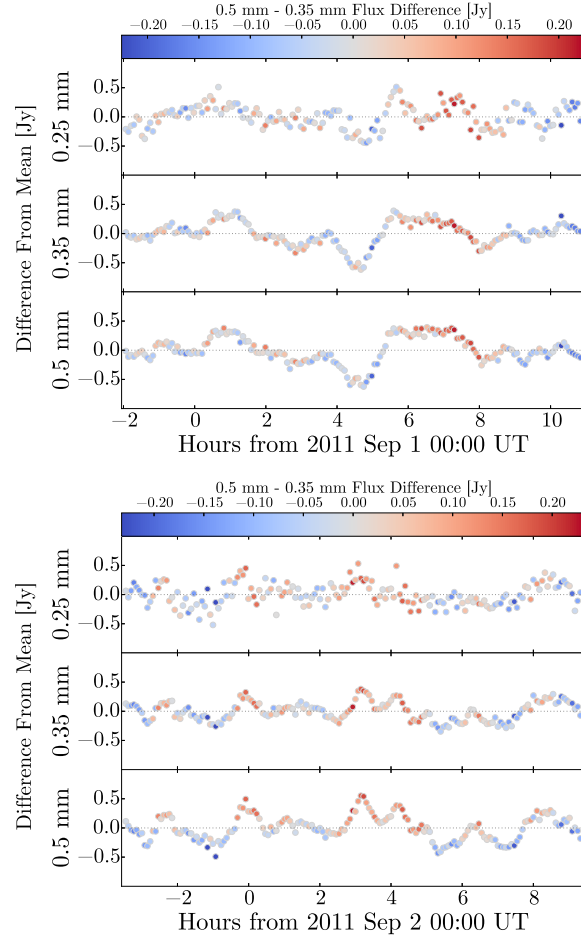


Figure 5.6: SPIRE light curves with flux density measurements color-coded to show the 0.5 mm - 0.35 mm flux density difference. The left panel shows the light curves from the first interval and the right panel shows the light curves from the second interval.

a larger absolute amplitude of variation for the longer-wavelength band. This pattern is less evident in the first interval, though there is some hint of a similar pattern in the smaller flares and the largest flare is brightest at 0.5 mm for most of its duration. This seeming change in the spectrum of the flaring emission between the first and second intervals may indicate that the quiescent 0.5–0.25 mm spectrum also changed, but without a way to directly measure the absolute flux density of Sgr A* we can only speculate.

In Figure 5.7 we show the power spectrum of our 0.5 mm light curve. The power spectrum is computed using Welch’s method (Welch, 1967), dividing into 6-hour blocks with 66% overlap. For clarity, we do not show the 0.25 mm and 0.35 mm power spectra, but they are very similar to the 0.5 mm spectrum, as would be expected from the similarity of the light curves. We find consistent power spectra between the two observing intervals, with power law slopes that agree to within 0.1. Specifically, for $P \propto f^{-\beta}$ we find $\beta = 2.2 \pm 0.2$. This is very similar to the $\beta = 2.3^{+0.8}_{-0.6}$ measured at 1.3 mm by Dexter et al. (2014). Those authors also noted a break in the power spectrum at 8^{+3}_{-4} hours, which is a longer timescale than we have access to in our 12.5-hour intervals. Meyer et al. (2009) also found a slope of $\beta = 2.1 \pm 0.5$ at infrared wavelengths (mostly 2.2 μm), but with a spectral break around 2.5 hours. There is only a slight suggestion of a break in our data around 0.4 h^{-1} , but the data provide very few independent measurements of this portion of the power spectrum and so we cannot consider this significant. The consistency in slope from 1.3 mm, through the SPIRE bands, out to the IR is not unexpected, as emission at all of these wavelengths is expected to arise very close to the black hole, and therefore to be subject to the same variations in the accretion process.

5.5 Conclusions

In this work we have presented the longest continuous submillimeter observations of Sgr A*, using 25.5 hours of data from the SPIRE instrument aboard the *Herschel Space Observatory*. These data have provided a first lower bound on the SED of Sgr A* at 0.25 mm and characterized the wavelength and temporal spectra of

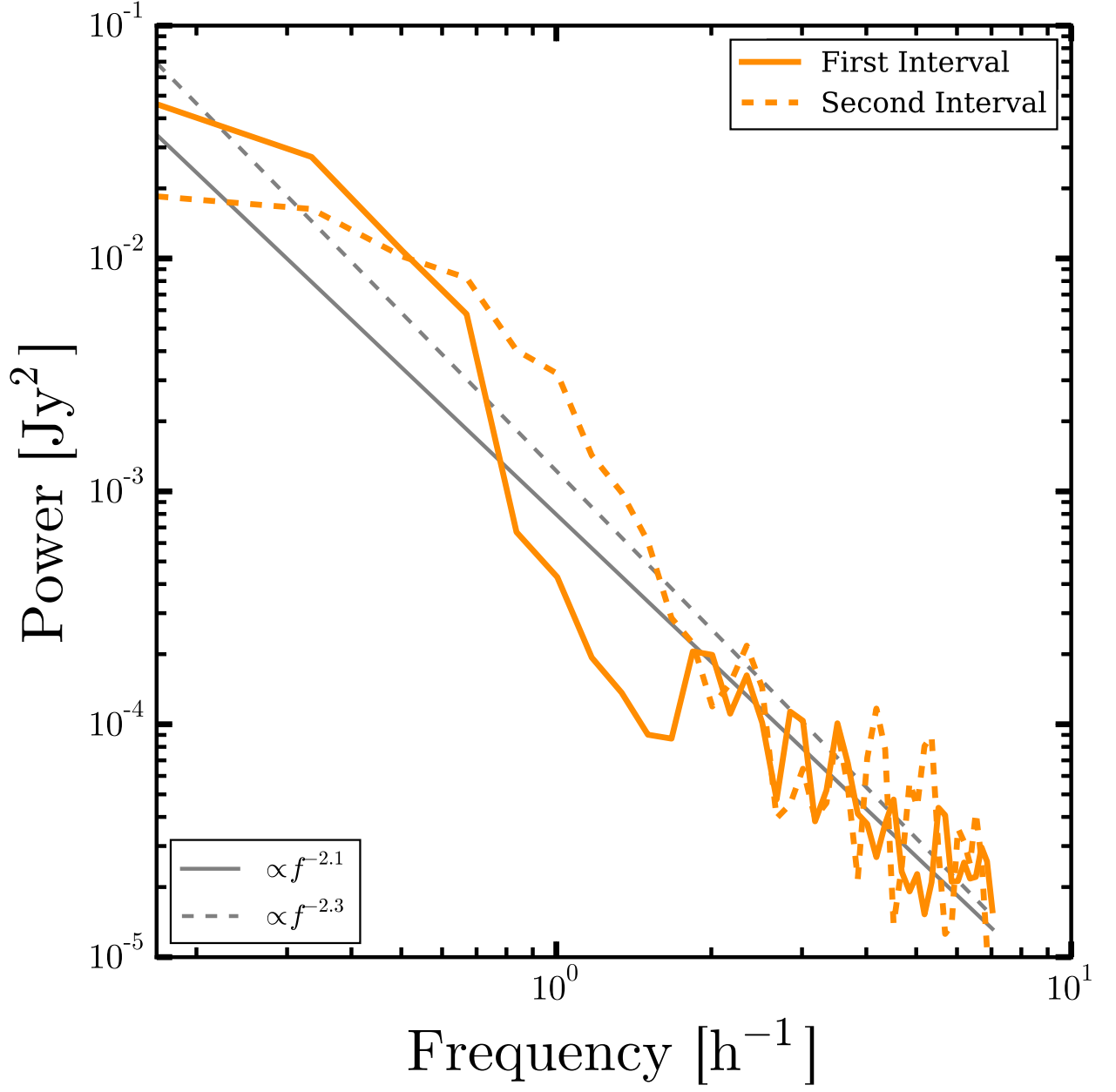


Figure 5.7: Power spectra for 0.5 mm light curves from the first and second observing intervals, along with best fit power-laws. The power spectra of the 0.25 mm and 0.35 mm light-curve are similar, though less well determined.

its submillimeter variations. While *Herschel* is no longer operational, the Atacama Large Millimeter/Submillimeter Array (ALMA) can make ground-based measurements from 3 to 0.35 mm at high sensitivity, which can provide further constraints at similar wavelengths. In particular, the spatial resolution afforded by ALMA will be adequate to isolate Sgr A* from its surroundings, which was not possible with *Herschel*. Such data can more fully characterize the SED of this source and its fractional variability.

CHAPTER 6

Conclusions

6.1 Variable accretion processes in the young binary-star system UY Aur

I helped commission the echelle mode of the ARIES spectrograph behind the MMT adaptive optics system. My spectra show the first ever detection of H_2 emission for UY Aur A and demonstrate a trend when compared to previous lower-resolution spectra of increasing accretion activity in UY Aur A and decreasing activity in UY Aur B. Different accretion indicators, such as K-band disk luminosity and $\text{Br}\gamma$ line luminosity, disagree on whether UY Aur B is currently less active. I suggested two scenarios which could explain these observations: first, that material accreting through the disk and producing a warmer more luminous disk, is piling up at some inner radius and not making it onto the star, where shocks produce $\text{Br}\gamma$ emission; second, I showed how it is reasonable that increased accretion through the disk could increase the scale height of the disk enough to add significant extinction to the surface of the protostar. In the second scenario, the intrinsic $\text{Br}\gamma$ flux is actually increased, even though the observed flux has decreased. These scenarios are testable and future work should include spectroscopic and photometric monitoring of edge-on and nearly edge-on protoplanetary systems to see if the predicted anti-correlation of disk-flux and $\text{Br}\gamma$ flux is present.

6.2 L-band Spectroscopy with Magellan-AO/Clio2: First Results on Young Low-Mass Companions

L-band spectroscopy of directly imaged companions to nearby young stars is important for fully characterizing their atmospheres and constraining their formation mechanism. I presented the first L-band spectra from Clio2 behind the Magellan adaptive optics system, currently the only low-resolution L-band spectrograph in the Southern

Hemisphere. Directly imaged planets with effective temperatures ~ 1000 K exhibit peculiar L-band SEDs when compared to more massive brown dwarfs in the field, even at the same temperature. My sample of warmer more massive ($12\text{--}30 M_{\text{Jup}}$) companions to nearby young stars have L-band spectra that are consistent with older even more massive brown dwarfs at the same temperature. These observations constrain the temperature range where the L-band SEDs of directly imaged companions begin to appear distinct from higher-gravity field dwarfs to be between 1000 and 1500 K. This range is consistent with the L-T transition for field dwarfs, emphasizing that the difference in appearance is due to clouds and carbon chemistry, which both evolve rapidly in the L-T transition. A few of my targets did exhibit some peculiarities. First, CD-35 2722 B has a $3\text{--}4 \mu\text{m}$ spectral slope that is redder than field dwarfs, implying less opaque cloud structure in this source and suggesting some cloud evolution occurs on ~ 50 My timescales. Second, AB Pic b and 2M 0103(AB) b both exhibit higher than expected flux at wavelengths corresponding to the fundamental ro-vibrational bands of the methane molecule. More work needs to be done to fully verify and characterize this feature, but if physical it could imply an atmospheric inversion or fluorescence in an aurora.

The future is bright for the study of low-mass companions to nearby stars. Two powerful new instruments have recently begun operation in the Southern Hemisphere: the Gemini Planet Imager (Macintosh et al., 2006); and the VLT Spectro-Polarimetric High-contrast Exoplanet REsearch (Beuzit et al., 2008). Both are designed to discover and characterize new gas-giant extrasolar planets, both include powerful adaptive optics systems, coronagraphs, and integral field spectrographs to provide spectroscopic characterization at high-contrast. Both instruments are sensitive in the NIR, from y to K bands. These instruments will undoubtedly image newly discovered planets and provide initial probes of their atmospheres. A more robust and diverse set of directly imaged planets will be essential for honing atmospheric models and improving our understanding of the most important processes in young gas-giant atmospheres.

Early studies of the first directly imaged extrasolar planets have revealed that the

L-band is a particularly powerful and important spectral regime for characterizing planetary atmospheres because 3–4 μm spectra can be used to constrain cloudiness and disequilibrium chemistry. Thus, longer wavelength follow-up of GPI and SPHERE discoveries will be important to constrain their atmospheric properties.

The new Arizona Lenslets for Exoplanet Spectroscopy (ALES) upgrade to the Large Binocular Telescope L/M-band mid-InfraRed Camera (LBTI/LMIRCam; Hinz et al., 2004; Wilson et al., 2008) provides the first integral field spectrograph (IFS) that can deliver low-resolution L and M band spectroscopy of directly imaged planets. IFSs are powerful instruments for studying the atmospheres of extrasolar planets because high contrast imaging techniques, such as angular differential imaging, can be used to help separate the light of planets from their host stars.

Combining GPI or SPHERE spectra with ALES spectra of extrasolar planets will result in spectral coverage from $\sim 1\text{--}4\ \mu\text{m}$. Such broad wavelength coverage strongly constrains the physics of the planetary atmospheres and can help break degeneracies in modeling extrasolar planet atmospheres (Sekemer et al., submitted).

6.3 Disentangling Confused Stars at the Galactic Center with Long Baseline Infrared Interferometry

I modeled observations of stars at the galactic center with the Keck-Interferometer ASTRA and Very Large Telescope Interferometer GRAVITY instruments. These large-aperture infrared interferometers gain the necessary sensitivity to make such observations by employing dual-field phase referencing. I showed the Keck Interferometer was better positioned if the stellar content within 50 milliarcseconds of Sgr A* only includes faint sources, because of better throughput and less beamsplits. The GRAVITY instrument will excel if the source content includes a few bright sources, since it is less affected by confusion noise because of the significant uv-coverage provided by the interferometer. Though the Keck Interferometer has been shutdown, construction of the GRAVITY instrument continues. Future observations with GRAVITY will discover new stars closer to Sgr A* if any exist with a K-band magnitude less than ~ 20 .

6.4 Far Infrared Variability of Sagittarius A*: 25.5 hours of Monitoring with *Herschel*

I used 25.5 hours of *Herschel* SPIRE observations to construct light curves of Sgr A* at wavelengths that are difficult or impossible to observe from the ground. The variations I report represent less than 1% of the flux in the *Herschel* beam at the location of Sgr A* and are supported by overlapping ground-based observations. The data I present provide the only constraint on the 0.25 mm flux of Sgr A*, setting a 0.5 Jy lower limit on the quiescent flux in this band. I show that the variability characteristics at submillimeter wavelengths are distinct when compared to 1.3 mm light curves, lacking a contribution from large amplitude variations. I suggest that the lack of a tail in my submillimeter light curves could suggest a physical connection between submillimeter variations and X-ray flares, which did not occur during our observing intervals. Such a connection is not well established. Future ALMA monitoring at 0.45 and 0.35 mm will establish the absolute flux level of Sgr A* at these wavelengths.

The inner-regions of the accretion flow will be probed by future interferometric observations of Sgr A*. In the NIR, the GRAVITY instrument can perform precise astrometry on bright NIR flares and could reveal orbital motion of a hot spot in a disk. At 1.3 mm, the Event Horizon Telescope, is a very-long baseline interferometry experiment that will combine stations across the globe to deliver the highest spatial resolution measurements of Sgr A*. These observations hold the potential to detect the signature of the black hole event horizon on the innermost regions of the accretion flow, providing a powerful test of general relativity in the strong-field regime.

REFERENCES

- Akeson, R. L. and E. L. N. Jensen (2014). Circumstellar Disks around Binary Stars in Taurus. *ApJ*, **784**, 62. doi:10.1088/0004-637X/784/1/62.
- Allard, F., D. Homeier, B. Freytag, and C. M. Sharp (2012). Atmospheres From Very Low-Mass Stars to Extrasolar Planets. In Reyl  , C., C. Charbonnel, and M. Schultheis (eds.) *EAS Publications Series*, volume 57 of *EAS Publications Series*, pp. 3–43. doi:10.1051/eas/1257001.
- An, T., W. M. Goss, J.-H. Zhao, X. Y. Hong, S. Roy, A. P. Rao, and Z.-Q. Shen (2005). Simultaneous Multiwavelength Observations of Sagittarius A*. *ApJ*, **634**, pp. L49–L52. doi:10.1086/498687.
- Armitage, P. J. (2011). Dynamics of Protoplanetary Disks. *ARA&A*, **49**, pp. 195–236. doi:10.1146/annurev-astro-081710-102521.
- Artymowicz, P. and S. H. Lubow (1996). Mass Flow through Gaps in Circumbinary Disks. *ApJ*, **467**, p. L77. doi:10.1086/310200.
- Baganoff, F. K., M. W. Bautz, W. N. Brandt, G. Chartas, E. D. Feigelson, G. P. Garmire, Y. Maeda, M. Morris, G. R. Ricker, L. K. Townsley, and F. Walter (2001). Rapid X-ray flaring from the direction of the supermassive black hole at the Galactic Centre. *Nature*, **413**, pp. 45–48. doi:10.1038/35092510.
- Baganoff, F. K., Y. Maeda, M. Morris, M. W. Bautz, W. N. Brandt, W. Cui, J. P. Doty, E. D. Feigelson, G. P. Garmire, S. H. Pravdo, G. R. Ricker, and L. K. Townsley (2003). Chandra X-Ray Spectroscopic Imaging of Sagittarius A* and the Central Parsec of the Galaxy. *ApJ*, **591**, pp. 891–915. doi:10.1086/375145.
- Balbus, S. A. and J. F. Hawley (1991). A powerful local shear instability in weakly magnetized disks. I - Linear analysis. II - Nonlinear evolution. *ApJ*, **376**, pp. 214–233. doi:10.1086/170270.
- Balick, B. and R. L. Brown (1974). Intense sub-arcsecond structure in the galactic center. *ApJ*, **194**, pp. 265–270. doi:10.1086/153242.
- Baraffe, I., D. Homeier, F. Allard, and G. Chabrier (2015). New evolutionary models for pre-main sequence and main sequence low-mass stars down to the hydrogen-burning limit. *A&A*, **577**, A42. doi:10.1051/0004-6361/201425481.
- Barman, T. S., B. Macintosh, Q. M. Konopacky, and C. Marois (2011a). Clouds and Chemistry in the Atmosphere of Extrasolar Planet HR8799b. *ApJ*, **733**, 65. doi:10.1088/0004-637X/733/1/65.

- Barman, T. S., B. Macintosh, Q. M. Konopacky, and C. Marois (2011b). The Young Planet-mass Object 2M1207b: A Cool, Cloudy, and Methane-poor Atmosphere. *ApJ*, **735**, L39. doi:10.1088/2041-8205/735/2/L39.
- Bate, M. R. and I. A. Bonnell (1997). Accretion during binary star formation - II. Gaseous accretion and disc formation. *MNRAS*, **285**, pp. 33–48.
- Beck, T. L., J. S. Bary, A. Dutrey, V. Piétu, S. Guilloteau, S. H. Lubow, and M. Simon (2012). Circumbinary Gas Accretion onto a Central Binary: Infrared Molecular Hydrogen Emission from GG Tau A. *ApJ*, **754**, 72. doi:10.1088/0004-637X/754/1/72.
- Beck, T. L., P. J. McGregor, M. Takami, and T.-S. Pyo (2008). Spatially Resolved Molecular Hydrogen Emission in the Inner 200 AU Environments of Classical T Tauri Stars. *ApJ*, **676**, pp. 472–489. doi:10.1086/527528.
- Bergin, E. A. and M. Tafalla (2007). Cold Dark Clouds: The Initial Conditions for Star Formation. *ARA&A*, **45**, pp. 339–396. doi:10.1146/annurev.astro.45.071206.100404.
- Beuzit, J.-L., M. Feldt, K. Dohlen, D. Mouillet, P. Puget, F. Wildi, L. Abe, J. Antichi, A. Baruffolo, P. Baudoz, A. Boccaletti, M. Carbillet, J. Charton, R. Claudi, M. Downing, C. Fabron, P. Feautrier, E. Fedrigo, T. Fusco, J.-L. Gach, R. Gratton, T. Henning, N. Hubin, F. Joos, M. Kasper, M. Langlois, R. Lenzen, C. Moutou, A. Pavlov, C. Petit, J. Pragt, P. Rabou, F. Rigal, R. Roelfsema, G. Rousset, M. Saisse, H.-M. Schmid, E. Stadler, C. Thalmann, M. Turatto, S. Udry, F. Vakili, and R. Waters (2008). SPHERE: a 'Planet Finder' instrument for the VLT. In *Society of Photo-Optical Instrumentation Engineers (SPIE) Conference Series*, volume 7014 of *Society of Photo-Optical Instrumentation Engineers (SPIE) Conference Series*, p. 18. doi:10.1117/12.790120.
- Black, J. H. and E. F. van Dishoeck (1987). Fluorescent excitation of interstellar H₂. *ApJ*, **322**, pp. 412–449. doi:10.1086/165740.
- Blum, J. and G. Wurm (2008). The Growth Mechanisms of Macroscopic Bodies in Protoplanetary Disks. *ARA&A*, **46**, pp. 21–56. doi:10.1146/annurev.astro.46.060407.145152.
- Boley, A. C., R. Helled, and M. J. Payne (2011). The Heavy-element Composition of Disk Instability Planets Can Range from Sub- to Super-nebular. *ApJ*, **735**, 30. doi:10.1088/0004-637X/735/1/30.
- Bonnefoy, M., G. Chauvin, A.-M. Lagrange, P. Rojo, F. Allard, C. Pinte, C. Dumas, and D. Homeier (2014). A library of near-infrared integral field spectra of young M-L dwarfs. *A&A*, **562**, A127. doi:10.1051/0004-6361/201118270.

- Bonnefoy, M., G. Chauvin, P. Rojo, F. Allard, A.-M. Lagrange, D. Homeier, C. Dumas, and J.-L. Beuzit (2010). Near-infrared integral-field spectra of the planet/brown dwarf companion AB Pictoris b. *A&A*, **512**, A52. doi:10.1051/0004-6361/200912688.
- Boss, A. P. (1997). Giant planet formation by gravitational instability. *Science*, **276**, pp. 1836–1839. doi:10.1126/science.276.5320.1836.
- Bower, G. C., S. Markoff, J. Dexter, M. A. Gurwell, J. M. Moran, A. Brunthaler, H. Falcke, P. C. Fragile, D. Maitra, D. Marrone, A. Peck, A. Rushton, and M. C. H. Wright (2015). Radio and Millimeter Monitoring of Sgr A*: Spectrum, Variability, and Constraints on the G2 Encounter. *ApJ*, **802**, 69. doi:10.1088/0004-637X/802/1/69.
- Bowler, B. P., M. C. Liu, T. J. Dupuy, and M. C. Cushing (2010). Near-infrared Spectroscopy of the Extrasolar Planet HR 8799 b. *ApJ*, **723**, pp. 850–868. doi:10.1088/0004-637X/723/1/850.
- Brandeker, A., R. Jayawardhana, and J. Najita (2003). Keck Adaptive Optics Imaging of Nearby Young Stars: Detection of Close Multiple Systems. *AJ*, **126**, pp. 2009–2014. doi:10.1086/378057.
- Brannigan, E., M. Takami, A. Chrysostomou, and J. Bailey (2006). On the detection of artefacts in spectro-astrometry. *MNRAS*, **367**, pp. 315–322. doi:10.1111/j.1365-2966.2005.09942.x.
- Brinkerink, C. D., H. Falcke, C. J. Law, D. Barkats, G. C. Bower, A. Brunthaler, C. Gammie, C. M. V. Impellizzeri, S. Markoff, K. M. Menten, M. Moscibrodzka, A. Peck, A. P. Rushton, R. Schaaf, and M. Wright (2015). ALMA and VLA measurements of frequency-dependent time lags in Sagittarius A*: evidence for a relativistic outflow. *A&A*, **576**, A41. doi:10.1051/0004-6361/201424783.
- Brown, R. H., K. H. Baines, G. Bellucci, J.-P. Bibring, B. J. Buratti, F. Capaccioni, P. Cerroni, R. N. Clark, A. Coradini, D. P. Cruikshank, P. Drossart, V. Formisano, R. Jaumann, Y. Langevin, D. L. Matson, T. B. McCord, V. Mennella, R. M. Nelson, P. D. Nicholson, B. Sicardy, C. Sotin, S. Amici, M. A. Chamberlain, G. Filacchione, G. Hansen, K. Hibbitts, and M. Showalter (2003). Observations with the Visual and Infrared Mapping Spectrometer (VIMS) during Cassini’s flyby of Jupiter. *Icarus*, **164**, pp. 461–470. doi:10.1016/S0019-1035(03)00134-9.
- Chan, C.-k., D. Psaltis, F. Ozel, L. Medeiros, D. Marrone, A. Sadowski, and R. Narayan (2015). Fast Variability and mm/IR flares in GRMHD Models of Sgr A* from Strong-Field Gravitational Lensing. *ArXiv e-prints*.

- Chapman, S. and T. G. Cowling (1970). *The mathematical theory of non-uniform gases. an account of the kinetic theory of viscosity, thermal conduction and diffusion in gases.*
- Chauvin, G., A.-M. Lagrange, C. Dumas, B. Zuckerman, D. Mouillet, I. Song, J.-L. Beuzit, and P. Lowrance (2004). A giant planet candidate near a young brown dwarf. Direct VLT/NACO observations using IR wavefront sensing. *A&A*, **425**, pp. L29–L32. doi:10.1051/0004-6361:200400056.
- Chauvin, G., A.-M. Lagrange, B. Zuckerman, C. Dumas, D. Mouillet, I. Song, J.-L. Beuzit, P. Lowrance, and M. S. Bessell (2005). A companion to AB Pic at the planet/brown dwarf boundary. *A&A*, **438**, pp. L29–L32. doi:10.1051/0004-6361:200500111.
- Chiang, E. and G. Laughlin (2013). The minimum-mass extrasolar nebula: in situ formation of close-in super-Earths. *MNRAS*, **431**, pp. 3444–3455. doi:10.1093/mnras/stt424.
- Close, L. M., A. Dutrey, F. Roddier, S. Guilloteau, C. Roddier, M. Northcott, F. Menard, G. Duvert, J. E. Graves, and D. Potter (1998). Adaptive Optics Imaging of the Circumbinary Disk around the T Tauri Binary UY Aurigae: Estimates of the Binary Mass and Circumbinary Dust Grain Size Distribution. *ApJ*, **499**, p. 883. doi:10.1086/305672.
- Close, L. M., J. R. Males, K. Morzinski, D. Kopon, K. Follette, T. J. Rodigas, P. Hinz, Y.-L. Wu, A. Puglisi, S. Esposito, A. Riccardi, E. Pinna, M. Xompero, R. Briguglio, A. Uomoto, and T. Hare (2013). Diffraction-limited Visible Light Images of Orion Trapezium Cluster with the Magellan Adaptive Secondary Adaptive Optics System (MagAO). *ApJ*, **774**, 94. doi:10.1088/0004-637X/774/2/94.
- Colavita, M. M. (1999). Fringe Visibility Estimators for the Palomar Testbed Interferometer. *PASP*, **111**, pp. 111–117. doi:10.1086/316302.
- Colavita, M. M. (2009). Adverse effects in dual-feed interferometry. *New A Rev.*, **53**, pp. 344–352. doi:10.1016/j.newar.2010.07.004.
- Currie, T., A. Burrows, Y. Itoh, S. Matsumura, M. Fukagawa, D. Apai, N. Madhusudhan, P. M. Hinz, T. J. Rodigas, M. Kasper, T.-S. Pyo, and S. Ogino (2011). A Combined Subaru/VLT/MMT 1-5 μm Study of Planets Orbiting HR 8799: Implications for Atmospheric Properties, Masses, and Formation. *ApJ*, **729**, 128. doi:10.1088/0004-637X/729/2/128.
- Cushing, M. C., M. S. Marley, D. Saumon, B. C. Kelly, W. D. Vacca, J. T. Rayner, R. S. Freedman, K. Lodders, and T. L. Roellig (2008). Atmospheric Parameters of Field L and T Dwarfs. *ApJ*, **678**, pp. 1372–1395. doi:10.1086/526489.

- Cushing, M. C., J. T. Rayner, and W. D. Vacca (2005). An Infrared Spectroscopic Sequence of M, L, and T Dwarfs. *ApJ*, **623**, pp. 1115–1140. doi:10.1086/428040.
- de Bruyn, A. G. (1976). Radio spectra of non-uniform synchrotron sources with internal absorption. *A&A*, **52**, pp. 439–447.
- Delorme, P., J. Gagné, J. H. Girard, A. M. Lagrange, G. Chauvin, M.-E. Naud, D. Lafrenière, R. Doyon, A. Riedel, M. Bonnefoy, and L. Malo (2013). Direct-imaging discovery of a 12-14 Jupiter-mass object orbiting a young binary system of very low-mass stars. *A&A*, **553**, L5. doi:10.1051/0004-6361/201321169.
- Dent, W. R. F., H. E. Matthews, R. Wade, and W. D. Duncan (1993). Sub-millimeter continuum emission from the Galactic center region. *ApJ*, **410**, pp. 650–662. doi:10.1086/172781.
- Dexter, J., E. Agol, P. C. Fragile, and J. C. McKinney (2010). The Submillimeter Bump in Sgr A* from Relativistic MHD Simulations. *ApJ*, **717**, pp. 1092–1104. doi:10.1088/0004-637X/717/2/1092.
- Dexter, J. and P. C. Fragile (2013). Tilted black hole accretion disc models of Sagittarius A*: time-variable millimetre to near-infrared emission. *MNRAS*, **432**, pp. 2252–2272. doi:10.1093/mnras/stt583.
- Dexter, J., B. Kelly, G. C. Bower, D. P. Marrone, J. Stone, and R. Plambeck (2014). An 8 h characteristic time-scale in submillimetre light curves of Sagittarius A*. *MNRAS*, **442**, pp. 2797–2808. doi:10.1093/mnras/stu1039.
- Do, T., A. M. Ghez, M. R. Morris, J. R. Lu, K. Matthews, S. Yelda, and J. Larkin (2009a). High Angular Resolution Integral-Field Spectroscopy of the Galaxy’s Nuclear Cluster: A Missing Stellar Cusp? *ApJ*, **703**, pp. 1323–1337. doi:10.1088/0004-637X/703/2/1323.
- Do, T., A. M. Ghez, M. R. Morris, S. Yelda, L. Meyer, J. R. Lu, S. D. Hornstein, and K. Matthews (2009b). A Near-Infrared Variability Study of the Galactic Black Hole: A Red Noise Source with NO Detected Periodicity. *ApJ*, **691**, pp. 1021–1034. doi:10.1088/0004-637X/691/2/1021.
- Dodds-Eden, K., S. Gillessen, T. K. Fritz, F. Eisenhauer, S. Trippe, R. Genzel, T. Ott, H. Bartko, O. Pfuhl, G. Bower, A. Goldwurm, D. Porquet, G. Trap, and F. Yusef-Zadeh (2011). The Two States of Sgr A* in the Near-infrared: Bright Episodic Flares on Top of Low-level Continuous Variability. *ApJ*, **728**, 37. doi:10.1088/0004-637X/728/1/37.

- Dodds-Eden, K., D. Porquet, G. Trap, E. Quataert, X. Haubois, S. Gillessen, N. Grosso, E. Pantin, H. Falcke, D. Rouan, R. Genzel, G. Hasinger, A. Goldwurm, F. Yusef-Zadeh, Y. Clenet, S. Trippe, P.-O. Lagage, H. Bartko, F. Eisenhauer, T. Ott, T. Paumard, G. Perrin, F. Yuan, T. K. Fritz, and L. Mascetti (2009). Evidence for X-Ray Synchrotron Emission from Simultaneous Mid-Infrared to X-Ray Observations of a Strong Sgr A* Flare. *ApJ*, **698**, pp. 676–692. doi:10.1088/0004-637X/698/1/676.
- Dodds-Eden, K., P. Sharma, E. Quataert, R. Genzel, S. Gillessen, F. Eisenhauer, and D. Porquet (2010). Time-Dependent Models of Flares from Sagittarius A*. *ApJ*, **725**, pp. 450–465. doi:10.1088/0004-637X/725/1/450.
- Doeleman, S. S., J. Weintroub, A. E. E. Rogers, R. Plambeck, R. Freund, R. P. J. Tilanus, P. Friberg, L. M. Ziurys, J. M. Moran, B. Corey, K. H. Young, D. L. Smythe, M. Titus, D. P. Marrone, R. J. Cappallo, D. C.-J. Bock, G. C. Bower, R. Chamberlin, G. R. Davis, T. P. Krichbaum, J. Lamb, H. Maness, A. E. Niell, A. Roy, P. Strittmatter, D. Werthimer, A. R. Whitney, and D. Woody (2008). Event-horizon-scale structure in the supermassive black hole candidate at the Galactic Centre. *Nature*, **455**, pp. 78–80. doi:10.1038/nature07245.
- Duchêne, G. (1999). Binary fraction in low-mass star forming regions: a reexamination of the possible excesses and implications. *A&A*, **341**, pp. 547–552.
- Duchêne, G. and A. Kraus (2013). Stellar Multiplicity. *ARA&A*, **51**, pp. 269–310. doi:10.1146/annurev-astro-081710-102602.
- Dutrey, A., S. Guilloteau, G. Duvert, L. Prato, M. Simon, K. Schuster, and F. Menard (1996). Dust and gas distribution around T Tauri stars in Taurus-Auriga. I. Interferometric 2.7mm continuum and ^{13}CO J=1-0 observations. *A&A*, **309**, pp. 493–504.
- Duvert, G., A. Dutrey, S. Guilloteau, F. Menard, K. Schuster, L. Prato, and M. Simon (1998). Disks in the UY Aurigae binary. *A&A*, **332**, pp. 867–874.
- Eckart, A., F. K. Baganoff, M. Morris, M. W. Bautz, W. N. Brandt, G. P. Garmire, R. Genzel, T. Ott, G. R. Ricker, C. Straubmeier, T. Viehmann, R. Schödel, G. C. Bower, and J. E. Goldston (2004). First simultaneous NIR/X-ray detection of a flare from Sgr A*. *A&A*, **427**, pp. 1–11. doi:10.1051/0004-6361:20040495.
- Eckart, A., F. K. Baganoff, M. R. Morris, D. Kunneriath, M. Zamaninasab, G. Witzel, R. Schödel, M. García-Marín, L. Meyer, G. C. Bower, D. Marrone, M. W. Bautz, W. N. Brandt, G. P. Garmire, G. R. Ricker, C. Straubmeier, D. A. Roberts, K. Muzic, J. Mauerhan, and A. Zensus (2009). Modeling mm-to X-ray flare emission from Sagittarius A*. *A&A*, **500**, pp. 935–946. doi:10.1051/0004-6361/200811354.

- Eckart, A., M. García-Marín, S. N. Vogel, P. Teuben, M. R. Morris, F. Baganoff, J. Dexter, R. Schödel, G. Witzel, M. Valencia-S., V. Karas, D. Kunneriath, C. Straubmeier, L. Moser, N. Sabha, R. Buchholz, M. Zamaninasab, K. Mužić, J. Moutaka, and J. A. Zensus (2012). Millimeter to X-ray flares from Sagittarius A*. *A&A*, **537**, A52. doi:10.1051/0004-6361/201117779.
- Eckart, A., R. Genzel, A. Krabbe, R. Hofmann, P. P. van der Werf, and S. Drapatz (1992). Spatially resolved near-infrared emission and a bubble of hot gas in the central active region of the Galaxy. *Nature*, **355**, pp. 526–529. doi:10.1038/355526a0.
- Eckart, A., R. Schödel, M. García-Marín, G. Witzel, A. Weiss, F. K. Baganoff, M. R. Morris, T. Bertram, M. Dovčiak, W. J. Duschl, V. Karas, S. König, T. P. Krichbaum, M. Krips, D. Kunneriath, R.-S. Lu, S. Markoff, J. Mauerhan, L. Meyer, J. Moutaka, K. Mužić, F. Najarro, J.-U. Pott, K. F. Schuster, L. O. Sjouwerman, C. Straubmeier, C. Thum, S. N. Vogel, H. Wiesenmeyer, M. Zamaninasab, and J. A. Zensus (2008). Simultaneous NIR/sub-mm observation of flare emission from Sagittarius A*. *A&A*, **492**, pp. 337–344. doi:10.1051/0004-6361:200810924.
- Eckart, A., R. Schödel, L. Meyer, S. Trippe, T. Ott, and R. Genzel (2006). Polarimetry of near-infrared flares from Sagittarius A*. *A&A*, **455**, pp. 1–10. doi:10.1051/0004-6361:20064948.
- Edwards, S., W. Fischer, L. Hillenbrand, and J. Kwan (2006). Probing T Tauri Accretion and Outflow with 1 Micron Spectroscopy. *ApJ*, **646**, pp. 319–341. doi:10.1086/504832.
- Eisenhauer, F., G. Perrin, W. Brandner, C. Straubmeier, A. Richichi, S. Gillessen, J. P. Berger, S. Hippler, A. Eckart, M. Schöller, S. Rabien, F. Cassaing, R. Lenzen, M. Thiel, Y. Clénet, J. R. Ramos, S. Kellner, P. Fédou, H. Baumeister, R. Hofmann, E. Gendron, A. Boehm, H. Bartko, X. Haubois, R. Klein, K. Dodds-Eden, K. Houairi, F. Hormuth, A. Gräter, L. Jocou, V. Naranjo, R. Genzel, P. Kervella, T. Henning, N. Hamaus, S. Lacour, U. Neumann, M. Haug, F. Malbet, W. Laun, J. Kolmeder, T. Paumard, R.-R. Rohloff, O. Pfuhl, K. Perraut, J. Ziegler, D. Rouan, and G. Rousset (2008). GRAVITY: getting to the event horizon of Sgr A*. In *Society of Photo-Optical Instrumentation Engineers (SPIE) Conference Series*, volume 7013 of *Society of Photo-Optical Instrumentation Engineers (SPIE) Conference Series*. doi:10.1117/12.788407.
- Eisner, J. A., G. W. Doppmann, J. R. Najita, D. McCarthy, C. Kulesa, B. J. Swift, and J. Teske (2010). Time-variable Accretion in the TW Hya Star/disk System. *ApJ*, **722**, pp. L28–L32. doi:10.1088/2041-8205/722/1/L28.
- Elias, J. H. (1978). A study of the Taurus dark cloud complex. *ApJ*, **224**, pp. 857–872. doi:10.1086/156436.

- Esposito, S., A. Riccardi, and B. Femenía (2000). Differential piston angular anisoplanatism for astronomical optical interferometers. *A&A*, **353**, pp. L29–L32.
- Etxaluze, M., H. A. Smith, V. Tolls, A. A. Stark, and E. González-Alfonso (2011). The Galactic Center in the Far-infrared. *AJ*, **142**, 134. doi:10.1088/0004-6256/142/4/134.
- Falcke, H., W. M. Goss, H. Matsuo, P. Teuben, J.-H. Zhao, and R. Zylka (1998). The Simultaneous Spectrum of Sagittarius A* from 20 Centimeters to 1 Millimeter and the Nature of the Millimeter Excess. *ApJ*, **499**, pp. 731–734.
- Fischer, W., S. Edwards, L. Hillenbrand, and J. Kwan (2011). Characterizing the IYJ Excess Continuum Emission in T Tauri Stars. *ApJ*, **730**, 73. doi:10.1088/0004-637X/730/2/73.
- Fish, V. L., S. S. Doeleman, C. Beaudoin, R. Blundell, D. E. Bolin, G. C. Bower, R. Chamberlin, R. Freund, P. Friberg, M. A. Gurwell, M. Honma, M. Inoue, T. P. Krichbaum, J. Lamb, D. P. Marrone, J. M. Moran, T. Oyama, R. Plambeck, R. Primiani, A. E. E. Rogers, D. L. Smythe, J. SooHoo, P. Strittmatter, R. P. J. Tilanus, M. Titus, J. Weintroub, M. Wright, D. Woody, K. H. Young, and L. M. Ziurys (2011). 1.3 mm Wavelength VLBI of Sagittarius A*: Detection of Time-variable Emission on Event Horizon Scales. *ApJ*, **727**, L36. doi:10.1088/2041-8205/727/2/L36.
- Fritz, T., S. Gillessen, S. Trippe, T. Ott, H. Bartko, O. Pfuhl, K. Dodds-Eden, R. Davies, F. Eisenhauer, and R. Genzel (2010). What is limiting near-infrared astrometry in the Galactic Centre? *MNRAS*, **401**, pp. 1177–1188. doi:10.1111/j.1365-2966.2009.15707.x.
- Gammie, C. F. (1996). Layered Accretion in T Tauri Disks. *ApJ*, **457**, p. 355. doi:10.1086/176735.
- Gammie, C. F. (2001). Nonlinear Outcome of Gravitational Instability in Cooling, Gaseous Disks. *ApJ*, **553**, pp. 174–183. doi:10.1086/320631.
- Genzel, R., F. Eisenhauer, and S. Gillessen (2010). The Galactic Center massive black hole and nuclear star cluster. *Reviews of Modern Physics*, **82**, pp. 3121–3195. doi:10.1103/RevModPhys.82.3121.
- Genzel, R., R. Schödel, T. Ott, F. Eisenhauer, R. Hofmann, M. Lehnert, A. Eckart, T. Alexander, A. Sternberg, R. Lenzen, Y. Clénet, F. Lacombe, D. Rouan, A. Renzini, and L. E. Tacconi-Garman (2003). The Stellar Cusp around the Supermassive Black Hole in the Galactic Center. *ApJ*, **594**, pp. 812–832. doi:10.1086/377127.
- Ghez, A. (2010). Stellar Orbits at the Galactic Center: Opportunities and Challenges. In *Dynamics from the Galactic Center to the Milky Way Halo*.

- Ghez, A. M., S. D. Hornstein, J. R. Lu, A. Bouchez, D. Le Mignant, M. A. van Dam, P. Wizinowich, K. Matthews, M. Morris, E. E. Becklin, R. D. Campbell, J. C. Y. Chin, S. K. Hartman, E. M. Johansson, R. E. Lafon, P. J. Stomski, and D. M. Summers (2005). The First Laser Guide Star Adaptive Optics Observations of the Galactic Center: Sgr A*'s Infrared Color and the Extended Red Emission in its Vicinity. *ApJ*, **635**, pp. 1087–1094. doi:10.1086/497576.
- Ghez, A. M., M. Morris, E. E. Becklin, A. Tanner, and T. Kremenek (2000). The accelerations of stars orbiting the Milky Way's central black hole. *Nature*, **407**, pp. 349–351. doi:10.1038/407349a.
- Ghez, A. M., G. Neugebauer, and K. Matthews (1993). The multiplicity of T Tauri stars in the star forming regions Taurus-Auriga and Ophiuchus-Scorpius: A 2.2 micron speckle imaging survey. *AJ*, **106**, pp. 2005–2023. doi:10.1086/116782.
- Ghez, A. M., S. Salim, N. N. Weinberg, J. R. Lu, T. Do, J. K. Dunn, K. Matthews, M. R. Morris, S. Yelda, E. E. Becklin, T. Kremenek, M. Milosavljevic, and J. Naiman (2008). Measuring Distance and Properties of the Milky Way's Central Supermassive Black Hole with Stellar Orbits. *ApJ*, **689**, pp. 1044–1062. doi:10.1086/592738.
- Gillessen, S., F. Eisenhauer, E. Quataert, R. Genzel, T. Paumard, S. Trippe, T. Ott, R. Abuter, A. Eckart, P. O. Lagage, M. D. Lehnert, L. J. Tacconi, and F. Martins (2006a). Variations in the Spectral Slope of Sagittarius A* during a Near-Infrared Flare. *ApJ*, **640**, pp. L163–L166. doi:10.1086/503557.
- Gillessen, S., F. Eisenhauer, S. Trippe, T. Alexander, R. Genzel, F. Martins, and T. Ott (2009a). Monitoring Stellar Orbits Around the Massive Black Hole in the Galactic Center. *ApJ*, **692**, pp. 1075–1109. doi:10.1088/0004-637X/692/2/1075.
- Gillessen, S., F. Eisenhauer, S. Trippe, T. Alexander, R. Genzel, F. Martins, and T. Ott (2009b). Monitoring Stellar Orbits Around the Massive Black Hole in the Galactic Center. *ApJ*, **692**, pp. 1075–1109. doi:10.1088/0004-637X/692/2/1075.
- Gillessen, S., G. Perrin, W. Brandner, C. Straubmeier, F. Eisenhauer, S. Rabien, A. Eckart, P. Lena, R. Genzel, T. Paumard, and S. Hippler (2006b). GRAVITY: the adaptive-optics-assisted two-object beam combiner instrument for the VLTI. In *Society of Photo-Optical Instrumentation Engineers (SPIE) Conference Series*, volume 6268 of *Society of Photo-Optical Instrumentation Engineers (SPIE) Conference Series*. doi:10.1117/12.671431.
- Goldston, J. E., E. Quataert, and I. V. Igumenshchev (2005). Synchrotron Radiation from Radiatively Inefficient Accretion Flow Simulations: Applications to Sagittarius A*. *ApJ*, **621**, pp. 785–792. doi:10.1086/427741.

- Griffin, M. J., A. Abergel, A. Abreu, P. A. R. Ade, P. André, J.-L. Augueres, T. Babbedge, Y. Bae, T. Baillie, J.-P. Baluteau, M. J. Barlow, G. Bendo, D. Benielli, J. J. Bock, P. Bonhomme, D. Brisbin, C. Brockley-Blatt, M. Caldwell, C. Cara, N. Castro-Rodriguez, R. Cerulli, P. Chaniel, S. Chen, E. Clark, D. L. Clements, L. Clerc, J. Coker, D. Communal, L. Conversi, P. Cox, D. Crumb, C. Cunningham, F. Daly, G. R. Davis, P. de Antoni, J. Delderfield, N. Devin, A. di Giorgio, I. Didschuns, K. Dohlen, M. Donati, A. Dowell, C. D. Dowell, L. Duband, L. Dumaye, R. J. Emery, M. Ferlet, D. Ferrand, J. Fontignie, M. Fox, A. Franceschini, M. Frerking, T. Fulton, J. Garcia, R. Gastaud, W. K. Gear, J. Glenn, A. Goizel, D. K. Griffin, T. Grundy, S. Guest, L. Guillemet, P. C. Hargrave, M. Harwit, P. Hastings, E. Hatziminaoglou, M. Herman, B. Hinde, V. Hristov, M. Huang, P. Imhof, K. J. Isaak, U. Israelsson, R. J. Ivison, D. Jennings, B. Kiernan, K. J. King, A. E. Lange, W. Latter, G. Laurent, P. Laurent, S. J. Leeks, E. Lellouch, L. Levenson, B. Li, J. Li, J. Lilienthal, T. Lim, S. J. Liu, N. Lu, S. Madden, G. Mainetti, P. Marliani, D. McKay, K. Mercier, S. Molinari, H. Morris, H. Moseley, J. Mulder, M. Mur, D. A. Naylor, H. Nguyen, B. O'Halloran, S. Oliver, G. Olofsson, H.-G. Olofsson, R. Orfei, M. J. Page, I. Pain, P. Panuzzo, A. Papageorgiou, G. Parks, P. Parr-Burman, A. Pearce, C. Pearson, I. Pérez-Fournon, F. Pinsard, G. Pisano, J. Podosek, M. Pohlen, E. T. Polehampton, D. Pouliquen, D. Rigopoulou, D. Rizzo, I. G. Roseboom, H. Roussel, M. Rowan-Robinson, B. Rownd, P. Saraceno, M. Sauvage, R. Savage, G. Savini, E. Sawyer, C. Scharmberg, D. Schmitt, N. Schneider, B. Schulz, A. Schwartz, R. Shafer, D. L. Shupe, B. Sibthorpe, S. Sidher, A. Smith, A. J. Smith, D. Smith, L. Spencer, B. Stobie, R. Sudiwala, K. Sukhatme, C. Surace, J. A. Stevens, B. M. Swinyard, M. Trichas, T. Tourette, H. Triou, S. Tseng, C. Tucker, A. Turner, M. Vaccari, I. Valtchanov, L. Vigroux, E. Virique, G. Voellmer, H. Walker, R. Ward, T. Waskett, M. Weilert, R. Wesson, G. J. White, N. Whitehouse, C. D. Wilson, B. Winter, A. L. Woodcraft, G. S. Wright, C. K. Xu, A. Zavagno, M. Zemcov, L. Zhang, and E. Zonca (2010). The Herschel-SPIRE instrument and its in-flight performance. *A&A*, **518**, L3. doi:10.1051/0004-6361/201014519.
- Güdel, M., F. Lahuis, K. R. Briggs, J. Carr, A. E. Glassgold, T. Henning, J. R. Najita, R. van Boekel, and E. F. van Dishoeck (2010). On the origin of [NeII] 12.81 μm emission from pre-main sequence stars: Disks, jets, and accretion. *A&A*, **519**, A113. doi:10.1051/0004-6361/200913971.
- Hallinan, G., S. P. Littlefair, G. Cotter, S. Bourke, L. K. Harding, J. S. Pineda, R. P. Butler, A. Golden, G. Basri, J. G. Doyle, M. M. Kao, S. V. Berdyugina, A. Kuznetsov, M. P. Rupen, and A. Antonova (2015). Magnetospherically driven optical and radio aurorae at the end of the stellar main sequence. *Nature*, **523**, pp. 568–571. doi:10.1038/nature14619.

- Hartigan, P., S. Edwards, and L. Ghandour (1995). Disk Accretion and Mass Loss from Young Stars. *ApJ*, **452**, p. 736. doi:10.1086/176344.
- Hartigan, P. and S. J. Kenyon (2003). A Spectroscopic Survey of Subarcsecond Binaries in the Taurus-Auriga Dark Cloud with the Hubble Space Telescope. *ApJ*, **583**, pp. 334–357. doi:10.1086/345293.
- Haubois, X., K. Dodds-Eden, A. Weiss, T. Paumard, G. Perrin, Y. Clénet, S. Gillessen, P. Kervella, F. Eisenhauer, R. Genzel, and D. Rouan (2012). Flares and variability from Sagittarius A*: five nights of simultaneous multi-wavelength observations. *A&A*, **540**, A41. doi:10.1051/0004-6361/201117725.
- Hayashi, C. (1981). Structure of the Solar Nebula, Growth and Decay of Magnetic Fields and Effects of Magnetic and Turbulent Viscosities on the Nebula. *Progress of Theoretical Physics Supplement*, **70**, pp. 35–53. doi:10.1143/PTPS.70.35.
- Herbst, T. M., C. D. Koresko, and C. Leinert (1995). Detection of shocked molecular hydrogen in infrared companions to T Tauri stars: Evidence for ongoing accretion. *ApJ*, **444**, pp. L93–L96. doi:10.1086/187868.
- Hinkle, K. H., L. Wallace, and W. Livingston (2003). Atmospheric Transmission Above Kitt Peak, 0.5 to 5.5 microns. In *American Astronomical Society Meeting Abstracts*, volume 35 of *Bulletin of the American Astronomical Society*, p. 1260.
- Hinz, P. M., T. Connors, T. McMahon, A. Cheng, C. Y. Peng, W. Hoffmann, D. McCarthy, Jr., and R. Angel (2004). Large Binocular Telescope Interferometer: the universal beam combiner. In Traub, W. A. (ed.) *New Frontiers in Stellar Interferometry*, volume 5491 of *Society of Photo-Optical Instrumentation Engineers (SPIE) Conference Series*, p. 787.
- Hinz, P. M., T. J. Rodigas, M. A. Kenworthy, S. Sivanandam, A. N. Heinze, E. E. Mamajek, and M. R. Meyer (2010). Thermal Infrared MMTAO Observations of the HR 8799 Planetary System. *ApJ*, **716**, pp. 417–426. doi:10.1088/0004-637X/716/1/417.
- Hioki, T., Y. Itoh, Y. Oasa, M. Fukagawa, T. Kudo, S. Mayama, H. Funayama, M. Hayashi, S. S. Hayashi, T.-S. Pyo, M. Ishii, T. Nishikawa, and M. Tamura (2007). Near-Infrared Coronagraphic Observations of the T Tauri Binary System UY Aur. *AJ*, **134**, pp. 880–885. doi:10.1086/519737.
- Horne, K. (1986). An optimal extraction algorithm for CCD spectroscopy. *PASP*, **98**, pp. 609–617. doi:10.1086/131801.
- Hornstein, S. D., K. Matthews, A. M. Ghez, J. R. Lu, M. Morris, E. E. Becklin, M. Rafelski, and F. K. Baganoff (2007). A Constant Spectral Index for Sagittarius

- A* during Infrared/X-Ray Intensity Variations. *ApJ*, **667**, pp. 900–910. doi:10.1086/520762.
- Hubeny, I. and A. Burrows (2007). A Systematic Study of Departures from Chemical Equilibrium in the Atmospheres of Substellar Mass Objects. *ApJ*, **669**, pp. 1248–1261. doi:10.1086/522107.
- Husser, T.-O., S. Wende-von Berg, S. Dreizler, D. Homeier, A. Reiners, T. Barman, and P. H. Hauschildt (2013). A new extensive library of PHOENIX stellar atmospheres and synthetic spectra. *A&A*, **553**, A6. doi:10.1051/0004-6361/201219058.
- Jacquet, E., S. Balbus, and H. Latter (2011). On linear dust-gas streaming instabilities in protoplanetary discs. *MNRAS*, **415**, pp. 3591–3598. doi:10.1111/j.1365-2966.2011.18971.x.
- Johansen, A., J. S. Oishi, M.-M. Mac Low, H. Klahr, T. Henning, and A. Youdin (2007). Rapid planetesimal formation in turbulent circumstellar disks. *Nature*, **448**, pp. 1022–1025. doi:10.1038/nature06086.
- Joy, A. H. and G. van Biesbrok (1944). Five new double stars among variables of the T Tauri class. *PASP*, **56**, p. 123.
- Kennea, J. A., D. N. Burrows, C. Kouveliotou, D. M. Palmer, E. Göğüş, Y. Kaneko, P. A. Evans, N. Degenaar, M. T. Reynolds, J. M. Miller, R. Wijnands, K. Mori, and N. Gehrels (2013). Swift Discovery of a New Soft Gamma Repeater, SGR J1745-29, near Sagittarius A*. *ApJ*, **770**, L24. doi:10.1088/2041-8205/770/2/L24.
- Krabbe, A., R. Genzel, A. Eckart, F. Najarro, D. Lutz, M. Cameron, H. Kroker, L. E. Tacconi-Garman, N. Thatte, L. Weitzel, S. Drapatz, T. Geballe, A. Sternberg, and R. Kudritzki (1995). The Nuclear Cluster of the Milky Way: Star Formation and Velocity Dispersion in the Central 0.5 Parsec. *ApJ*, **447**, p. L95. doi:10.1086/309579.
- Kratter, K. M., C. D. Matzner, and M. R. Krumholz (2008). Global Models for the Evolution of Embedded, Accreting Protostellar Disks. *ApJ*, **681**, pp. 375–390. doi:10.1086/587543.
- Kratter, K. M., R. A. Murray-Clay, and A. N. Youdin (2010). The Runts of the Litter: Why Planets Formed Through Gravitational Instability Can Only Be Failed Binary Stars. *ApJ*, **710**, pp. 1375–1386. doi:10.1088/0004-637X/710/2/1375.
- Kraus, A. L., M. J. Ireland, F. Martinache, and L. A. Hillenbrand (2011). Mapping the Shores of the Brown Dwarf Desert. II. Multiple Star Formation in Taurus-Auriga. *ApJ*, **731**, 8. doi:10.1088/0004-637X/731/1/8.

- Kuchner, M. J. (2004). A Minimum-Mass Extrasolar Nebula. *ApJ*, **612**, pp. 1147–1151. doi:10.1086/422577.
- Lada, C. J. (2006). Stellar Multiplicity and the Initial Mass Function: Most Stars Are Single. *ApJ*, **640**, pp. L63–L66. doi:10.1086/503158.
- Lambrechts, M. and A. Johansen (2012). Rapid growth of gas-giant cores by pebble accretion. *A&A*, **544**, A32. doi:10.1051/0004-6361/201219127.
- Lane, B. F. and M. M. Colavita (2003). Phase-referenced Stellar Interferometry at the Palomar Testbed Interferometer. *AJ*, **125**, pp. 1623–1628. doi:10.1086/367793.
- Lawson, P. R. (ed.) (2000). *Principles of Long Baseline Stellar Interferometry*.
- Leinert, C., H. Zinnecker, N. Weitzel, J. Christou, S. T. Ridgway, R. Jameson, M. Haas, and R. Lenzen (1993). A systematic approach for young binaries in Taurus. *A&A*, **278**, pp. 129–149.
- Lin, D. N. C. and J. Papaloizou (1979). On the structure of circumbinary accretion disks and the tidal evolution of commensurable satellites. *MNRAS*, **188**, pp. 191–201.
- Liu, M. C., E. A. Magnier, N. R. Deacon, K. N. Allers, T. J. Dupuy, M. C. Kotsen, K. M. Aller, W. S. Burgett, K. C. Chambers, P. W. Draper, K. W. Hodapp, R. Jedicke, N. Kaiser, R.-P. Kudritzki, N. Metcalfe, J. S. Morgan, P. A. Price, J. L. Tonry, and R. J. Wainscoat (2013). The Extremely Red, Young L Dwarf PSO J318.5338-22.8603: A Free-floating Planetary-mass Analog to Directly Imaged Young Gas-giant Planets. *ApJ*, **777**, L20. doi:10.1088/2041-8205/777/2/L20.
- Lloyd-Hart, M. (2000). Thermal Performance Enhancement of Adaptive Optics by Use of a Deformable Secondary Mirror. *PASP*, **112**, pp. 264–272. doi:10.1086/316503.
- Lodato, G., E. Delgado-Donate, and C. J. Clarke (2005). Constraints on the formation mechanism of the planetary mass companion of 2MASS 1207334-393254. *MNRAS*, **364**, pp. L91–L95. doi:10.1111/j.1745-3933.2005.00112.x.
- Lodato, G. and W. K. M. Rice (2004). Testing the locality of transport in self-gravitating accretion discs. *MNRAS*, **351**, pp. 630–642. doi:10.1111/j.1365-2966.2004.07811.x.
- Lord, S. D. (1992). A new software tool for computing Earth’s atmospheric transmission of near- and far-infrared radiation. Technical Memorandum NASA-TM-103957, A-92154, NAS 1.15:103957, NASA, NASA Ames Research Center; Moffett Field, CA, United States.

- Lowrance, P. J., C. McCarthy, E. E. Becklin, B. Zuckerman, G. Schneider, R. A. Webb, D. C. Hines, J. D. Kirkpatrick, D. W. Koerner, F. Low, R. Meier, M. Rieke, B. A. Smith, R. J. Terrile, and R. I. Thompson (1999). A Candidate Substellar Companion to CD -33deg7795 (TWA 5). *ApJ*, **512**, pp. L69–L72. doi:10.1086/311858.
- Lowrance, P. J., G. Schneider, J. D. Kirkpatrick, E. E. Becklin, A. J. Weinberger, B. Zuckerman, P. Plait, E. M. Malmuth, S. R. Heap, A. Schultz, B. A. Smith, R. J. Terrile, and D. C. Hines (2000). A Candidate Substellar Companion to HR 7329. *ApJ*, **541**, pp. 390–395. doi:10.1086/309437.
- Luhman, K. L. (2012). The Formation and Early Evolution of Low-Mass Stars and Brown Dwarfs. *ARA&A*, **50**, pp. 65–106. doi:10.1146/annurev-astro-081811-125528.
- Macintosh, B., J. Graham, D. Palmer, R. Doyon, D. Gavel, J. Larkin, B. Oppenheimer, L. Saddlemyer, J. K. Wallace, B. Bauman, J. Evans, D. Erikson, K. Morzinski, D. Phillion, L. Poyneer, A. Sivaramakrishnan, R. Soummer, S. Thibault, and J.-P. Veran (2006). The Gemini Planet Imager. In *Society of Photo-Optical Instrumentation Engineers (SPIE) Conference Series*, volume 6272 of *Society of Photo-Optical Instrumentation Engineers (SPIE) Conference Series*, p. 0. doi:10.1117/12.672430.
- Macintosh, B., J. R. Graham, T. Barman, R. J. De Rosa, Q. Konopacky, M. S. Marley, C. Marois, E. L. Nielsen, L. Pueyo, A. Rajan, J. Rameau, D. Saumon, J. J. Wang, M. Ammons, P. Arriaga, E. Artigau, S. Beckwith, J. Brewster, S. Bruzzone, J. Bulger, B. Burningham, A. S. Burrows, C. Chen, E. Chiang, J. K. Chilcote, R. I. Dawson, R. Dong, R. Doyon, Z. H. Draper, G. Duchêne, T. M. Esposito, D. Fabrycky, M. P. Fitzgerald, K. B. Follette, J. J. Fortney, B. Gerard, S. Goodsell, A. Z. Greenbaum, P. Hibon, S. Hinkley, T. Hufford, L.-W. Hung, P. Ingraham, M. Johnson-Groh, P. Kalas, D. Lafreniere, J. E. Larkin, J. Lee, M. Line, D. Long, J. Maire, F. Marchis, B. C. Matthews, C. E. Max, S. Metchev, M. A. Millar-Blanchaer, T. Mittal, C. V. Morley, K. M. Morzinski, R. Murray-Clay, R. Oppenheimer, D. W. Palmer, R. Patel, J. Patience, M. D. Perrin, L. A. Poyneer, R. R. Rafikov, F. T. Rantakyro, E. Rice, P. Rojo, A. R. Rudy, J.-B. Ruffio, M. T. Ruiz, N. Sadakuni, L. Saddlemyer, M. Salama, D. Savransky, A. C. Schneider, A. Sivaramakrishnan, I. Song, R. Soummer, S. Thomas, G. Vasisht, J. K. Wallace, K. Ward-Duong, S. J. Wiktorowicz, S. G. Wolff, and B. Zuckerman (2015). Discovery and spectroscopy of the young Jovian planet 51 Eri b with the Gemini Planet Imager. *ArXiv e-prints*.
- Mamajek, E. E., M. R. Meyer, P. M. Hinz, W. F. Hoffmann, M. Cohen, and J. L. Hora (2004). Constraining the Lifetime of Circumstellar Disks in the Terrestrial Planet

- Zone: A Mid-Infrared Survey of the 30 Myr old Tucana-Horologium Association. *ApJ*, **612**, pp. 496–510. doi:10.1086/422550.
- Marley, M. S. and T. D. Robinson (2014). On the Cool Side: Modeling the Atmospheres of Brown Dwarfs and Giant Planets. *ArXiv e-prints*.
- Marley, M. S., D. Saumon, M. Cushing, A. S. Ackerman, J. J. Fortney, and R. Freedman (2012). Masses, Radii, and Cloud Properties of the HR 8799 Planets. *ApJ*, **754**, 135. doi:10.1088/0004-637X/754/2/135.
- Marois, C., B. Macintosh, T. Barman, B. Zuckerman, I. Song, J. Patience, D. Lafrenière, and R. Doyon (2008). Direct Imaging of Multiple Planets Orbiting the Star HR 8799. *Science*, **322**, pp. 1348–. doi:10.1126/science.1166585.
- Marois, C., B. Zuckerman, Q. M. Konopacky, B. Macintosh, and T. Barman (2010). Images of a fourth planet orbiting HR 8799. *Nature*, **468**, pp. 1080–1083. doi:10.1038/nature09684.
- Marrone, D. P., F. K. Baganoff, M. R. Morris, J. M. Moran, A. M. Ghez, S. D. Hornstein, C. D. Dowell, D. J. Muñoz, M. W. Bautz, G. R. Ricker, W. N. Brandt, G. P. Garmire, J. R. Lu, K. Matthews, J.-H. Zhao, R. Rao, and G. C. Bower (2008). An X-Ray, Infrared, and Submillimeter Flare of Sagittarius A*. *ApJ*, **682**, pp. 373–383. doi:10.1086/588806.
- Marrone, D. P., J. M. Moran, J.-H. Zhao, and R. Rao (2006). The Submillimeter Polarization of Sgr A*. *Journal of Physics Conference Series*, **54**, pp. 354–362. doi:10.1088/1742-6596/54/1/056.
- Matzner, C. D. and Y. Levin (2005). Protostellar Disks: Formation, Fragmentation, and the Brown Dwarf Desert. *ApJ*, **628**, pp. 817–831. doi:10.1086/430813.
- McKee, C. F. and E. C. Ostriker (2007). Theory of Star Formation. *ARA&A*, **45**, pp. 565–687. doi:10.1146/annurev.astro.45.051806.110602.
- Merritt, D., T. Alexander, S. Mikkola, and C. M. Will (2011). Stellar dynamics of extreme-mass-ratio inspirals. *Phys. Rev. D*, **84**(4), 044024. doi:10.1103/PhysRevD.84.044024.
- Meyer, L., T. Do, A. Ghez, M. R. Morris, S. Yelda, R. Schödel, and A. Eckart (2009). A Power-Law Break in the Near-Infrared Power Spectrum of the Galactic Center Black Hole. *ApJ*, **694**, pp. L87–L91. doi:10.1088/0004-637X/694/1/L87.
- Meyer, L., A. M. Ghez, R. Schödel, S. Yelda, A. Boehle, J. R. Lu, T. Do, M. R. Morris, E. E. Becklin, and K. Matthews (2012). The Shortest-Known-Period Star Orbiting Our Galaxy’s Supermassive Black Hole. *Science*, **338**, pp. 84–. doi:10.1126/science.1225506.

- Miyake, K. and Y. Nakagawa (1993). Effects of particle size distribution on opacity curves of protoplanetary disks around T Tauri stars. *icarus*, **106**, p. 20. doi:10.1006/icar.1993.1156.
- Muzerolle, J., L. Hartmann, and N. Calvet (1998). A Brgamma Probe of Disk Accretion in T Tauri Stars and Embedded Young Stellar Objects. *AJ*, **116**, pp. 2965–2974. doi:10.1086/300636.
- Neilsen, J., M. A. Nowak, C. Gammie, J. Dexter, S. Markoff, D. Haggard, S. Nayakshin, Q. D. Wang, N. Grosso, D. Porquet, J. A. Tomsick, N. Degenaar, P. C. Fragile, J. C. Houck, R. Wijnands, J. M. Miller, and F. K. Baganoff (2013). A Chandra/HETGS Census of X-Ray Variability from Sgr A* during 2012. *ApJ*, **774**, 42. doi:10.1088/0004-637X/774/1/42.
- Neuhäuser, R., C. Ginski, T. O. B. Schmidt, and M. Mugrauer (2011). Further deep imaging of HR 7329 A (η Tel A) and its brown dwarf companion B. *MNRAS*, **416**, pp. 1430–1435. doi:10.1111/j.1365-2966.2011.19139.x.
- Neuhäuser, R., E. W. Guenther, M. G. Petr, W. Brandner, N. Huélamo, and J. Alves (2000). Spectrum and proper motion of a brown dwarf companion of the T Tauri star CoD-33/*circ*7795. *A&A*, **360**, pp. L39–L42.
- Nomura, H., Y. Aikawa, M. Tsujimoto, Y. Nakagawa, and T. J. Millar (2007). Molecular Hydrogen Emission from Protoplanetary Disks. II. Effects of X-Ray Irradiation and Dust Evolution. *ApJ*, **661**, pp. 334–353. doi:10.1086/513419.
- Öberg, K. I., R. Murray-Clay, and E. A. Bergin (2011). The Effects of Snowlines on C/O in Planetary Atmospheres. *ApJ*, **743**, L16. doi:10.1088/2041-8205/743/1/L16.
- Ochi, Y., K. Sugimoto, and T. Hanawa (2005). Evolution of a Protobinary: Accretion Rates of the Primary and Secondary. *ApJ*, **623**, pp. 922–939. doi:10.1086/428601.
- Olling, R. P. and M. R. Merrifield (2000). Two measures of the shape of the dark halo of the Milky Way. *MNRAS*, **311**, pp. 361–369. doi:10.1046/j.1365-8711.2000.03053.x.
- Ormel, C. W. and H. H. Klahr (2010). The effect of gas drag on the growth of protoplanets. Analytical expressions for the accretion of small bodies in laminar disks. *A&A*, **520**, A43. doi:10.1051/0004-6361/201014903.
- Paumard, T., R. Genzel, F. Martins, S. Nayakshin, A. M. Beloborodov, Y. Levin, S. Trippe, F. Eisenhauer, T. Ott, S. Gillessen, R. Abuter, J. Cuadra, T. Alexander, and A. Sternberg (2006). The Two Young Star Disks in the Central Parsec of the Galaxy: Properties, Dynamics, and Formation. *ApJ*, **643**, pp. 1011–1035. doi:10.1086/503273.

- Pecaut, M. J. and E. E. Mamajek (2013). Intrinsic Colors, Temperatures, and Bolometric Corrections of Pre-main-sequence Stars. *ApJS*, **208**, 9. doi:10.1088/0067-0049/208/1/9.
- Pierce-Price, D., J. S. Richer, J. S. Greaves, W. S. Holland, T. Jenness, A. N. Lasenby, G. J. White, H. E. Matthews, D. Ward-Thompson, W. R. F. Dent, R. Zylka, P. Mezger, T. Hasegawa, T. Oka, A. Omont, and G. Gilmore (2000). A Deep Submillimeter Survey of the Galactic Center. *ApJ*, **545**, pp. L121–L125. doi:10.1086/317884.
- Pollack, J. B., O. Hubickyj, P. Bodenheimer, J. J. Lissauer, M. Podolak, and Y. Greenzweig (1996). Formation of the Giant Planets by Concurrent Accretion of Solids and Gas. *Icarus*, **124**, pp. 62–85. doi:10.1006/icar.1996.0190.
- Porquet, D., P. Predehl, B. Aschenbach, N. Grosso, A. Goldwurm, P. Goldoni, R. S. Warwick, and A. Decourchelle (2003). XMM-Newton observation of the brightest X-ray flare detected so far from Sgr A*. *A&A*, **407**, pp. L17–L20. doi:10.1051/0004-6361:20030983.
- Pott, J.-U., A. Eckart, A. Glindemann, S. Kraus, R. Schödel, A. M. Ghez, J. Woillez, and G. Weigelt (2008a). First VLTI infrared spectro-interferometry on GCIRS 7. Characterizing the prime reference source for Galactic center observations at highest angular resolution. *A&A*, **487**, pp. 413–418. doi:10.1051/0004-6361:200809829.
- Pott, J.-U., J. Woillez, P. L. Wizinowich, A. Eckart, A. Glindemann, A. M. Ghez, and J. R. Graham (2008b). First spectro-interferometry on galactic center sources in the infrared: results and science prospects at the sensitivity limit of current larger aperture arrays. In *Society of Photo-Optical Instrumentation Engineers (SPIE) Conference Series*, volume 7013 of *Society of Photo-Optical Instrumentation Engineers (SPIE) Conference Series*. doi:10.1117/12.788245.
- Prato, L. and M. Simon (1997). Are Both Stars in a Classic T Tauri Binary Classic T Tauri Stars? *ApJ*, **474**, p. 455. doi:10.1086/303442.
- Pringle, J. E. (1981). Accretion discs in astrophysics. *ARA&A*, **19**, pp. 137–162. doi:10.1146/annurev.aa.19.090181.001033.
- Pyo, T.-S., M. Hayashi, T. L. Beck, C. J. Davis, and M. Takami (2014). [Fe II] Emissions Associated with the Young Interacting Binary UY Aurigae. *ApJ*, **786**, 63. doi:10.1088/0004-637X/786/1/63.
- Raghavan, D., H. A. McAlister, T. J. Henry, D. W. Latham, G. W. Marcy, B. D. Mason, D. R. Gies, R. J. White, and T. A. ten Brummelaar (2010). A Survey of Stellar Families: Multiplicity of Solar-type Stars. *ApJS*, **190**, pp. 1–42. doi:10.1088/0067-0049/190/1/1.

- Read, A. M., S. R. Rosen, R. D. Saxton, and J. Ramirez (2011). A new comprehensive 2D model of the point spread functions of the XMM-Newton EPIC telescopes: spurious source suppression and improved positional accuracy. *A&A*, **534**, A34. doi:10.1051/0004-6361/201117525.
- Reid, M. J., K. M. Menten, X. W. Zheng, A. Brunthaler, L. Moscadelli, Y. Xu, B. Zhang, M. Sato, M. Honma, T. Hirota, K. Hachisuka, Y. K. Choi, G. A. Moellenbrock, and A. Bartkiewicz (2009). Trigonometric Parallaxes of Massive Star-Forming Regions. VI. Galactic Structure, Fundamental Parameters, and Non-circular Motions. *ApJ*, **700**, pp. 137–148. doi:10.1088/0004-637X/700/1/137.
- Rieke, G. H. and M. J. Rieke (1988). Stellar velocities and the mass distribution in the Galactic center. *ApJ*, **330**, pp. L33–L37. doi:10.1086/185199.
- Royer, F., S. Grenier, M.-O. Baylac, A. E. Gómez, and J. Zorec (2002). Rotational velocities of A-type stars in the northern hemisphere. II. Measurement of $v \sin i$. *A&A*, **393**, pp. 897–911. doi:10.1051/0004-6361:20020943.
- Rubilar, G. F. and A. Eckart (2001). Periastron shifts of stellar orbits near the Galactic Center. *A&A*, **374**, pp. 95–104. doi:10.1051/0004-6361:20010640.
- Salyk, C., G. J. Herczeg, J. M. Brown, G. A. Blake, K. M. Pontoppidan, and E. F. van Dishoeck (2013). Measuring Protoplanetary Disk Accretion with H I Pfund β . *ApJ*, **769**, 21. doi:10.1088/0004-637X/769/1/21.
- Sánchez-Portal, M., A. Marston, B. Altieri, H. Aussel, H. Feuchtgruber, U. Klaas, H. Linz, D. Lutz, B. Merín, T. Müller, M. Nielbock, M. Oort, G. Pilbratt, M. Schmidt, C. Stephenson, and M. Tuttlebee (2014). The pointing system of the Herschel space observatory. Description, Calibration, Performance and improvements. *Experimental Astronomy*, **37**, pp. 453–479. doi:10.1007/s10686-014-9396-z.
- Schödel, R., T. Ott, R. Genzel, R. Hofmann, M. Lehnert, A. Eckart, N. Mouawad, T. Alexander, M. J. Reid, R. Lenzen, M. Hartung, F. Lacombe, D. Rouan, E. Gendron, G. Rousset, A.-M. Lagrange, W. Brandner, N. Ageorges, C. Lidman, A. F. M. Moorwood, J. Spyromilio, N. Hubin, and K. M. Menten (2002). A star in a 15.2-year orbit around the supermassive black hole at the centre of the Milky Way. *Nature*, **419**, pp. 694–696. doi:10.1038/nature01121.
- Serabyn, E., J. Carlstrom, O. Lay, D. C. Lis, T. R. Hunter, J. H. Lacy, and R. E. Hills (1997). High-Frequency Measurements of the Spectrum of Sagittarius A*. *ApJ*, **490**, pp. L77–L81. doi:10.1086/311010.
- Shakura, N. I. and R. A. Sunyaev (1973). Black holes in binary systems. Observational appearance. *A&A*, **24**, pp. 337–355.

- Shao, M. and M. M. Colavita (1992). Potential of long-baseline infrared interferometry for narrow-angle astrometry. *A&A*, **262**, pp. 353–358.
- Sivanandam, S., P. M. Hinz, A. N. Heinze, M. Freed, and A. H. Breuninger (2006). Clio: a 3-5 micron AO planet-finding camera. In *Society of Photo-Optical Instrumentation Engineers (SPIE) Conference Series*, volume 6269 of *Society of Photo-Optical Instrumentation Engineers (SPIE) Conference Series*, p. 0. doi:10.1117/12.672344.
- Skemer, A. J., L. M. Close, P. M. Hinz, W. F. Hoffmann, T. P. Greene, J. R. Males, and T. L. Beck (2010). ISM Dust Grains and N-band Spectral Variability in the Spatially Resolved Subarcsecond Binary UY Aur. *ApJ*, **711**, pp. 1280–1290. doi:10.1088/0004-637X/711/2/1280.
- Skemer, A. J., L. M. Close, L. Szűcs, D. Apai, I. Pascucci, and B. A. Biller (2011). Evidence Against an Edge-on Disk Around the Extrasolar Planet, 2MASS 1207 b and a New Thick-cloud Explanation for Its Underluminosity. *ApJ*, **732**, 107. doi:10.1088/0004-637X/732/2/107.
- Skemer, A. J., P. M. Hinz, S. Esposito, A. Burrows, J. Leisenring, M. Skrutskie, S. Desidera, D. Mesa, C. Arcidiacono, F. Mannucci, T. J. Rodigas, L. Close, D. McCarthy, C. Kulesa, G. Agapito, D. Apai, J. Argomedo, V. Bailey, K. Boutsia, R. Briguglio, G. Brusa, L. Busoni, R. Claudi, J. Eisner, L. Fini, K. B. Follette, P. Garnavich, R. Gratton, J. C. Guerra, J. M. Hill, W. F. Hoffmann, T. Jones, M. Krejny, J. Males, E. Masciadri, M. R. Meyer, D. L. Miller, K. Morzinski, M. Nelson, E. Pinna, A. Puglisi, S. P. Quanz, F. Quiros-Pacheco, A. Riccardi, P. Stefanini, V. Vaitheeswaran, J. C. Wilson, and M. Kompero (2012). First Light LBT AO Images of HR 8799 bcde at 1.6 and 3.3 μm : New Discrepancies between Young Planets and Old Brown Dwarfs. *ApJ*, **753**, 14. doi:10.1088/0004-637X/753/1/14.
- Skemer, A. J., M. S. Marley, P. M. Hinz, K. M. Morzinski, M. F. Skrutskie, J. M. Leisenring, L. M. Close, D. Saumon, V. P. Bailey, R. Briguglio, D. Defrere, S. Esposito, K. B. Follette, J. M. Hill, J. R. Males, A. Puglisi, T. J. Rodigas, and M. Kompero (2014). Directly Imaged L-T Transition Exoplanets in the Mid-infrared. *ApJ*, **792**, 17. doi:10.1088/0004-637X/792/1/17.
- Skrutskie, M. F., M. R. Meyer, D. Whalen, and C. Hamilton (1996). Near-Infrared Photometric Monitoring of Young Stellar Objects. *AJ*, **112**, p. 2168. doi:10.1086/118172.
- Stephens, D. C., S. K. Leggett, M. C. Cushing, M. S. Marley, D. Saumon, T. R. Geballe, D. A. Golimowski, X. Fan, and K. S. Noll (2009). The 0.8-14.5 μm Spectra of Mid-L to Mid-T Dwarfs: Diagnostics of Effective Temperature, Grain

- Sedimentation, Gas Transport, and Surface Gravity. *ApJ*, **702**, pp. 154–170. doi:10.1088/0004-637X/702/1/154.
- Stone, J. M., J. A. Eisner, J. D. Monnier, J. Woillez, P. Wizinowich, J.-U. Pott, and A. M. Ghez (2012). Disentangling Confused Stars at the Galactic Center with Long-baseline Infrared Interferometry. *ApJ*, **754**, 151. doi:10.1088/0004-637X/754/2/151.
- Stone, J. M., J. A. Eisner, C. Salyk, C. Kulesa, and D. McCarthy (2014). Variable Accretion Processes in the Young Binary-star System UY Aur. *ApJ*, **792**, 56. doi:10.1088/0004-637X/792/1/56.
- Strüder, L., U. Briel, K. Dennerl, R. Hartmann, E. Kendziorra, N. Meidinger, E. Pfeffermann, C. Reppin, B. Aschenbach, W. Bornemann, H. Bräuninger, W. Burkert, M. Elender, M. Freyberg, F. Haberl, G. Hartner, F. Heuschmann, H. Hippmann, E. Kastelic, S. Kemmer, G. Kettenring, W. Kink, N. Krause, S. Müller, A. Oppitz, W. Pietsch, M. Popp, P. Predehl, A. Read, K. H. Stephan, D. Stötter, J. Trümper, P. Holl, J. Kemmer, H. Soltau, R. Stötter, U. Weber, U. Weichert, C. von Zanthier, D. Carathanassis, G. Lutz, R. H. Richter, P. Solc, H. Böttcher, M. Kuster, R. Staubert, A. Abbey, A. Holland, M. Turner, M. Balasini, G. F. Bignami, N. La Palombara, G. Villa, W. Buttler, F. Gianini, R. Lainé, D. Lumb, and P. Dhez (2001). The European Photon Imaging Camera on XMM-Newton: The pn-CCD camera. *A&A*, **365**, pp. L18–L26. doi:10.1051/0004-6361:20000066.
- Toomre, A. (1964). On the gravitational stability of a disk of stars. *ApJ*, **139**, pp. 1217–1238. doi:10.1086/147861.
- Torres, C. A. O., L. da Silva, G. R. Quast, R. de la Reza, and E. Jilinski (2000). A New Association of Post-T Tauri Stars near the Sun. *AJ*, **120**, pp. 1410–1425. doi:10.1086/301539.
- Torres, C. A. O., G. R. Quast, L. da Silva, R. de La Reza, C. H. F. Melo, and M. Sterzik (2006). Search for associations containing young stars (SACY). I. Sample and searching method. *A&A*, **460**, pp. 695–708. doi:10.1051/0004-6361:20065602.
- Turner, M. J. L., A. Abbey, M. Arnaud, M. Balasini, M. Barbera, E. Belsole, P. J. Bennie, J. P. Bernard, G. F. Bignami, M. Boer, U. Briel, I. Butler, C. Cara, C. Chabaud, R. Cole, A. Collura, M. Conte, A. Cros, M. Denby, P. Dhez, G. Di Coco, J. Dowson, P. Ferrando, S. Ghizzardi, F. Gianotti, C. V. Goodall, L. Gretton, R. G. Griffiths, O. Hainaut, J. F. Hochedez, A. D. Holland, E. Jourdain, E. Kendziorra, A. Lagostina, R. Laine, N. La Palombara, M. Lortholary, D. Lumb, P. Marty, S. Molendi, C. Pigot, E. Poindron, K. A. Pounds, J. N. Reeves, C. Reppin, R. Rothenflug, P. Salvétat, J. L. Sauvageot, D. Schmitt,

- S. Sembay, A. D. T. Short, J. Spragg, J. Stephen, L. Strüder, A. Tiengo, M. Trifoglio, J. Trümper, S. Vercellone, L. Vigroux, G. Villa, M. J. Ward, S. Whitehead, and E. Zonca (2001). The European Photon Imaging Camera on XMM-Newton: The MOS cameras : The MOS cameras. *A&A*, **365**, pp. L27–L35. doi:10.1051/0004-6361:20000087.
- Vincent, F. H., T. Paumard, G. Perrin, L. Mugnier, F. Eisenhauer, and S. Gillessen (2011). Performance of astrometric detection of a hotspot orbiting on the innermost stable circular orbit of the Galactic Centre black hole. *MNRAS*, **412**, pp. 2653–2664. doi:10.1111/j.1365-2966.2010.18084.x.
- Wahhaj, Z., M. C. Liu, B. A. Biller, F. Clarke, E. L. Nielsen, L. M. Close, T. L. Hayward, E. E. Mamajek, M. Cushing, T. Dupuy, M. Tecza, N. Thatte, M. Chun, C. Ftaclas, M. Hartung, I. N. Reid, E. L. Shkolnik, S. H. P. Alencar, P. Artymowicz, A. Boss, E. de Gouveia Dal Pino, J. Gregorio-Hetem, S. Ida, M. Kuchner, D. N. C. Lin, and D. W. Toomey (2011). The Gemini NICI Planet-finding Campaign: Discovery of a Substellar L Dwarf Companion to the Nearby Young M Dwarf CD-35 2722. *ApJ*, **729**, 139. doi:10.1088/0004-637X/729/2/139.
- Webb, R. A., B. Zuckerman, I. Platais, J. Patience, R. J. White, M. J. Schwartz, and C. McCarthy (1999). Discovery of Seven T Tauri Stars and a Brown Dwarf Candidate in the Nearby TW Hydrae Association. *ApJ*, **512**, pp. L63–L67. doi:10.1086/311856.
- Weidenschilling, S. J. (1977a). Aerodynamics of solid bodies in the solar nebula. *MNRAS*, **180**, pp. 57–70.
- Weidenschilling, S. J. (1977b). The distribution of mass in the planetary system and solar nebula. *Ap&SS*, **51**, pp. 153–158. doi:10.1007/BF00642464.
- Weinberg, N. N., M. Milosavljević, and A. M. Ghez (2005). Astrometric Monitoring of Stellar Orbits at the Galactic Center with a Next Generation Large Telescope. In P. K. Seidelmann & A. K. B. Monet (ed.) *Astrometry in the Age of the Next Generation of Large Telescopes*, volume 338 of *Astronomical Society of the Pacific Conference Series*, pp. 252–+.
- Weinberg, S. (1972). *Gravitation and Cosmology: Principles and Applications of the General Theory of Relativity*.
- Weinberger, A. J., G. Anglada-Escudé, and A. P. Boss (2013). Distance and Kinematics of the TW Hydrae Association from Parallaxes. *ApJ*, **762**, 118. doi:10.1088/0004-637X/762/2/118.
- Welch, P. D. (1967). The Use of Fast Fourier Transform for the Estimation of Power Spectra: A Method Based on Time Averaging Over Short, Modified Periodograms. *IEEE Trans. Audio & Electroacoust.*, Volume AU-15, p. 70-73, **15**, pp. 70–73.

- White, R. J. and A. M. Ghez (2001). Observational Constraints on the Formation and Evolution of Binary Stars. *ApJ*, **556**, pp. 265–295. doi:10.1086/321542.
- Wilson, J. C., P. M. Hinz, M. F. Skrutskie, T. Jones, E. Solheid, J. Leisenring, P. Garnavich, M. Kenworthy, M. J. Nelson, and C. E. Woodward (2008). LMIRcam: an L/M-band imager for the LBT combined focus. In *Society of Photo-Optical Instrumentation Engineers (SPIE) Conference Series*, volume 7013 of *Society of Photo-Optical Instrumentation Engineers (SPIE) Conference Series*, p. 3. doi:10.1117/12.789939.
- Willez, J., R. Akeson, M. Colavita, J. Eisner, A. Ghez, J. Graham, L. Hillenbrand, R. Millan-Gabet, J. Monnier, J.-U. Pott, S. Ragland, P. Wizinowich, E. Appleby, B. Berkey, A. Cooper, C. Felizardo, J. Herstein, M. Hrynevych, O. Martin, D. Medeiros, D. Morrison, T. Panteleeva, B. Smith, K. Summers, K. Tsubota, C. Tyau, and E. Wetherell (2010). ASTRA: astrometry and phase-referencing astronomy on the Keck interferometer. In *Society of Photo-Optical Instrumentation Engineers (SPIE) Conference Series*, volume 7734 of *Society of Photo-Optical Instrumentation Engineers (SPIE) Conference Series*. doi:10.1117/12.857740.
- Willez, J., R. Akeson, M. Colavita, J. Eisner, R. Millan-Gabet, J. Monnier, J.-U. Pott, S. Ragland, P. Wizinowich, M. Abajian, E. Appleby, B. Berkey, A. Cooper, C. Felizardo, J. Herstein, M. Hrynevych, D. Medeiros, D. Morrison, T. Panteleeva, B. Smith, K. Summers, K. Tsubota, C. Tyau, and E. Wetherell (2012). Self-Phase-Referenced Spectro-Interferometry on the Keck Interferometer. *PASP*, **124**, pp. 51–61. doi:10.1086/664075.
- Wollman, E. R., T. R. Geballe, J. H. Lacy, C. H. Townes, and D. M. Rank (1977). NE II 12.8 micron emission from the galactic center. II. *ApJ*, **218**, pp. L103–L107. doi:10.1086/182585.
- Wolniewicz, L., I. Simbotin, and A. Dalgarno (1998). Quadrupole Transition Probabilities for the Excited Rovibrational States of H₂. *ApJS*, **115**, p. 293. doi:10.1086/313091.
- Youdin, A. N. and J. Goodman (2005). Streaming Instabilities in Protoplanetary Disks. *ApJ*, **620**, pp. 459–469. doi:10.1086/426895.
- Yusef-Zadeh, F., H. Bushouse, C. D. Dowell, M. Wardle, D. Roberts, C. Heinke, G. C. Bower, B. Vila-Vilaró, S. Shapiro, A. Goldwurm, and G. Bélanger (2006). A Multiwavelength Study of Sgr A*: The Role of Near-IR Flares in Production of X-Ray, Soft γ -Ray, and Submillimeter Emission. *ApJ*, **644**, pp. 198–213. doi:10.1086/503287.
- Yusef-Zadeh, F., H. Bushouse, M. Wardle, C. Heinke, D. A. Roberts, C. D. Dowell, A. Brunthaler, M. J. Reid, C. L. Martin, D. P. Marrone, D. Porquet, N. Grosso,

- K. Dodds-Eden, G. C. Bower, H. Wiesenmeyer, A. Miyazaki, S. Pal, S. Gillessen, A. Goldwurm, G. Trap, and H. Maness (2009). Simultaneous Multi-Wavelength Observations of Sgr A* During 2007 April 1-11. *ApJ*, **706**, pp. 348–375. doi:10.1088/0004-637X/706/1/348.
- Yusef-Zadeh, F., M. Wardle, H. Bushouse, C. D. Dowell, and D. A. Roberts (2010). Occultation of the Quiescent Emission from Sgr A* by IR Flares. *ApJ*, **724**, pp. L9–L15. doi:10.1088/2041-8205/724/1/L9.
- Yusef-Zadeh, F., M. Wardle, C. Heinke, C. D. Dowell, D. Roberts, F. K. Baganoff, and W. Cotton (2008). Simultaneous Chandra, CSO, and VLA Observations of Sgr A*: The Nature of Flaring Activity. *ApJ*, **682**, pp. 361–372. doi:10.1086/588803.
- Zuckerman, B., I. Song, and M. S. Bessell (2004). The AB Doradus Moving Group. *ApJ*, **613**, pp. L65–L68. doi:10.1086/425036.
- Zuckerman, B., I. Song, M. S. Bessell, and R. A. Webb (2001). The β Pictoris Moving Group. *ApJ*, **562**, pp. L87–L90. doi:10.1086/337968.